



INSTITUTO SUPERIOR TÉCNICO  
Universidade Técnica de Lisboa

## **SYNCHRONOUS WOUND-ROTOR ELECTRICAL MACHINE CONTROL FOR ELECTRIC AIRPLANE TAXIING**

**Nuno Miguel Gomes da Silva**

Dissertação para obtenção do Grau de Mestre em  
**Engenharia Aeroespacial**

### **Júri**

Presidente: Prof. Doutor João Manuel Lage de Miranda Lemos

Orientador: Prof. Doutor Horácio João Matos Fernandes

Vogal: Prof. Doutor Joaquim António Fraga Gonçalves Dente

**Novembro de 2011**



To Avelino de Brito Pires,

*"Porque todos é que sabemos tudo"*



# RESUMO

---

O aumento do tráfego aéreo esperado para as próximas décadas, está a pressionar a indústria aeronáutica no sentido de reagir com uma melhoria na eficiência de operação do avião. Assim, surge a necessidade de melhorar o processo de parqueamento dos aviões, tanto ao nível da redução no consumo de combustível como nas emissões poluentes que têm lugar nesta fase do voo. Neste âmbito, o conceito de parqueamento eléctrico de aviões apresenta-se como uma solução muito interessante, na medida em que permite efectuar todo o parqueamento sem recorrer às turbinas principais do avião.

Nesta dissertação avalia-se a viabilidade da introdução de máquinas eléctricas síncronas de rotor bobinado no trem de aterragem principal de um avião. Esta solução irá permitir: (i) movimentar o avião durante o parqueamento, eliminando a necessidade de se utilizarem rebocadores ou as turbinas principais; (ii) regenerar energia eléctrica durante a marcha de inércia do avião. Por sua vez, esta energia eléctrica pode ser posteriormente introduzida na rede eléctrica do avião e, inclusivamente, utilizada para alimentar as máquinas eléctricas durante o próximo parqueamento, substituindo a energia outrora proveniente da APU do avião. Como resultado, a solução proposta irá aumentar a autonomia e eficiência do avião em todas as operações realizadas no solo.

Neste sentido, foi desenhada e construída uma plataforma de desenvolvimento da electrónica de potência necessária para controlar máquinas eléctricas trifásicas síncronas de rotor bobinado. Paralelamente, foi implementada uma nova técnica de controlo sem recurso a sensores, baseada na comparação da tensão BEMF média entre duas fases. Numa última fase, todo o sistema foi testado num protótipo para determinar a sua performance e aplicabilidade num avião. Os resultados obtidos, validam a nova técnica de controlo e demonstram o controlo da velocidade de rotação de uma máquina eléctrica síncrona de rotor bobinado.

**Palavras-chave:** Parqueamento eléctrico de aviões, Controlo de máquinas eléctricas, controlo sem sensores, detecção de BEMF, Máquina eléctrica síncrona de rotor bobinado

v

# ABSTRACT

---

The expected air traffic growth for the next decades, is pressuring the aeronautical industry to react with a correspondent improvement in the operating efficiency of the airplane. Hence, arises the necessity to ameliorate airplane taxiing, both in terms of reducing fuel consumption and pollutant emissions that take place in this phase of flight. In this scope, the concept of electric taxiing presents itself as a very interesting solution, as it allows performing all taxiing without recurring to the main engines of the airplane.

This paper assesses the feasibility of introducing a synchronous wound-rotor electrical machine (EM) in the main landing gear of an airplane. This solution will allow to: (i) power the airplane during taxiing, eliminating the necessity of using tug tractors or the main engines; (ii) regenerate electrical energy during the airplane roll. In turn, this electrical energy can be introduced in the power grid of the airplane and later used to power the EMs during taxiing, replacing the energy otherwise provided by the Auxiliary Power Unit (APU) of the airplane. As a result, the proposed solution will improve airplane autonomy and efficiency in ground operations.

In this context, was designed and built a development platform of the power electronics necessary for synchronous wound-rotor EM control. Alongside, a new sensorless Back Electromotive Force (BEMF) technique was implemented, employing average phase to phase voltage comparison. Ultimately, the proposed system was then tested on a prototype vehicle to determine its performance and applicability on an airplane. The results obtained validate the new control technique and show the rotational speed control of a synchronous wound-rotor EM.

**Keywords:** Electric airplane taxiing, Electrical machine control, Sensorless control, BEMF sensing, Synchronous wound-rotor electrical machine



# ACKNOWLEDGEMENTS

---

I would like to express a sincere gratitude to Prof. Horácio Fernandes, for all the guidance and scientific principles instilled, which greatly contributed to this work and to my formation as an engineer.

A genuine thanks to the IPFN and its personnel for their support, availability and practical advice, specially to Rui Dias, Eng. João Fortunato, Eng. Ivo Carvalho, Eng. Tiago Pereira, Eng. Rafael Henriques.

A heartfelt gratitude to my colleagues and friends Dário Silva, António Morgado, João Eloi, António Henriques, Guilherme Silva, João Teixeira, Edmundo Ferreira, Pedro Casau, Rui Santos, Tiago Fernandes, Anabela Reis and Pedro Fernandes for their unconditional support, availability and friendship.

A special word to Patrícia Segurado, for sharing this journey with me, and to my parents Paulo and Maria to whom I owe being here today.



# CONTENTS

---

<b>RESUMO .....</b>	<b>IV</b>
<b>ABSTRACT.....</b>	<b>VI</b>
<b>ACKNOWLEDGEMENTS .....</b>	<b>VIII</b>
<b>CONTENTS.....</b>	<b>X</b>
<b>LIST OF FIGURES.....</b>	<b>XIV</b>
<b>LIST OF TABLES .....</b>	<b>XVIII</b>
<b>LIST OF SYMBOLS.....</b>	<b>XX</b>
<b>LIST OF ACRONYMS .....</b>	<b>XXII</b>
<b>CHAPTER 1      Introduction .....</b>	<b>1</b>
1.1      Problem Statement.....	2
1.2      Dissertation Outline.....	2
<b>CHAPTER 2      Airplane Taxi Stage.....</b>	<b>5</b>
2.1      Overview.....	5
2.2      Issues and room for improvement.....	6
2.2.1      Operational issues .....	6
2.2.2      Safety issues .....	7
2.2.3      Environmental issues.....	7
2.2.4      Cost .....	7
2.3      New Approaches to Airplane Taxiing.....	8
2.3.1      Dispatch Towing.....	8
2.3.2      Autonomous Ground Propulsion System (AGPS).....	9
2.3.3      Comparison .....	11
2.4      Proposed Concept of Electric Taxiing.....	11
2.4.1      Concept summary .....	11

2.4.2	Synchronous Wound-rotor Electrical Machine .....	12
2.4.3	Power Source specifics .....	14
2.4.4	Airplane Integration .....	15
2.4.5	System Savings.....	15
2.5	Prototype approach.....	16
2.5.1	Power Electronics .....	16
2.5.2	Electrical Machine.....	17
2.5.3	Testing structure .....	17
2.6	Summary.....	18
<b>CHAPTER 3</b>	<b>Electrical Machine Control.....</b>	<b>19</b>
3.1	Control principle.....	19
3.2	Sensored Control .....	20
3.3	Sensorless Control.....	22
3.3.1	Field-Oriented Control (FOC).....	22
3.3.2	BEMF Sensing and zero crossing point (ZCP) .....	23
3.4	Voltage application techniques.....	25
3.4.1	Pulse-Width Modulation .....	25
3.4.2	Sinusoidal Pulse-width modulation (SPWM) .....	26
3.4.3	Space vector modulation (SVM).....	27
3.4.4	Six-step commutation .....	28
3.5	Chosen control method .....	30
3.5.1	New voltage sensing method .....	30
3.5.2	Method description for six-step commutation .....	31
3.5.3	Method description for sinusoidal PWM.....	33
3.5.4	Commutation errors compensation .....	34
3.5.5	Robustness.....	35
3.6	Summary.....	36
<b>CHAPTER 4</b>	<b>Control method implementation .....</b>	<b>37</b>
4.1	Control structure .....	37

4.1.1	Alignment.....	37
4.1.2	Open loop start.....	38
4.1.3	Sensorless run.....	39
4.2	Firmware.....	39
4.2.1	Features overview .....	39
4.2.2	Hardcode Configuration.....	40
4.2.3	Commutation vector .....	40
4.2.4	Major functions Flow charts.....	41
4.2.5	Real-Time Updates .....	46
4.3	Microcontroller Implementation .....	47
4.3.1	ADC configuration.....	47
4.3.2	UART configuration.....	48
4.3.3	TIMERS configuration .....	49
4.3.4	MCPWM configuration.....	50
4.3.5	OUTPUT COMPARE configuration .....	50
4.3.6	INPUT CAPTURE configuration.....	51
4.3.7	CHANGE NOTIFICATION CONFIGURATION .....	51
4.3.8	INTERRUPTS configuration.....	52
4.4	Summary .....	52
<b>CHAPTER 5</b>	<b>Hardware Description .....</b>	<b>53</b>
5.1	Purpose and overview.....	53
5.1.1	Purpose .....	53
5.1.2	Overview.....	54
5.2	Control Module .....	56
5.2.1	dsPIC® Control Board.....	57
5.2.2	EM Control Board.....	58
5.3	Power Module .....	69
5.3.1	Power Switches.....	70
5.3.2	Solder-Free Construction.....	70

5.3.3	Power dissipation .....	71
5.3.4	Transients and noise suppression features .....	72
5.4	Summary .....	73
<b>CHAPTER 6</b>	<b>Tests and Results.....</b>	<b>75</b>
6.1	Testing Structure assembly.....	75
6.2	Control method validation.....	76
6.3	Prototype Performance.....	77
6.3.1	Open Loop start .....	77
6.3.2	Speed Control .....	78
6.3.3	Field Weakening.....	81
6.3.4	Power and Torque .....	82
6.4	Summary .....	84
<b>CHAPTER 7</b>	<b>Conclusions.....</b>	<b>85</b>
7.1	Future Work.....	87
<b>Appendix A</b>	<b>MAIN CODE PARAMETERS.....</b>	<b>88</b>
A.1	Files listing.....	88
A.2	Parameters listing .....	89
A.3	Flags listing.....	91
<b>Appendix B</b>	<b>FIRMWARE FLOW CHARTS .....</b>	<b>92</b>
<b>Appendix C</b>	<b>SCHEMATICS.....</b>	<b>97</b>
<b>Appendix D</b>	<b>Hardware Validation Results.....</b>	<b>103</b>
<b>BIBLIOGRAPHY .....</b>		<b>105</b>

# LIST OF FIGURES

---

Figure 2.1 - CAD model of the TaxiBot system, showing airplane nose wheel and landing gear fully engaged (6).....	9
Figure 2.2 - Main landing gear with electrical machines for autonomous taxiing.....	10
Figure 2.3 - Block diagram representation of the proposed concept of electric taxiing .....	12
Figure 2.4 - Block diagram representation of the power network for the proposed Concept of taxiing .....	15
Figure 2.5 - Cutaway of a claw-pole alternator.....	17
Figure 2.6 - CAD model of the testing structure.....	17
Figure 3.1 - Graphical representation of a machine control method .....	20
Figure 3.2 – Hall sensor signal, BEMF, output torque and phase current waveforms of an EM with trapezoidal BEMF.....	21
Figure 3.3 – Vector control transformations .....	23
Figure 3.4 – BEMF voltages, phase currents, phases zero crossing points and Hall sensor waveforms comparison .....	25
Figure 3.5 - PWM signal and corresponding average voltage for different duty cycles .....	26
Figure 3.6 - Sinusoidal pulse-width modulation schematic implementation .....	26
Figure 3.7 - Space vector modulation representations: A) hexagon; B) reference vector addition .....	28
Figure 3.8 - Six-step commutation stator field in relation to the rotor .....	29
Figure 3.9 – Six-step commutation method: phase waveforms representation on the left and inverter schematic perspective on the right.....	30
Figure 3.10 - Inverter topology and electrical machine equivalent circuit, where R, L and e represent the winding resistance, inductance and BEMF, respectively (37).....	31
Figure 3.11 - Phase relationship between BEMF ( $e_a$ ), average terminal voltage of phases a ( $V_a$ ) and c ( $V_c$ ) and average phase to phase voltage ( $V_{ac}$ ) (37) .....	33
Figure 3.12 - New terminal voltage sensing method circuit representation (37) .....	34
Figure 3.13 - Voltage spikes in zero crossing detection for phase voltages a and c, and spikes absence in phase to phase voltage ac (37) .....	36
Figure 4.1 – Sensorless control algorithm stages for a BEMF sensing method.....	38
Figure 5.1 - Developed controller block diagram .....	55

Figure 5.2 - Developed controller overview .....	56
Figure 5.3 - Control module developed for this thesis (dsPIC® and EM control boards) .....	57
Figure 5.4 - dsPIC30F4011 board developed by IPFN .....	58
Figure 5.5 - Bootstrap method schematic representation.....	59
Figure 5.6 - Schematic of the MOSFET gate driver circuit for pair PWM1 .....	61
Figure 5.7 - Parasitic inductances in half-bridge and the consequent VS pin undershoot.....	61
Figure 5.8 - Schematic of the asymmetric gate resistor network circuit for pair PWM1.....	62
Figure 5.9 - Schematic of the DC bus voltage feedback circuit.....	63
Figure 5.10 - Schematic of the low-side DC bus current measurement circuit.....	64
Figure 5.11 - Bode plot of spice simulation pertaining to the low-side DC bus current measurement circuit (signal I_BUS), where it can be verified that $f - 3dB = 16.6\text{Hz}$ and 60dB/decade attenuation.....	65
Figure 5.12 - Schematic of the overcurrent detection circuit.....	66
Figure 5.13 - Schematic of the BEMF sensing circuit for phase U.....	66
Figure 5.14 - Bode plot of the spice simulation pertaining to the low-side phase current measurement circuit (signal I_Phase_U), where it can be verified that $f - 3dB = 2.87\text{kHz}$ and 60dB/decade attenuation.....	68
Figure 5.15 - Schematic of the Hall effect sensor interface circuit .....	69
Figure 5.16 - Schematic of the gear-tooth sensor interface circuit .....	69
Figure 5.17 - Developed solder-free three-phase power module with extra rotor terminal .....	70
Figure 5.18 - Schematic representation of the developed solder-free three-phase bridge .....	71
Figure 5.19 - Developed solder-free half-bridge.....	72
Figure 6.1 - Testing structure built for this dissertation .....	75
Figure 6.2 - Comparison between the pseudo-Hall signal <i>U_VOLT_COMP</i> (CH1) and the correspondent Hall sensor Signal (CH3); CH2 and CH4 are BEMF voltages of phases U and W respectively (Appendix C) .....	76
Figure 6.3 - Power consumption profile during start from standstill (no load), showing the three stages of the control software: alignment, open loop start and sensorless run .....	78
Figure 6.4 - Rotor rotational speed response to a step in the reference (potentiometer), for 12V operation and no load .....	79
Figure 6.5 - Rotor rotational speed response to a step in the reference (potentiometer), for 24V operation and no load .....	79
Figure 6.6 - Rotor rotational speed response to a sequence of variations in the reference (potentiometer) under constant load, for 12v operation.....	80
Figure 6.7 - Rotor rotational speed variation for different rotor magnetic field intensities (field weakening), for 12V operation and no load .....	81

Figure 6.8 - Power and torque measurements for 12V operation with load .....	83
Figure 6.9 - Power and torque measurements for 24V operation with load .....	83
Figure B.1 - STOP_Motor function flow chart.....	92
Figure B.2 - START_Motor function flow chart.....	93
Figure B.3 - CNInterrupt function flow chart .....	93
Figure B.4 - Main function flow chart.....	94
Figure B.5 - T1Interrupt function flow chart.....	95
Figure B.6 - Open2lock_transition function flow chart .....	96
Figure C.1 - MOSFET gate drivers circuitry schematics .....	98
Figure C.2 - Phase and bus currents feedback circuitry schematics.....	99
Figure C.3 -Schematics of DIN 96, DIL 10 and DB 25 connectors, buttons and geartooth .....	100
Figure C.4 -Voltage Feedback circuitry and Hall sensors interface schematics.....	101
Figure C.5 - Power module schematics .....	102
Figure D.1 - BEMF of phase U (CH3) and BEMF filtering of phases U (Ch1) and W (CH2) during sensorless run mode; correspondent pseudo-Hall signal <i>U_VOLT_COMP</i> (CH4).....	103
Figure D.2 - BEMF of phase U (CH3) and BEMF filtering of phases U (Ch1) and W (CH2) during open loop start; correspondent pseudo-Hall signal <i>U_VOLT_COMP</i> (CH4).....	103
Figure D.3 - BEMF of phase U (CH1), half-bridge current of phase U (CH3), BEMF of phase W (CH4) and half-bridge current of phase W (Ch2) during sensorless run mode.....	104
Figure D.4 - Half-bridge current of phase W (CH2), half-bridge current of phase U (CH3) and half-bridge current of phase V (Ch4) during sensorless run mode .....	104



# LIST OF TABLES

---

Table 2.1 - Major advantages of the TaxiBot over a traditional taxiing system (6) .....	9
Table 2.2 - Major advantages of an electrical autonomous ground propulsion system over the traditional taxiing system (7), (9) and (10) .....	10
Table 2.3 - Acceleration and speed requirements of typical taxiing.....	13
Table 2.4 - Weights of the electric taxiing system, fuel savings and overall net weight.....	14
Table 2.5 - Major savings of the proposed concept of electric taxiing with electrical energy recovery over a traditional taxiing system.....	16
Table 2.6 - Scaling between the real size power electronics of the airplane and the power electronics of the prototype .....	16
Table 4.1 - Hall Sensor readings and phase energize sequence for six-step commutation .....	41
Table 4.2 - dsPIC30F4011 major configuration bits settings .....	47
Table 4.3 - dsPIC30F4011 ADC module configuration.....	48
Table 4.4 - dsPIC30F4011 UART module configuration.....	49
Table 4.5 - dsPIC30F4011 TIMER module configuration.....	49
Table 4.6 - dsPIC30F4011 MCPWM module configuration.....	50
Table 4.7 - dsPIC30F4011 OUTPUT COMPARE module configuration.....	51
Table 4.8 - dsPIC30F4011 INPUT CAPTURE module configuration.....	51
Table 4.9 - Software interrupt functions priorities.....	52
Table 5.1 - Developed controller major requirements.....	54
Table A.1 - Source code files, purpose and specific functions contained.....	89
Table A.2 - Major Parameters listing and respective software Implications .....	90
Table A.3 - Flags listing and respective software implications .....	91



# LIST OF SYMBOLS

---

<b>General Use</b>		
$f_{-3dB}$	Cutoff frequency, Hz	$\omega_r$ Average angular speed of the rotor, rad/s
B	Magnetic field, T	$\phi_1$ Phase delay angle induced by the RC filter, radians
C	Capacitance, F	$\phi_2$ Current lagging angle caused by the armature inductance, radians
d	Duty-Cycle	$\Delta t_s$ Interpolation time period, s
E	Electric field, V/m	
F	Force, N	
I	Current, A	<b>Bootstrap</b>
m	Mass, kg	$I_{DS-}$ Desat diode bias when on
P	Power, W	$I_{LK}$ Floating section leakage current, A
p	Number of rotor pole pairs	$I_{LK\_CAP}$ Bootstrap capacitor leakage current, A
$P_{avg}$	Average Power, W	$I_{LK\_DIODE}$ Bootstrap diode leakage current, A
q	Electric charge of particle, C	$I_{LK\_GE}$ MOSFET gate-source leakage current, A
R	Resistance, $\Omega$	$I_{QBS}$ Floating section quiescent current, A
t	Time, s	$C_{BOOTmin}$ Minimum capacitance of the bootstrap capacitor, C
v	Velocity, m/s	$Q_G$ MOSFET turn-on required gate charge, C
V	Voltage, V	$Q_{LS}$ Charge required by internal level shifters, C
W	Work, J	$Q_{TOT}$ Total charge, C
<b>Control Method</b>		$Q_{gd}$ MOSFET gate-to-drain charge, C
$L_a$	Inductance of phase a, H	$Q_{gs}$ MOSFET gate-to-source charge, C
$R_a$	Resistance of phase a, $\Omega$	$R_{DRp}$ Equivalent on-resistance of the driver, $\Omega$
$V_a$	Average terminal voltage of phase a, V	$R_{Gon}$ MOSFET turn-on resistor, $\Omega$
$V_{pnn}$	Switching State Vector pnn, V	$V_{CC}$ Integrated circuit supply voltage, V
$\theta_e$	Angle of electrical cycle, degrees	
$\theta_r$	Angle of rotor position, degrees	
$\omega_e$	Fundamental frequency of terminal voltage, rad/s	

$V_F$	Bootstrap diode forward voltage, V
$V_{LS}$	Voltage drop across the low-side MOSFET or load, V
$V_{Min}$	Minimum voltage between $V_B$ and $V_S$ , V
$V_{gs}^*$	MOSFET gate-to-source plateau (Miller) voltage
$t_{on}$	MOSFET turn-on time, s
$\Delta V_{BS}$	Voltage drop across the bootstrap capacitor, V

# LIST OF ACRONYMS

---

A/D	Analog-to-Digital	MCU	Microcontroller
AC	Alternate Current	MEA	More Electric Aircraft
ACIM	AC Induction Machine	MLG	Main Landing gear
ADC	Analog-to-Digital Converter	MOSFET	Metal-Oxide-Semiconductor Field-Effect Transistor
AGPS	Autonomous Ground Propulsion System	MTOW	Maximum Take Off Weight
APU	Auxiliary Power Unit	NLG	Nose Landing Gear
BEMF	Back Electromotive Force	OET	Optimized Electric Taxiing
BLDC	Brushless DC	OL	Open Loop
CMRR	Common Mode Rejection Ratio	PCB	Printed Circuit Board
CPU	Central Processing Unit	PM	Permanent Magnets
DC	Direct Current	PMSM	Permanent Magnet Synchronous Machine
DSC	Digital Signal Controller	PPVS	Phase to Phase Voltage Sensing
DSP	Digital Signal Processor	PWM	Pulse Width Modulation
EM	Electrical Machine	RC	Resistor-Capacitor
EMF	Electromotive Force	RPM	Revolutions per Minute
EMI	Electromagnetic Interference	SPICE	Simulation Program with Integrated Circuit Emphasis
ESC	Electronic Speed Controller	SPWM	Sinusoidal Pulse Width Modulation
FOC	Filed Oriented Control	SSV	Switching state vectors
FOD	Foreign Object Damage	SVM	Space Vector Modulation
IAI	Israel Aerospace Industries	ZCP	Zero Crossing Point
IGBT	Insulated Gate Bipolar Transistor		
MCPWM	Motor Control PWM		

ESR      Equivalent Series Resistance

LSB      Least Significant Bit

# CHAPTER 1

## INTRODUCTION

---

When considering airplane operation, specially a typical flight profile, the taxi stage, hereafter referred to as taxiing, is most commonly regarded as having little impact on overall performance, mainly due to its short duration. Although, the aeronautical industry faces a steep air traffic growth [1], with evident consequences on the surface-traffic of the airports and taxiways length. Alongside, a new approach on airplane design, manufacturing and operation is underway, with emphasis on the use of technology which can influence maintenance costs and fuel usage. The More Electric Aircraft (MEA) and Power Optimized Aircraft (POA) initiatives [2], [3], followed by research projects such as CleanSky [4], establish guidelines for an increased efficiency of overall airplane operation and energy use. Essentially the traditional engine, which produces thrust, pneumatic, hydraulic, and electric power, is redesigned and optimized to solely produce thrust and electric power. Smaller electric machines are responsible to locally generate the power needed for the pneumatic, hydraulic and other mechanical systems. Therefore, operating and maintenance costs are reduced, together with an improved reliability.

In this context, the aeronautical industry is mobilizing to provide new taxiing alternatives, with special focus on eliminating the use of main engines of the airplane during this stage. Therefore, two new approaches to current airplane taxiing arise, these being (i) dispatch towing [5], [6], and (ii) autonomous ground propulsion systems (AGPS) [7], [8] and [9]. They both allow considerable fuel and environmental savings, since the taxiing is performed without recurring to the main engines. Though, only AGPS further improves autonomy of the airplane in ground operations, discarding the utilization of tug tractors.

The alternative proposed in this dissertation employs a synchronous wound-rotor electrical machine (EM) placed in the landing gear. This EM will be responsible for (i) moving the airplane

during taxiing and (ii) regenerate electrical energy during the airplane roll. This electrical energy can later be used to power the EMs in the landing gear or other airplane systems. Accordingly, the fuel and environmental savings achieved will be higher than in the two existing alternatives.

To assess the performance of the proposed system, and applicability on an airplane, was designed, constructed and validated a controller for three phase synchronous wound-rotor EMs, where was implemented a new sensorless control technique.

## 1.1 PROBLEM STATEMENT

The development of an airplane taxiing electrical system involves a thorough study of the electric and mechanical characteristics of the system to enable applicability on an airplane. From the electric point of view, specifically in regard to the EM and respective power electronics, it is important to ensure that the system is able to move the airplane during taxiing, reaching the requisites of acceleration and speed for the aviation industry. Therefore, the problem can be divided in:

- determine the airplane taxiing requirements and system dimensioning;
- study of a control methodology for proper EM operation;
- design and construction of a scale prototype of the EM controller;
- practical testing of the prototype to assess applicability on an airplane.

This problem folding was decided taking into consideration the impossibility of building an EM controller that could be implemented and tested on an airplane, due to budgetary and time constraints of the dissertation.

## 1.2 DISSERTATION OUTLINE

This dissertation can be outlined as follows:

- Chapter 2 which describes airplane taxiing in general and develops the followed approach;
- Chapter 3 which introduces electrical machine control fundamentals and describes the chosen control technique;
- Chapter 4 which describes in detail the software implementation of the chosen control method and microcontroller (MCU) configuration;
- Chapter 5 which thoroughly describes the hardware implementation of the power electronics of the EM controller;
- Chapter 6 which shows the practical results obtained with the prototype;

- Chapter 7 which concludes the dissertation and presents future works.

Each chapter begins with a brief introduction containing relevant concepts and a general framework of the main topic of the chapter, followed by a detailed description of the work undertaken. At the end, a brief summary itemizes the key points of the chapter.

The appendixes provide complementary information to the subjects discussed throughout the dissertation.



# CHAPTER 2

## AIRPLANE TAXI STAGE

---

The following chapter focuses on the airplane taxi stage, where the major motivation behind this thesis lies. In detail, the current taxiing process of an airplane is explained, itemizing the key drawbacks that open room for improvement. Two improved concepts are stated: airplane full towing from gate to holding area [5], [6]; and an electric ground propulsion system fully integrated on the airplane [7], [8], [10], [11] and [12]. The last, for its unique features and progress, was chosen as the basis for this dissertation. Moreover, a new technological approach to an integrated ground propulsion system for airplanes is proposed, together with a prototype construction for practical assessment of the technologies involved.

### 2.1 OVERVIEW

Throughout the aviation history there is a process where little intervention has been made, this being airplane taxiing. This stage encompasses all the movements of an airplane on the ground, only excluding the accelerating run along a runway prior to take-off, or the decelerating run after landing. The airplane can move on its own power or be towed by a special tractor, also called tug.

To cope with the efficiency quest taken by the aeronautical industry, stated in the MEA directives, airplane taxiing has to address decade pending issues (see section 2.2). Above all, it has to face the ever-increasing air traffic, which causes a surface-traffic problem at major airports. The length and complexity of runways, taxiways and terminal ramp areas are increasing. This has direct consequences, such as a superior taxi time and increased local emissions from the airport.

Furthermore, there is a process that requires special attention, which is the backward motion of an airplane required to exit the airport gate, or in other ground operations. Despite that many airplanes can also move backwards on the ground using reverse thrust, the resulting jet blast can cause damage to surrounding infrastructures. Therefore, ground movements close to the airport terminal require the use of a tug, and the remaining motions have to be surrounded by safety measures, which take into consideration the jet blast effect.

## 2.2 ISSUES AND ROOM FOR IMPROVEMENT

To further understand the taxiing process and how it must be improved, to cope with the most recent requirements for a more efficient airplane, the following sections itemize the main drawbacks involved in current taxiing operations.

### 2.2.1 OPERATIONAL ISSUES

Regardless of an airplane being parked at an airport gate or ramp, in order to take-off it has to taxi from its current position until the beginning of the runway. Usually the processes involved encompass positioning and connecting the tug; pushback/towing of the airplane; disconnecting the tug; and moving from the gate or ramp until the runway. All these processes take, on average, twenty five minutes [5], [11] and [12]. Concerning the time period during which the airplane moves from the gate until the runway, it only depends on the surface-traffic of the airport and taxiway length. In regard to all the processes prior to this taxiing stage, they are related to the airplane itself (time for APU start and system check) and ground operations (luggage loading, airplane refuel and passengers boarding). Hence, to improve taxiing efficiency it is necessary to separately address these two time slots.

The ever-increasing surface-traffic at the major airports, together with a growing complexity and length of current taxiways, makes the task of reducing the time span between gate exit and runway arrival a very demanding one. One possible solution is to implement control algorithms to enhance traffic flows [13]. Other is to decrease airplane separation to achieve a higher surface density, which raises the quest for new taxiing methods, preferably with main engines off, dispensing jet blast separation [9], [14].

In regard to all the processes prior to an airplane leaving the gate, mainly the pushback procedure, there is also a need for improvement. The pushback itself takes only one minute and a half on average [11]. Though, between the connection of the tug to the airplane and the beginning of actual forward displacement towards the runway, there is a five minutes period [11]. This time lapse is mainly due to all the procedures that have to be met between the pilots

and tug operators, to guarantee a safe maneuver. Moreover, there is the risk of the tug to damage the nose landing gear (NLG).

It is also relevant mentioning that taxiing is responsible for fifty to seventy percent of carbon brake wear, due to engines over thrust while at idle.

### **2.2.2 SAFETY ISSUES**

There are also some risks involving taxiing procedures that need to be taken into consideration. The main engines create a powerful jet blast, which in the gate/ramp area can injure ground personnel or damage equipment. In addition, the engines continuously suck in sand and other debris that might inflict damage to the engine, which is commonly referred to as foreign object damage (FOD). This is even more important when taken into account that fifty percent of all FOD incidents occur during taxiing [5]. Also, these objects can also be shredded and propelled out, becoming dangerous projectiles.

It is also important to consider the tug-airplane interaction, where communication errors between the pilot and the tug operator can occur, leading to harmful situations to both the airplane and ground equipment.

### **2.2.3 ENVIRONMENTAL ISSUES**

Considering that throughout the majority of the taxiing at least one main engine is on, there are considerable noise and pollutant emissions, with a significant impact on operational costs and airport fees. Moreover, from all airplane operating phases, taxiing is the major contributor in relation to carbon monoxide and unburned hydrocarbons emissions [5], [12]. The reason behind this is the very inefficient operation of the jet engines during taxiing, since they operate at very low power and, consequently, far from the designed operating power range. As a reference, the long-haul Airbus A380 uses up to 500 tons/year [5] of jet fuel exclusively on taxiing, this represents 1580 tons/year in CO<sub>2</sub> emissions [15]. This is even more evident when considering the world short-haul airplane fleet, where taxiing is a greater percentage of total airplane use, and a total of 5 million tons/year of fuel (15.8 million tons/year of CO<sub>2</sub>) [10] are used.

### **2.2.4 COST**

In a traditional taxiing there are two main costs to be considered, these being the costs associated with ground handling and the ones related to fuel consumption. Regarding the A380 case abovementioned, with the current fuel prices [16], taxiing represents a cost of 361k€/year solely on fuel. Furthermore, considering on average a cost of 120 €/flight on ground handling [11] and 3.75 flights/day [9], this represents a total of 164k€/year. The sum of the two establishes the taxiing cost of an A380 in 525k€/year, without considering noise and emissions

fees applied locally by the airports. In relation to the world short-haul airplane fleet, the fuel expenditure during taxiing, without additional airport fees, represents an amazing 3,614 M€/year.

## 2.3 NEW APPROACHES TO AIRPLANE TAXIING

In the following sections are described two new approaches to airplane taxiing that intend to address the aforementioned problems and bring taxiing efficiency to new reference levels.

### 2.3.1 DISPATCH TOWING

The dispatch towing concept is based on a tug responsible for towing the airplane from the airport gate until the beginning of the runway (taxi-out), and to return it to the gate after landing (taxi-in). This eliminates the use of airplane engines during taxiing, which has a considerable impact on pollutant and noise emissions. Despite not being a totally new idea, its implementation has been somewhat difficult, mainly due to the pending communication issue between the pilot and tug operator. During the pushback operation, since the pilot cannot see what is behind the airplane, the procedure is controlled by the tug operator. On the other hand, during forward motion of the airplane the control has to be done by the pilot; however, the tug can only be controlled by the tug operator, and for this reason all the pilot commands have to be communicated to the tug. Hence, dispatch towing as been regarded has unsafe due to the impossibility of the pilot to take control of the airplane during taxiing. Moreover, it produces too much wear and tear on the nose landing gear.

Though, a joint initiative between Israel aerospace industries (IAI) and Airbus brought the dispatch towing concept to a completely new era. As a result, it was created the TaxiBot system [6], [5], which is a semi-robotic towbarless tug with a unique mechanical interface to the NLG (Figure 2.1). The pilot uses existing airplane controls in the same way it is accustomed to when taxiing using the airplane engines. It is then the task of the mechanical interface to interpret the pilot solicitations reflected in the NLG and to drive the tug accordingly. Early testing indicates an improved airplane safety on icy or slippery surfaces, due to a larger contact surface which improves traction.

The TaxiBot is currently powered by two five hundred horse power V8s engines, powering six hydraulic machines, one in each wheel. However, it is also under study the concept of an electric powered system, which can further decrease pollutant emissions. Furthermore, the system can be used with any type of airplane, not requiring any modification to be done on it.

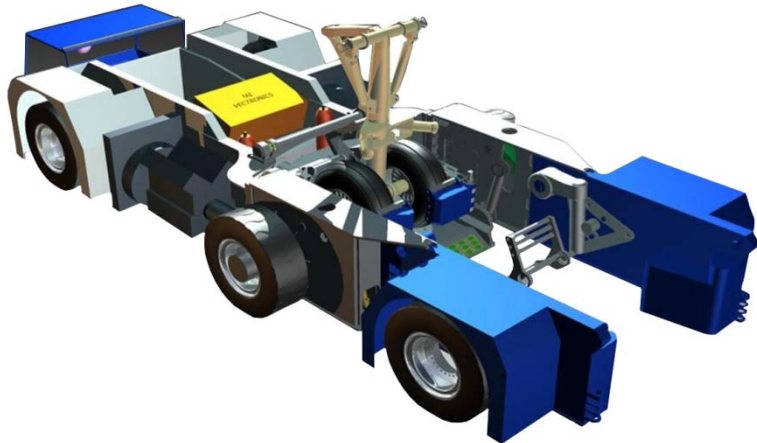


**Figure 2.1 - CAD model of the TaxiBot system, showing airplane nose wheel and landing gear fully engaged [6]**

In Table 2.1 are summarized the major advantages of the TaxiBot system over traditional taxiing [6].

Category	Advantages over traditional taxiing
Fuel cost of taxiing (global)	Reduction from 4,870 million €/year to 521.6 million €/year
Emissions of taxiing (global)	Reduction from 18 million tons/year to 2 million tons/year
Noise	Reduction due to non utilization of main engines
FOD avoidance while taxiing	Savings of 243.4 million €/year
Brakes	Less carbon brake wear, no need to counter residual thrust from main engines

**Table 2.1 - Major advantages of the TaxiBot over a traditional taxiing system [6]**

To mention the current interest of the aeronautic community on this topic, visible in recent CleanSky calls for proposal, which comprehend the design and manufacture of systems similar to the TaxiBot [17].

### 2.3.2 AUTONOMOUS GROUND PROPULSION SYSTEM (AGPS)

An autonomous ground propulsion system allows an airplane to perform all the taxiing maneuvers, without the use of tugs or the airplane engines. In detail, it consists on placing an electrical, or hydraulic, machine in the nose/main landing gear, capable of moving the airplane both backwards and forward (Figure 2.2). The system is powered by the Auxiliary Power Unit (APU) of the airplane and fully controlled by the pilot.

Initial system concepts employed a hydraulic machine within the wheel of the NLG of an airplane. However, this concept was not integrated on existing airplane due to system weight.

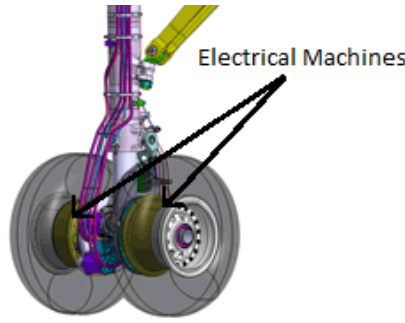


**Figure 2.2 - Main landing gear with electrical machines for autonomous taxiing**

Nowadays, the increasing development in power electronics, allows the recent electrical concepts to weigh less than the fuel weight they save per flight [9]. Hence, electric AGPS represents an incredible alternative to any existing taxiing method, for the autonomy in ground operations it grants to an airplane, and also for the fuel savings it allows, up to four percent [7], [8] and [10] regardless of the introduced extra weight. A proof of this attractiveness is the involvement of companies such as Honeywell, Safran, Messier-Bugatti, Boeing and Airbus in electrical APGS systems.

Concerning the system itself, an electrical machine of 50kW and with a torque of 11kN·m [11], placed in the landing gear (nose or main), is sufficient to move the airplane. Since it requires some modifications to be made on the airplane, it is expected for the system to be part of the design process of new airplanes and to be retrofitted onto existing ones.

The major advantages of electric AGPS over traditional taxiing are summarized in Table 2.2.

Category	Advantages over traditional taxiing
Fuel consumption	Reduction in 4-5% of total fuel consumption
Emissions	Reduction in 4-5% of total emissions and up to 90% during taxiing
Noise	Reduction due to non utilization of main engines
FOD avoidance while taxiing	Savings of 243.4 million €/year
Brakes	Less carbon brake wear, no need to counter residual thrust from main engines
Safety	Improved for airplane and ground personnel/equipment
Autonomy	Complete autonomy in ground maneuvers, no need for tugs

**Table 2.2 - Major advantages of an electrical autonomous ground propulsion system over the traditional taxiing system [7], [9] and [10]**

Also, the interest of this topic inside the aeronautic community is well stated in two very recent CleanSky call for proposals, that requested the development of electromechanical wheel actuators for taxiing, both for airplanes and rotorcrafts [17], [18].

### **2.3.3 COMPARISON**

The aforementioned systems provide a reliable and much improved alternative to the current state of airplane taxiing. They both achieve similar, and admirable, reductions in fuel consumption, noise and pollutant emissions, together with a respectable FOD avoidance rate.

Overall the TaxiBot tug system allows slightly higher fuel and emission savings, since the taxiing is performed without the main engines utilization while not introducing extra weight on the airplane. However, it introduces new ground traffic hurdles, as the TaxiBot fleet has to be controlled, and does not completely solves the availability issue, since the airplane is still dependent on the fleet of tugs.

The electrical AGPS system requires some airplane modifications and introduces permanent weight to it. Though, this is compensated by the weight of the fuel reduction it allows. Moreover, the fuel reductions still represent savings in the order of millions of euros per airplane. Also, it is the only solution available that allows for a totally independent taxiing, without the use of either the main engines or tugs, which drastically improves ground traffic and safety.

## **2.4 PROPOSED CONCEPT OF ELECTRIC TAXIING**

From the two new approaches to airplane taxiing, the electrical AGPS system was chosen has the basis for the concept of electric taxiing proposed on this dissertation. This taxiing solution proves to be reliable, with major environmental and financial savings, and a considerable impact on ground traffic. The necessity to optimize airplane performance in all flight phases requires a long-lasting taxiing solution that can bring airport management and airplane movements on the ground for completely new standards. Therefore, the electric ground propulsion system arises as the path towards taxiing future.

### **2.4.1 CONCEPT SUMMARY**

This dissertation proposes an optimized electric taxiing (OET) concept, where electrical energy is recovered during the airplane roll<sup>1</sup>. The recovered electrical energy can later be used to power electric taxiing, ultimately eliminating the necessity of the power to be delivered by the APU. Thus, the proposed electric taxiing system will allow fuel savings above all the existing concepts, including electric TaxiBot concepts.

To accomplish this, EMs were placed in the main landing gear (MLG), being these responsible for (i) powering the airplane on ground movements, and (ii) recover electrical energy during the

---

<sup>1</sup> The main focus of this dissertation is electric taxiing, in particular how to enable ground movements of the airplane solely recurring to EMs placed in the MLG. Referring to energy recovery using these EMs, all data can be found in [19].

airplane roll (Figure 2.3). Moreover, the EM placement in the MLG, in opposition to existing concepts that use the NLG, is due to approximately 90% of the airplane's weight to be on the MLG. This improves operation under adverse weather conditions, where traction is an issue.

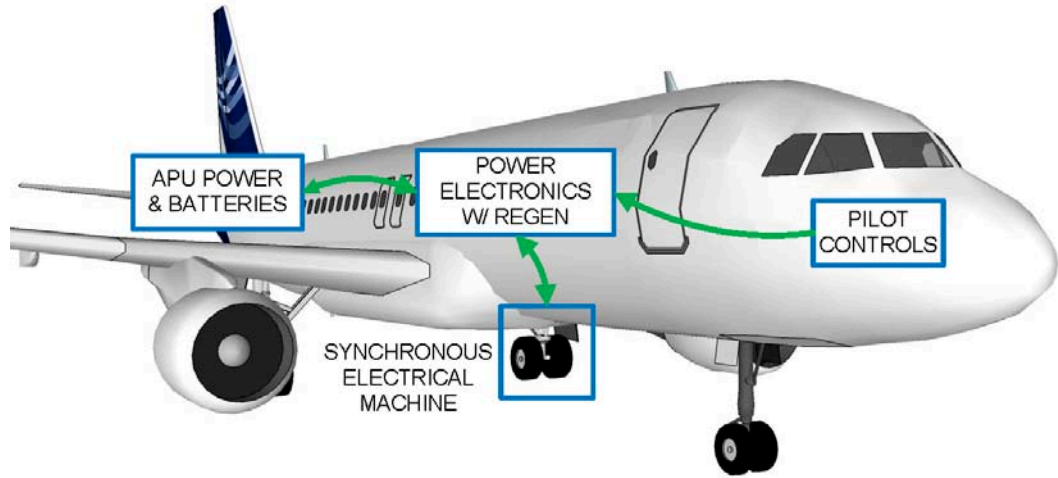


**Figure 2.3 - Block diagram representation of the proposed concept of electric taxiing**

#### 2.4.2 SYNCHRONOUS WOUND-ROTOR ELECTRICAL MACHINE

In order to select the type of EM to be employed in the OET concept, it was important to take into consideration the generator capabilities of the EM, since electrical energy recovery during airplane roll is a primary concern.

As stated in [19], a synchronous wound-rotor EM placed in the landing gear of the airplane enables energy regeneration during the airplane roll, further providing some electromagnetic braking capability. This type of EM attains a good performance as an electric generator [20], [21], mainly due to the capability of controlling rotor magnetic field intensity, which determines the induced BEMF and, ultimately, the amount of electrical energy recovered. Alongside, it also achieves a good performance as an electric motor. All things considered, a synchronous wound-rotor EM totally fulfills the requirements inherent to the OET concept. Therefore, it was selected as the EM to be employed in the MLG.

Concerning the wound-rotor choice in specific, there are also synchronous machines that employ permanent magnets (PM) in the rotor, enabling a higher specific power density (kW/kg). Though, considering the power ratings involved in electric AGPS, above 50kW, the cost of the magnets and their size would make such a machine very expensive.

Furthermore, a wound-rotor has some safety advantages over a PM rotor, which is important in aeronautical applications. In case of system failure, a PM rotor continuously induces BEMF while the machine is rotating, which might lead to unsafe voltage levels. On the other hand, a wound-rotor machine if not excited by the power electronics, does not induce any BEMF, independently

of the machine rotation. In addition, PM rotors are more susceptible to vibrations and temperature variations, when compared to wound-rotors, which are a constant in the operating environment of the proposed system, this being the main landing gear.

Pertaining to the power of the EM used, it was primarily taken into account the accelerations and speed requirements of a typical taxiing [18], which can be found in Table 2.3.

Category	Typical values
Maximum speed	40km/h (11.11m/s)
Acceleration (0 to 40km/h)	40s

**Table 2.3 - Acceleration and speed requirements of typical taxiing**

The EM power can be estimated by:

$$P_{avg} = \frac{W}{\Delta t} \quad (2.1)$$

where  $P_{avg}$  is the average power given in watts (W);  $W$  is the work performed, in joules; and  $\Delta t$  is the time duration, in seconds. Also, the work can be given by:

$$W = \frac{1}{2} \cdot m \cdot (v_2^2 - v_1^2) \quad (2.2)$$

where  $m$  is the mass given in kg, and  $v_1$ ,  $v_2$  are the initial and final velocities, respectively, in m/s.

Considering the worst case scenario in terms of power demand, which would be an acceleration from standstill to 40km/h, and an airplane's weight of 70 tons, typical maximum take-off weight (MTOW) of a short-haul airplane, follows:

$$P_{avg} = \frac{\frac{1}{2} \times 70000 \text{ kg} \times (11.11 \text{ m/s})^2}{40 \text{ s}} = 108 \text{ kW} \quad (2.3)$$

This value is the double of the aforementioned 50kW, which is justified by the assumed MTOW and acceleration. Depending on the taxiing requirements and the size of the airplane, different average power values must be used.

The current state of development in synchronous machines with wound-rotors for high power applications enables specific power ratios of 1kW/kg [22]. Hence, in Table 2.4 are summarized the overall system weight and net weight, considering the fuel savings. The weight of the saved fuel was estimated considering a short-haul typical fuel capacity of 22,000 liters, a fuel density of 0.8kg/L and the 5.5% savings of the total fuel that the OET concept allows (see section 2.4.5). Furthermore, it was considered that 30% of the electric taxiing system weight is due to the power electronics.

Category	Weight
Electric taxiing system	130kg
Fuel Saved	968kg
Net weight	838kg

**Table 2.4 - Weights of the electric taxiing system, fuel savings and overall net weight**

As shown, the OET concept system, with synchronous wound-rotor EMs, not only compensates the extra weight introduced by the EMs and the power electronics, but also allows the airplane to be 838kg lighter due to the saved fuel weight.

Regarding the torque and speed requirements, depending on the synchronous machine mechanical characteristics, it should also be considered the introduction of a proper gear ratio (typically 5 to 10) to achieve the desired torque and speed.

#### 2.4.3 POWER SOURCE SPECIFICS

Traditionally the most common power network in airplanes encompasses a three-phase 115VAC 400Hz bus, together with a 28VDC bus [23], [24]. The 115VAC bus is powered from the engine mounted generators and is used to power the majority of the airplane systems. Wherever it may be required by a particular system, the power is converted locally to meet that demand in specific. Concerning the 28VDC system, it is used to start the APU and to operate crucial avionics systems, both before the main engines startup and in case of emergency after main engines failure. This DC bus is powered either from on-board batteries or from an emergency generator, such as a ram air turbine.

To face the continuous increase in the power requirements, the MEA initiative is changing the power network of the airplane, increasing the AC generation to three-phase 230/400VAC and introducing a 540VDC bus [23], [24] and [25]. The main purpose is to allow better utilization of the power networks, reducing power electronics size for local systems conversion, or even eliminate the necessity of local power conversion. Alongside, it is predicted the introduction of batteries in the new DC bus [26] to enhance grid acceptance of regenerated power.

Following this new trend, the power electronics of the concept proposed on this dissertation will use the 540VDC bus as its main power source. Therefore, the total current drawn by the system will be less than 200A (108kW), enabling the use of off-the-shelf and small-size power electronics. This allows for a contained weight of the power electronics, further improving system fuel gains by reducing the overall system weight. Furthermore, it will be possible to use the DC bus batteries as an energy buffer, storing the electrical energy recovered during the airplane roll and later powering the MLG machines during taxiing. In Figure 2.4 is shown a block diagram of the OET concept power grid.

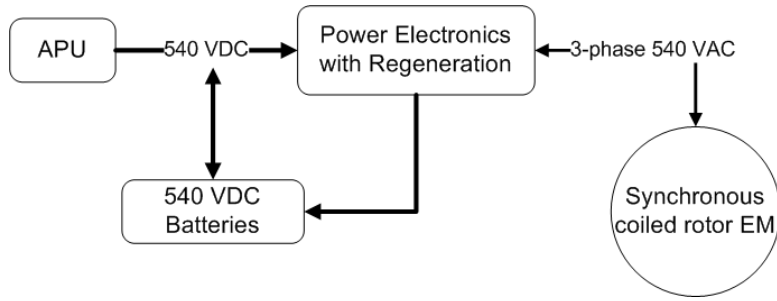


**Figure 2.4 - Block diagram representation of the power network for the proposed Concept of taxiing**

It will also be possible to retrofit this design on existing airplanes, where the 115VAC power grid is still used. The system will then be powered by the 115VAC, only requiring some changes to be made on power electronics.

#### 2.4.4 AIRPLANE INTEGRATION

The EMs are to be placed in the MLG, since it is where 90% of the airplane's weight lies. Therefore, traction should be performed there to improve system efficiency and safety. However, it must be taken into consideration system integration since the MLGs have friction brakes, so not only the volume available is smaller than in the NLG, but also there is a lot of heat production and considerable vibrations. In addition, the MLG supports the major impact on landing. All things considered, the EMs must have improved reliability to attain the mechanical and thermal requirements.

#### 2.4.5 SYSTEM SAVINGS

Taking advantage of the MEA power grid architecture, the proposed concept of electric taxiing with electrical energy recovery will reduce in 15% the fuel consumption during taxiing [11], when compared to other concepts of electric taxiing with no energy recovery systems. This results in 5-6% reduction in total fuel consumption. Furthermore, pollutant emissions during taxiing will be reduced in almost 100%, when compared to current taxiing. Both these achievements are due to all the taxiing to be performed only with APU in idle operation, since the electrical energy used to power the EMs in the MLG will have been recovered during the previous airplane roll. Hence, the APU fuel consumption and pollutant emissions will be lower, when compared to the situation where the APU has to power the EMs. In Table 2.5 are summarized the expected savings of the proposed system.

All things considered, this kind of technology has a market dimension of thousands of million euros per year, which is a very large figure on a time where efficiency is a major goal.

<b>Category</b>	<b>Advantages over traditional taxiing</b>
Fuel consumption	Reduction in 5-6% of total fuel consumption
Emissions	Reduction in 5-6% of total emissions and up to 100% during taxiing
Noise	Reduction due to non utilization of main engines
FOD avoidance while taxiing	Savings of 243.4 million €/year

**Table 2.5 - Major savings of the proposed concept of electric taxiing with electrical energy recovery over a traditional taxiing system**

## 2.5 PROTOTYPE APPROACH

For practical assessment of the technologies involved on this concept, was built a prototype of the power electronics necessary for practical implementation of the proposed concept. Therefore, was designed, built and tested a power module to control a three-phase synchronous machine with a wound-rotor. Although, due to equipment and budget restraints, the system was downsized to a smaller scale capable of being implemented and studied in the available laboratorial conditions. The following sections describe the chosen prototype approach.

### 2.5.1 POWER ELECTRONICS

A 1:10 scale was adopted in the construction of the power electronics, to cope with the aforementioned limitations. In Table 2.6 is detailed the reduction made to the system.

<b>Airplane scale</b>	<b>Prototype scale</b>
108kW	10kW
540VDC	100VDC
200A	100A

**Table 2.6 - Scaling between the real size power electronics of the airplane and the power electronics of the prototype**

Taking into account the application universe of the OET system, abrupt load variations and fast accelerations are not a major designing constraint, as it would be, for instance, in an electrical car application. The airplane's weight during taxiing varies less than 0.2%, if added to the fact that taxiways are almost plain ground, the load over the OET system can be considered to be practically constant. Hence, taking this into consideration in the design of the power electronics, a reliable, feasible and performing control architecture was adopted, over a more complex and resource demanding. The last would grant a better machine control over a wider range of situations, however this falls outside the scope of this dissertation.

## 2.5.2 ELECTRICAL MACHINE

The EM used in the prototype was a car alternator, also known as claw-pole alternator, which is a synchronous electrical machine with a wound-rotor. It has a three-phase stator and a claw-pole rotor with a single ring-form excitation winding, responsible for magnetizing all six pole pairs at the same time. In Figure 2.5 is depicted the structure of a claw-pole alternator.

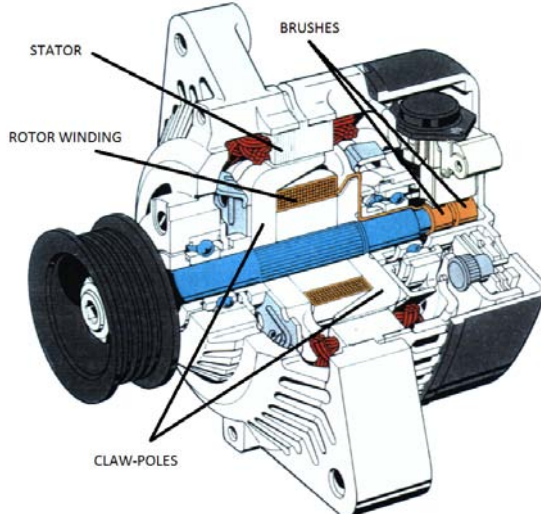


Figure 2.5 - Cutaway of a claw-pole alternator

## 2.5.3 TESTING STRUCTURE

A testing structure was built, containing all the power electronics, batteries, alternator and a 12 inches wheel (Figure 2.6). The connection between the alternator and the wheel was made through a chain.

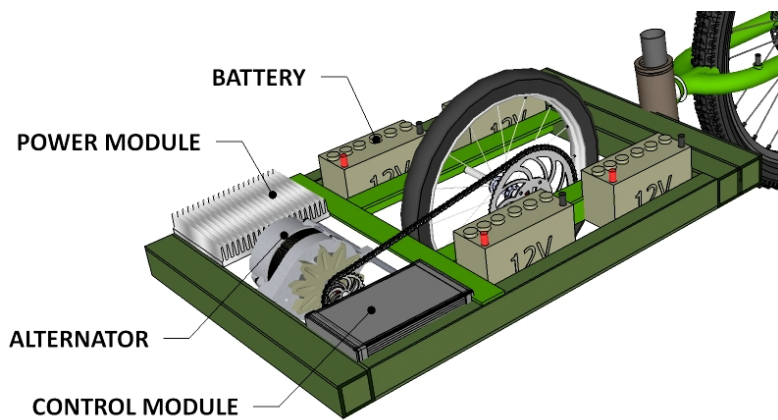


Figure 2.6 - CAD model of the testing structure

To perform tests under real conditions and retrieve data relative to the power consumption or energy regenerated, the structure can be connected to a vehicle where it would perform work. This vehicle can either be a bicycle or a motorcycle.

The following chapters address the development of the software and hardware that was designed, built and tested with the purpose of practically assess the performance of the technologies involved in the control of an EM for airplane taxiing, being this the main scope of this dissertation.

## 2.6 SUMMARY

This chapter introduced the concept of airplane taxiing, itemizing the major operational, safety and environmental issues that current taxiing cannot address. Therefore, two new approaches to airplane taxiing were presented: the dispatch towing concept and an autonomous ground propulsion system (AGPS). They both take airplane taxiing to all new standards, improving safety and achieving considerable fuel and environmental savings that represent millions of dollar per year for the aeronautical industry.

The AGPS concept, in particular electric AGPS, was chosen over dispatch towing as the basis of this dissertation. This system greatly improves the autonomy of an airplane in ground operations, while still attaining savings of 4% in total fuel consumption. It consists on placing an electrical machine (EM) in the landing gear, powered by the Auxiliary Power Unit (APU) of the airplane, allowing the airplane to perform all the ground movements without needing a tug or using the main engines.

An optimized electric taxiing (OET) concept was proposed, which added to a typical electric APGS the feature of electrical energy recovery during the airplane roll. This electrical energy is introduced in the power grid of the airplane and later used to power the electric taxiing. Comparing with electric AGPS, the OET concept allows higher fuel and emission savings (5.5%), since the APU load is smaller.

In the end, to assess the practical implementation of the OET concept, a layout of a prototype was defined.

# CHAPTER 3

## ELECTRICAL MACHINE CONTROL

---

In this chapter the principles behind electrical machines control theory will be presented, after which will be explained the control method implemented in the controller developed for the purpose of this thesis.

### 3.1 CONTROL PRINCIPLE

The EM used in this thesis was an automotive alternator, also known as claw-pole alternator. It has a three-phase winding structure in the stator and a rotor whose magnetic flux is created from coils, instead of permanent magnets.

From the control point of view, this machine is very similar to brushless DC machines (BLDC), so the control methodology is mostly based on BLDC control methods. Therefore, this type of EM requires a commutation sequence to be fed to the stator windings, creating a rotating magnetic field, in order to obtain the desired torque and rotational speed. This rotating field is generated electronically and for this purpose an electronic speed controller (ESC) had to be built.

The ESC has to determine the rotor position on each and every commutation and to do so, two methods can be employed: through the use of sensors (sensored control), or BEMF detection (sensorless control) [20], [21]. Once the rotor position is known, the ESC energizes each phase windings according to the chosen output voltage modulation technique, which will allow the machine to behave with the desired torque and speed.

The control process of an EM is graphically summarized in Figure 3.1.

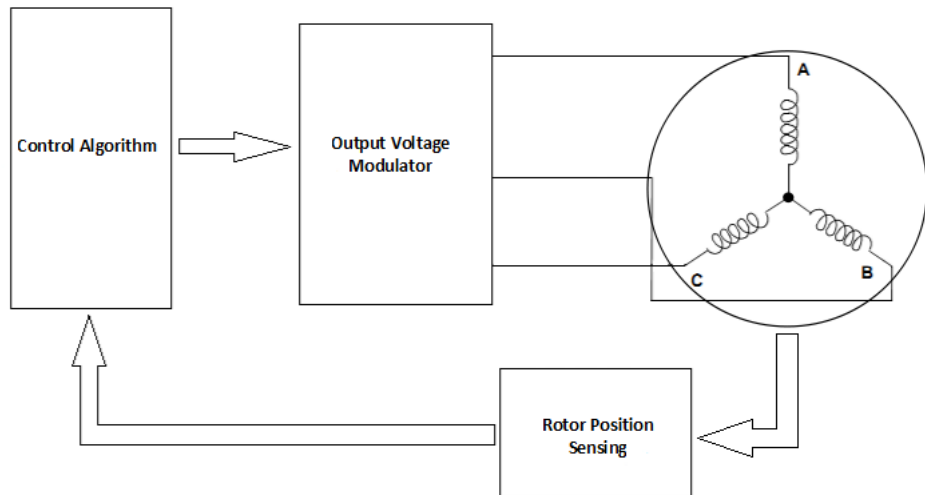


**Figure 3.1 - Graphical representation of a machine control method**

### 3.2 SENSORED CONTROL

To precisely determine rotor position one can employ shaft encoders, resolvers or, more often, Hall effect sensors [20], [21] and [27] that detect the rotor magnet position. The basic idea behind any given sensor is to sense the rotor or shaft position and output an analog or digital signal, which in turn allows the ESC to energize the stator windings in the correct sequence.

The more precise sensors are optical encoders and synchronous resolvers. They continuously give shaft absolute position with a very high degree of precision. Also it is possible to determine rotor speed by differentiating the position signal given by the sensors and all of this is independent of machine type.

But in some type of EMs, such as BLDCs, there is no need for continuous position detection: it is only needed to detect rotor position on every 60 degrees of the electrical cycle in order to properly commutate. These are the cases where Hall effect sensors are most used. Usually are used three Hall effect position sensors carefully placed on the rotor itself, in a way that they all have 60 or 120 electrical degrees offset from each other [27]. Each sensor element outputs a digital high level for 180 electrical degrees of electrical rotation, and a low level for the other 180 electrical degrees. This allows for each sensor output to be in alignment with one of the electromagnetic circuits. In Figure 3.2 is shown a diagram depicting the relationship between the sensor outputs and the required machine drive voltages.

The waveforms in Figure 3.2 are typical from an EM with trapezoidal BEMF and it is clearly seen the division of a complete electrical cycle in six portions of 60° each. Also, the period of each Hall sensor is a full electrical cycle and there is a 60° phase difference between them. This allows for a transition to occur, in one of the Hall sensors, at every 60° of the electrical cycle. This type of

cycle division is the keystone behind six-step commutation methods, explained in 3.4.4. The fact that BEMF voltages and phase currents should be in phase for optimal machine operation, in terms of torque/ampere output, is also visible.

Sensors tend to increase the cost and size of the machine and, most of the times, a special mechanical arrangement needs to be made for mounting the sensors. There is also the matter that some sensors, particularly Hall sensors, are temperature sensitive, which limits the machine operation to under  $75^{\circ}\text{C}$  [21]. On the other hand, they can also reduce the system reliability because of the use of components and wiring. In some applications it may not even be possible to mount any position sensor on the EM. Therefore sensorless control of EMs has been receiving great interest in recent years.

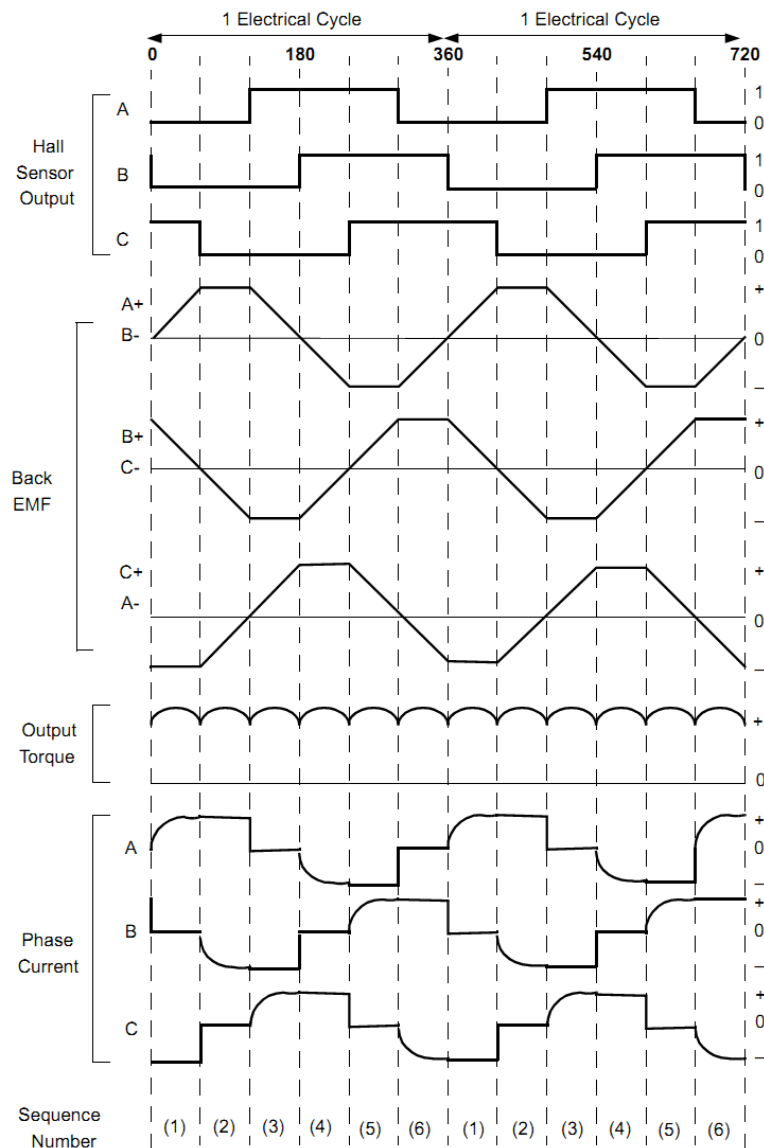


**Figure 3.2 – Hall sensor signal, BEMF, output torque and phase current waveforms of an EM with trapezoidal BEMF**

### 3.3 SENSORLESS CONTROL

Sensorless control methods can be divided in two major techniques, which are flux measurement methods and BEMF detection methods [28].

The flux measurement technique is complicated, needs machines parameters, and algebraic equations to estimate the position and the speed. It requires a powerful microcontroller (MCU) for mathematical computation. Hence, the methods of flux measurement are not favored for industrial and commercial applications [29], [30]. On the other hand, BEMF detection methods are very handy when it comes to cost and circuit complexity and they are becoming more widely accepted in industrial applications [30].

Many approaches have been followed for BEMF detection methods, including terminal voltage sensing; third harmonic BEMF sensing; freewheeling diode conduction; and BEMF integration [31]. Despite the fact that most of these methods face some accuracy, reliability and complexity problems, specially at low speed ranges [30], [32], terminal voltage sensing has been widely used in many commercial and industrial applications. Both the simplicity and low cost of this method make it quite attractive above the others mentioned.

It is worth mentioning that the continuous improvement in microcontrollers technology in the past few years allowed for more complex detection methods to be implemented, such as field-oriented control (FOC) algorithms [29], [33]. These are flux measurement techniques which require the measurement of each phase current and voltage and use some quite complex control algorithms for rotor position estimation. These algorithms significantly improve rotor position estimation, hence allowing better torque control, even at zero speed [33]. Nevertheless, the development and utilization of FOC control methods are, in some applications, too costly from a time and hardware perspective.

#### 3.3.1 FIELD-ORIENTED CONTROL (FOC)

Vector control techniques are used to achieve a high-performance machine control, characterized by a smooth rotation over the entire speed range of the machine, full torque control at zero speed, fast accelerations and decelerations. This kind of machine control, also referred to as field oriented control, is a reference in sensorless control, for its complexity, efficiency and cost.

The idea behind the FOC algorithm is to decompose a stator current into a magnetic field-generating part, and a torque-generating part [33]. Both components can be controlled separately after decomposition.

The basic structure of any vector control method can be summarized as follows [29] (see also Figure 3.3):

- Measure the EM quantities, phase voltages, and currents;
- Transform them into the two-phase system ( $\alpha, \beta$ ) using a Clarke transformation;
- Calculate the rotor flux space-vector magnitude and position angle;
- Transform stator currents into the d, q reference frame using a Park transformation;
- The stator current torque and flux producing components are separately controlled;
- The output stator voltage space vector is calculated using the decoupling block;
- The stator voltage space vector is transformed by an inverse Park transformation back from the d, q reference frame into the two-phase system fixed with the stator;
- Using space vector modulation (SVM) [34], the output three-phase voltage is generated.

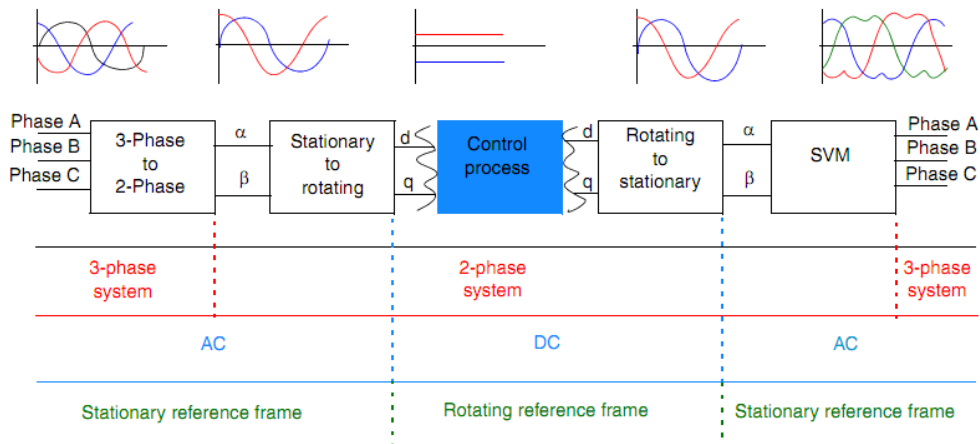


**Figure 3.3 – Vector control transformations**

To decompose currents into torque and flux producing components, the position of the EM magnetizing flux is needed. This requires accurate rotor position and speed information to be sensed. Incremental encoders or resolvers attached to the rotor are naturally used as position transducers for vector control drives. However, the aim of this topic is sensorless control, as so it is also possible to estimate this data from algorithms such as sliding mode observers [33].

### 3.3.2 BEMF SENSING AND ZERO CROSSING POINT (ZCP)

Among the mentioned methods for BEMF detection, terminal voltage sensing arises as one of the most commonly used. Together with the cost and complexity benefits of this method over flux measuring ones, there are some worth mentioning advantages which made it quite attractive for the purpose of this thesis:

- It is suitable to be used on a wide range of EM and the method is easily implemented on both star (Y) and delta ( $\Delta$ ) connected three-phase machines;

- It requires no detailed knowledge of EM properties;
- It is relatively insensitive to manufacturing tolerance variations;
- It will work both for voltage and current control.

A very common voltage sensing control technique is the BEMF zero crossing point method [27], [32], [35] and [36]. This method is based on detecting the instances when the BEMF of an inactive phase is zero.

The BEMF voltage in the phase windings increases when the phase is connected to the positive bus of the power supply, and reduces when the connection is done with the return path. A ZCP takes place when the winding is left open during the commutation sequence. The combination of the ZCPs of the three phases is used to calculate the proper energizing sequence. However, there is a  $30^\circ$  phase difference between the ideal commutation moment and the time BEMF crosses zero [27], [32] and [35].

In Figure 3.4 it is represented the waveform created by each BEMF ZCP. This signal behaves in the exact same way as the Hall sensor signal, the only difference being the  $30^\circ$  phase difference between them. This phase difference has to be compensated, which can be done electronically or in hardware, by implementing a phase shift circuit/algorithm. Once the signal phase is shifted, all the three signals retrieved from the BEMF ZCPs when the phases were inactive, will allow a proper commutation control.

A very important aspect to consider is very low-speed operation and start from standstill. Since BEMF is proportional to the rotational speed, when the machine rotor is stopped, it is impossible to detect ZCPs in the BEMF because there is no BEMF to detect. Also, at very low-speeds, it might be difficult to detect zero crossings since the BEMF signal has low amplitude. To overcome both these problems, the machine is started from standstill in open loop, with no rotor position feedback. Once the rotational speed is sufficient to allow clean zero crossing readings, the control is switched to BEMF sensing.

Another aspect to take into careful consideration is how to detect the BEMF ZCPs, since the BEMF voltage measured on each phase is referenced to the EM neutral point [27], [32] and [37]. The problem arises because the machine neutral point is not always accessible. There are several methods to overcome this issue, being the three most common: BEMF voltage compared with half of the DC bus; BEMF voltage compared to a virtual neutral point; and BEMF voltage directly measured using analog-to-digital converters [38].

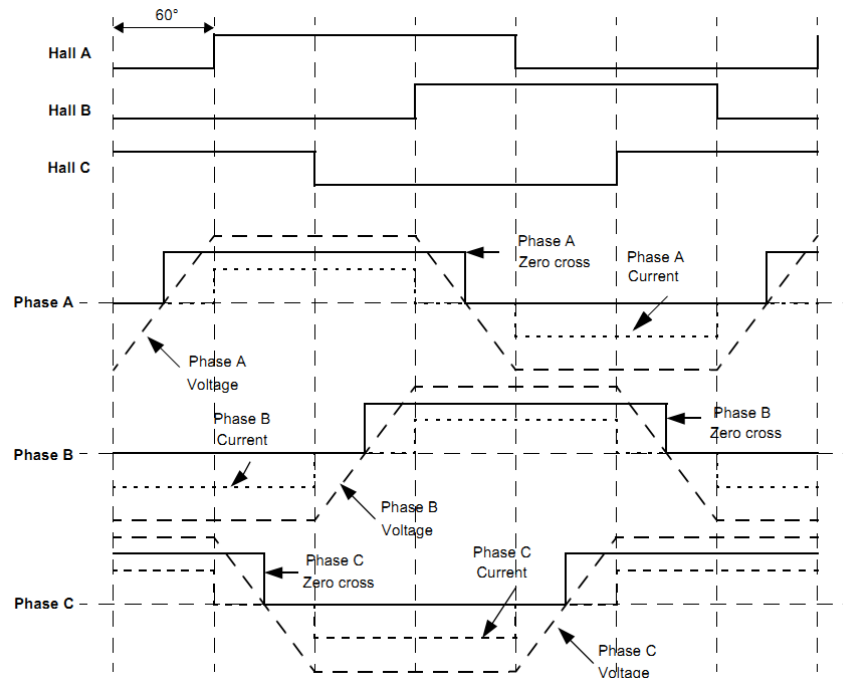


**Figure 3.4 – BEMF voltages, phase currents, phases zero crossing points and Hall sensor waveforms comparison**

### 3.4 VOLTAGE APPLICATION TECHNIQUES

After the rotor position is known and the next commutation in sequence is determined by the control algorithm, it is the turn of a voltage application technique to properly energize the power switches to attain the desired machine operation. The following sections describe the most common voltage application techniques.

#### 3.4.1 PULSE-WIDTH MODULATION

A pulse-width modulated (PWM) signal is a constant period square wave with a varying duty cycle. The term duty cycle refers to the pulse width itself, which is the amount of time in a period in which the square wave is on. Usually is given in percentage, corresponding to the reason between the on-time and the off-time of the square wave.

PWM can be used to reduce the total amount of power delivered to a load without losses normally incurred when a power source is limited by resistive means. This happens because the average power delivered is proportional to the modulation duty cycle. High frequency PWM power control systems are realizable with semiconductor switches. The discrete on/off states of the modulation are used to control the state of the switches, being the voltage across or current through the load proportional to the on time of the switches - Figure 3.5.

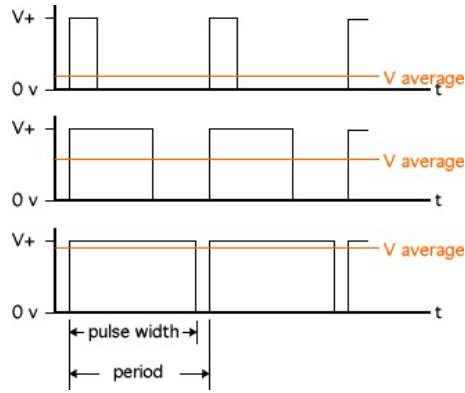


**Figure 3.5 - PWM signal and corresponding average voltage for different duty cycles**

Whenever the PWM signal is high, the switch is closed and the entire supply voltage is applied across the EM terminals. When the PWM signal is low, the switch is open and the supply voltage across the EM is zero volts. As a result, for a given pulse width corresponds an average voltage across the load.

This method is the basis of the majority of voltage application techniques available today.

### 3.4.2 SINUSOIDAL PULSE-WIDTH MODULATION (SPWM)

In many industrial applications, Sinusoidal Pulse-Width Modulation (SPWM), also called Sine coded Pulse-Width Modulation, is used to control the ESC output voltage. SPWM maintains good performance of the drive in the entire range of operation between zero and 78 percent of the value that would be reached by square-wave operation [34]. If the modulation index exceeds this value, linear relationship between modulation index and output voltage is not maintained and over-modulation methods are required.

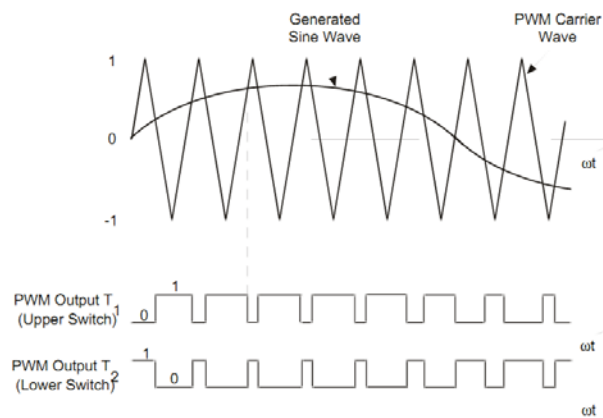


**Figure 3.6 - Sinusoidal pulse-width modulation schematic implementation**

In the most straightforward implementation, generation of the desired output voltage is achieved by comparing the desired reference waveform, called modulating signal, with a high-

frequency triangular carrier wave, as depicted schematically in Figure 3.6. Depending on whether the signal voltage is larger or smaller than the carrier waveform, either the positive or negative dc bus voltage is applied at the output.

### 3.4.3 SPACE VECTOR MODULATION (SVM)

The space vector modulation technique [34] is the most commonly adopted for the synthesis of the bridge ac voltages because it provides the best possible voltage gain (15% more than SPWM) [34]; the smallest ac current ripple with the lowest number of switching actions; the least amount of high-frequency circulating energy; and inherent suitability for transient operation.

A three-phase ESC, also called inverter and thoroughly explained in section 5.3, due to topological restrictions, may assume only eight switching combinations. This comes from the fact that a path must be provided for the main inductor currents and no short circuit must be applied in any leg of the bridge at any time. Also, from these eight combinations, only six of them yield non-zero voltage between phase windings a, b, c. In the space vector representation, these combinations correspond to the six non-zero discrete voltage vectors -  $V_{pn}$ ,  $V_{pp}$ ,  $V_{np}$ ,  $V_{nn}$ ,  $V_{nn}$ , and  $V_{pn}$  - and the two zero voltage vectors  $V_{pp}$  and  $V_{nn}$ , as depicted in Figure 3.7 a). The subscript letters p and n represent the circuit state: for instance  $V_{pn}$  corresponds to the state in which phase a is connected to the positive rail (p), while phases b and c are connected to the negative rail (n). These vectors, also called the switching state vectors (SSVs), form the SVM hexagon (Figure 3.7 a)), which is divided into six sectors. Each sector is defined by two non-zero vectors,  $60^\circ$  apart, whose node voltages differ in only one position, e.g.  $V_{pn}$  and  $V_{pp}$ .

In SVM, the rotating reference space vector of desired line voltages ( $V_r$ ) is synthesized at any given instant by PWM of its two adjacent SSVs and a zero vector. For the example in Figure 3.7 b)  $V_r$  is in sector II and it can be synthesized as follows:

$$V_r = d_1 \cdot V_{pn} + d_2 \cdot V_{pp} + d_0 \cdot V_0 \quad (3.1)$$

where  $d_1$  and  $d_2$  are duty cycles, given in period percentage, of the SSVs  $V_{pn}$  and  $V_{pp}$ , respectively, and

$$d_0 = 1 - d_1 - d_2 \quad (3.2)$$

is the duty cycle of the zero SSV,  $V_{pp}$  or  $V_{nn}$ .

The SVM technique can now be resumed in the following steps:

- Sector identification;
- Space voltage vector decomposition into directions of sector base vectors  $V_x$ , and  $V_{x \pm 60^\circ}$ ;
- PWM duty cycle calculation.

This method gives the greatest variability in arranging the zero and non-zero vectors during the PWM period. You can arrange these vectors to lower switching losses, or to reach a different result such as center-aligned PWM, edge-aligned PWM, minimal switching, and so on. For this reason is versatile enough to allow implementation of several vector control algorithms.

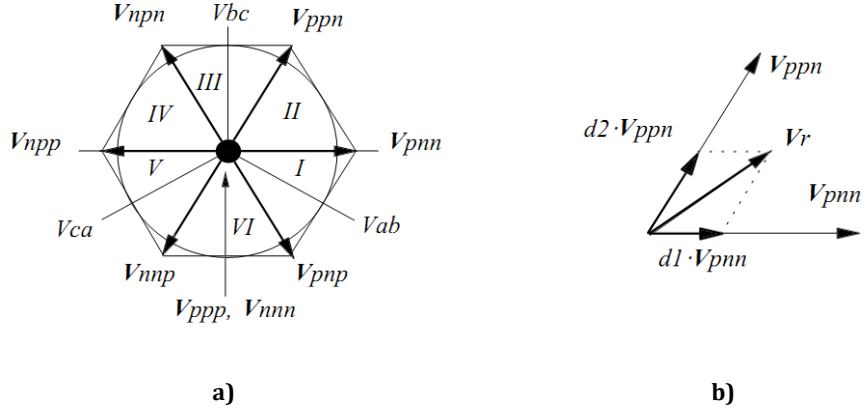


**Figure 3.7 - Space vector modulation representations: A) hexagon; B) reference vector addition**

### 3.4.4 SIX-STEP COMMUTATION

Between the methods referenced one of the most commonly used is the six-step commutation method. The specific feature of this commutation method is that one of the three phases is off at a time. That is why this method is largely used together with BEMF sensing methods, which require a zero current in the phase where BEMF is to be sensed.

During the commutation sequence there is one phase of the windings energized to the positive bus (current enters into the winding), the second phase winding is connected to the negative bus (current exits the winding) and the third phase is in a non-energized condition. The interaction between the magnetic field generated by the stator coils and the one generated in the rotor, either by permanent magnets or coils, creates the required torque. Ideally the peak torque occurs when these two fields are at  $90^\circ$  apart from each other.

In order to keep the machine running the magnetic field produced by the windings should shift position, as the rotor moves to catch up with the stator field. This is done by a three-phase inverter, where the rotor position is calculated and the correct winding phases are properly energized according to the determined rotor position [27], [36]. As a result it is created the commonly called rotating field, which can be more clearly understood in Figure 3.8.

A complete electrical cycle corresponds to  $360^\circ$  and the conducting interval of each one of the three phases, A, B and C, is  $120^\circ$ . The name six-step commutation comes from the fact that at every  $60^\circ$  of the electrical cycle there is a commutation of the conduction phases, in a total of six

steps for each electrical cycle. Also, a commutation at every  $60^\circ$  allows for the current to be in phase with BEMF, producing maximum torque [21], [39] and [40].

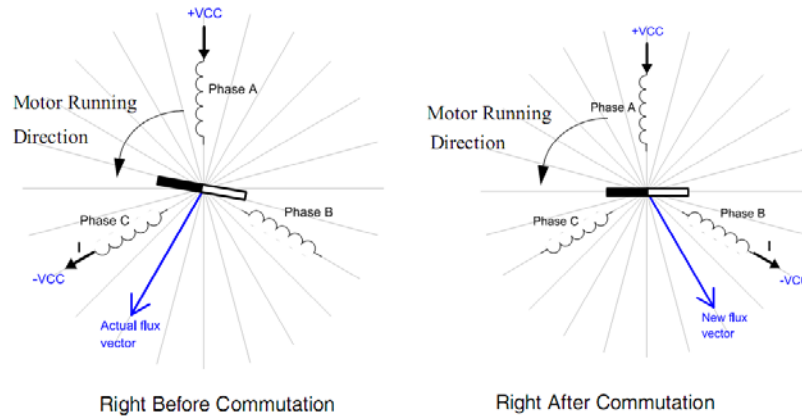


**Figure 3.8 - Six-step commutation stator field in relation to the rotor**

The commutation follows a certain pattern in every cycle [32], [40]:

- on the first step, the transistors T1 and T4 (Figure 3.9) are closed, and the current flows into the windings of phase A and exits through the windings of phase B;
- on the second step, the transistor T1 stays closed but T4 opens and now it is T6 that is closed, which makes the current to flow from the windings of phase A to the windings of phase C;
- on the third step, is now time for the transistor T6 to stay closed and it is T1 that opens and T3 that closes, which keeps the current flowing to the windings of phase C but now from the windings of phase B.

This process goes on for three more steps, until all the possible combinations occur, but always keeping the same current flowing principle, of always having one active phase in common between any two consecutive steps - Figure 3.9. After the six steps are completed and a complete electrical revolution is achieved, the process restarts from step one.

However, it is important to state that one electrical cycle may not correspond to a complete mechanical revolution of the rotor. The number of electrical cycles to be repeated to complete a mechanical rotation is determined by the rotor pole pairs. For each rotor pole pair, one electrical cycle is completed, so the number of electrical cycles to be completed before a complete mechanical rotation is equal to the number of the rotor pole pairs [27], [40] - Equation (3.3).

$$\text{Mechanical Rotation} = \frac{\text{Nr. of Electrical cycles}}{\text{Pole pairs}} \quad (3.3)$$

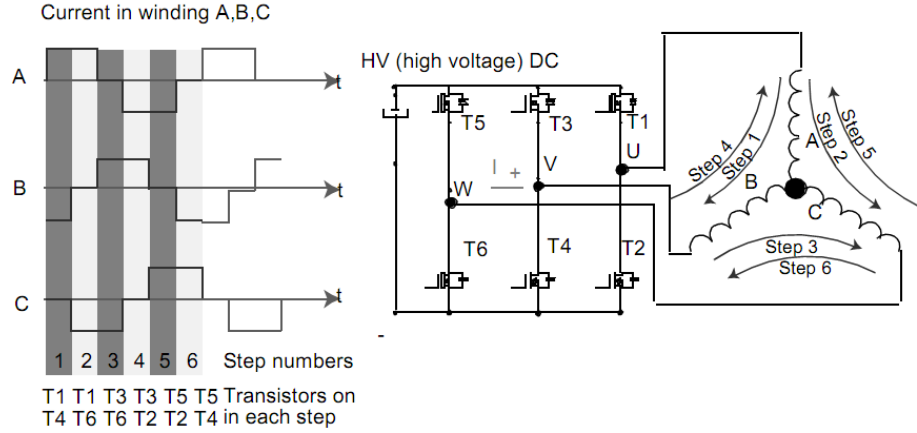


**Figure 3.9 – Six-step commutation method: phase waveforms representation on the left and inverter schematic perspective on the right**

### 3.5 CHOSEN CONTROL METHOD

The method chosen and implemented on this thesis was a sensorless technique that allows a simple hardware design, quite similar to what is used in Hall sensor-based commutation, together with a simple, yet performing, control algorithm.

#### 3.5.1 NEW VOLTAGE SENSING METHOD

For the purpose of this thesis, full torque control at zero speed and abrupt load variations were not the major constraints when it came to choose the control method. The hardware and software development was made with the intention of prototype testing and the system requirements established in section 2.5. As so, more important was the robustness, feasibility and cost/efficiency ratio of such a system. The degree of liberty given, permitted a system where load variation handling and start from stand-still could be achieved with BEMF sensing techniques.

Keeping in mind the keystones of the control approach, terminal voltage sensing, in the form of zero crossing point detection, was the elected technique. Many commercial applications use ZCP methods for sensorless machine control, which together with the advantages pointed in 3.3.2, show the potential of such technique.

However, there are several practical implementation problems when using the phase to neutral ZCP detection method. Firstly, the neutral voltage is required for comparison with the inactive BEMF, which sometimes is an issue, since the neutral voltage not always is accessible. There are some methods to overcome this matter [38], but all of them introduce signal noise and lead to ZCP detection deviations. Another issue is the requirement of a phase shift circuitry. Since the ZCPs of the conventional BEMF method are inherently 30 electric degrees ahead of the ideal

commutation points, a precise velocity estimator and a phase shift circuit, or digital filter, are needed to process the zero crossing signals so that accurate commutation points can be determined. If taken into account the additional open loop starting process, the sensorless ZCP detection based commutation turns out to be much more complex than the Hall effect sensor-based commutation. Still, much simpler than when compared to flux measurement techniques.

To address the aforementioned problems, a new terminal voltage sensing method was implemented [37]. Instead of detecting the EM terminal to neutral voltage, the estimated commutation signals are extracted directly from the average phase to phase voltage, using simple single-stage low-pass filters and low cost comparators. The output signals of the new detection circuit can be directly applied to a conventional six-step commutation table, as if they were obtained from real Hall effect sensors. This is possible since the estimated commutation signals are in phase with the ideal commutation points.

Unlike conventional solutions, this method does not require additional EM virtual neutral voltage, complex phase shift circuits, or precise speed estimators. Therefore, in terms of cost and reliability, this approach has obvious advantages over ZCP detection.

### 3.5.2 METHOD DESCRIPTION FOR SIX-STEP COMMUTATION

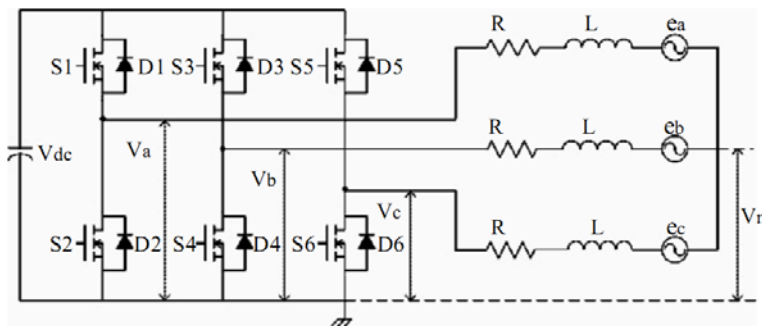


**Figure 3.10 - Inverter topology and electrical machine equivalent circuit, where R, L and e represent the winding resistance, inductance and BEMF, respectively [37]**

In a traditional inverter topology, the terminal voltage of each phase can be divided into three sub-sections, *i.e.* positive current conduction (current flows into the phase), negative current conduction (current flows out from the phase), and zero current conduction. It should be noted that each machine terminal is inserted between the upper and lower power switches, which are connected to the positive and negative sides of the DC source. Therefore it can be expected that the maximum and minimum terminal voltages will be fixed between  $V_{DC}$  and 0 - Figure 3.10.

When voltage application is done through a method such as six-step commutation, for a given torque or velocity command, a directly corresponding PWM signal is delivered to the inverter switches, controlling the amount of current flowing into the machine phases. If the terminal

voltages are expressed in the average form, *i.e.* in terms of duty cycle, the switching states can be eliminated - Figure 3.2. As so, the average terminal voltage of phase a can be derived as follows [37]:

$$V_a = d \cdot V_{DC} \quad \theta_e = 30^\circ \sim 150^\circ \quad (3.4)$$

$$V_a = \frac{(\theta_e + 30)}{60} (d \cdot V_{DC}) \quad \theta_e = -30^\circ \sim 30^\circ \quad (3.5)$$

$$V_a = (d \cdot V_{DC}) - \frac{(\theta_e - 150)}{60} (d \cdot V_{DC}) \quad \theta_e = 150^\circ \sim 210^\circ \quad (3.6)$$

$$V_a = 0 \quad \theta_e = 210^\circ \sim 330^\circ \quad (3.7)$$

where  $d$  represents the duty cycle, in percentage, and  $\theta_e$  the electrical angle in degrees. As for the average phase to phase voltage, from (3.4) and (3.5)-(3.7) one can express it as:

$$V_{ac} = d \cdot V_{DC} \quad \theta_e = 90^\circ \sim 150^\circ \quad (3.8)$$

$$V_{ac} = -d \cdot V_{DC} \quad \theta_e = 270^\circ \sim 330^\circ \quad (3.9)$$

$$V_{ac} = (-d \cdot V_{DC}) + \frac{(\theta_e + 30)}{120} (d \cdot 2V_{DC}) \quad \theta_e = -30^\circ \sim 90^\circ \quad (3.10)$$

$$V_{ac} = (d \cdot V_{DC}) - \frac{(\theta_e - 150)}{120} (d \cdot 2V_{DC}) \quad \theta_e = 150^\circ \sim 270^\circ \quad (3.11)$$

The same results can be obtained for the phases b and c with  $120^\circ$  and  $240^\circ$  phase difference.

According to (3.8)-(3.11), the zero crossing points of the average phase to phase voltage will occur at  $30^\circ$  and  $210^\circ$ , respectively. The phase relationship between the ideal BEMF waveform, the average terminal voltage, and the average phase to phase voltage, according to (3.4)-(3.11), is depicted in Figure 3.11.

It is easy to find that the average phase to phase voltage has an inherent phase angle difference of 30 electric degrees when compared with the BEMF. Namely, the zero crossing points of the phase to phase voltage are in phase with the ideal commutation points. According to this, the commutation points can be obtained directly from the three terminal voltages without including the neutral voltage and the phase shift circuit can be eliminated.

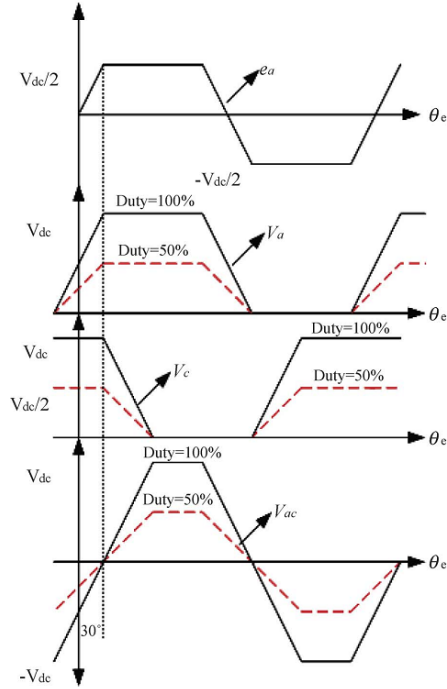


**Figure 3.11 - Phase relationship between BEMF ( $e_a$ ), average terminal voltage of phases a ( $V_a$ ) and c ( $V_c$ ) and average phase to phase voltage ( $V_{ac}$ ) [37]**

### 3.5.3 METHOD DESCRIPTION FOR SINUSOIDAL PWM

The rectangular current commutation, such as six-step commutation method, is known for its simplicity and ease of implementation. However, the time delay of the power switches and the effect of armature reaction, cause the armature current not to raise or fall instantaneously. As a consequence, periodic noise and torque ripple are generated in every 60 electrical degree commutation process [34]. In some cases, where high precision machine control is necessary, the mentioned issues are a major concern, and sinusoidal current commutation is adopted. This is an area of applicability of SPWM methods. If the high frequency terms are filtered with a proper low-pass filter, the average terminal voltage and the average phase to phase voltage can be expressed in terms of duty cycle as expressed in (3.12)-(3.17), respectively [37].

$$V_a = \frac{1}{2}d \cdot V_{DC} + \frac{1}{2}d \cdot V_{DC} \sin(\omega t) \quad (3.12)$$

$$V_b = \frac{1}{2}d \cdot V_{DC} + \frac{1}{2}d \cdot V_{DC} \sin(\omega t - 120) \quad (3.13)$$

$$V_c = \frac{1}{2}d \cdot V_{DC} + \frac{1}{2}d \cdot V_{DC} \sin(\omega t - 240) \quad (3.14)$$

$$V_{ac} = \frac{\sqrt{3}}{2} \cdot d \cdot V_{DC} \sin(\omega t - 30) \quad (3.15)$$

$$V_{ba} = \frac{\sqrt{3}}{2} \cdot d \cdot V_{DC} \sin(\omega t - 150) \quad (3.16)$$

$$V_{cb} = \frac{\sqrt{3}}{2} \cdot d \cdot V_{DC} \sin(\omega t - 270) \quad (3.17)$$

According to (3.12)-(3.17), the zero crossing points of the average phase to phase voltage  $V_{ac}$ , will occur at 30 and 210 electrical degrees respectively, which is same as the rectangular current commutation shown in (3.8)-(3.11).

As so, average terminal voltage equations (3.4)-(3.17), show that commutation signals can be generated with simple RC filters and comparators, as shown in Figure 3.12, without neutral voltage and phase delay circuitry.

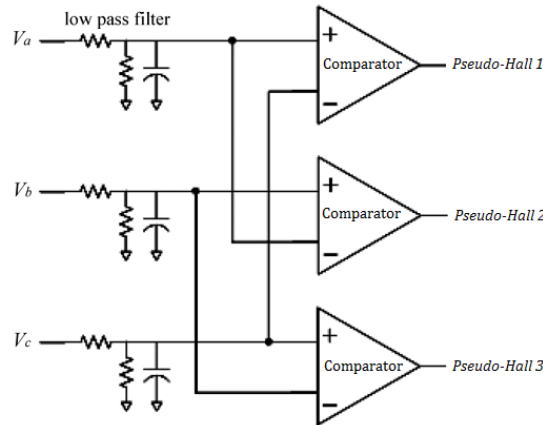


**Figure 3.12 - New terminal voltage sensing method circuit representation [37]**

### 3.5.4 COMMUTATION ERRORS COMPENSATION

A total of three rising edges and three falling edges occur over one electrical cycle, as depicted in Figure 3.4. This gives a fixed 60 electrical degrees separating each rising and falling edge. As a result, the average angular speed of the rotor  $\omega_r$  in rad/s, over 60 electrical degrees, can be estimated according to the following:

$$\omega_r = \frac{60\pi}{180 \cdot p \cdot t_{rf}} \quad (3.18)$$

where  $t_{rf}$  is the time between a rising and falling edge and  $p$  is the number of rotor pole pairs.

If taken into consideration the fact that speed does not vary significantly during each  $t_{rf}$ , the position of the rotor, in degrees, between each rising and falling edge can be estimated by [37]:

$$\theta_r = \theta_n + \left( \frac{180}{\pi} \right) \cdot \omega_r \cdot \Delta t_s \quad (3.19)$$

where  $n = 1 \sim 6$ ,  $\theta_1 = 30^\circ$ ,  $\theta_2 = 90^\circ \dots \theta_6 = 330^\circ$ , and  $\Delta t_s$  is the interpolation time period which is determined by the performance of the microcontroller used. Equation (3.19) reveals that the continuous position of the rotor can be obtained if the angular speed between each 60 electric degrees does not change significantly. This assumption is reasonable if the inertia of the system or the number of pole pairs of the rotor is large enough.

However, the utilization of a simple low-pass filter, introduces a small but fixed delay independent of rotor speed. With rotor speed increase, the percentage contribution of the fixed delay to the overall period increases, introducing a phase difference between the Pseudo-Halls signals and the BEMF. The phase delay angle, in radians, induced by the resistor-capacitor (RC) filter in terms of the machine frequency is given by [37]:

$$\phi_1 = -\tan^{-1} \left( \frac{CR_1R_2}{R_1 + R_2} \omega_e \right) \quad (3.20)$$

where  $R_1$  and  $R_2$  are the filter resistors,  $C$  the filter capacitor, and  $\omega_e$  the fundamental frequency of the terminal voltage. Also, in order to make the copper losses as low as possible, the current lagging angle, in radians, caused by the armature inductance is estimated using (3.21).

$$\phi_2 = -\tan^{-1} \left( \frac{L_a}{R_a} \omega_e \right) \quad (3.21)$$

where  $L_a$  represents phase a inductance and  $R_a$  phase a resistance.

Both the position errors introduced by the low-pass filter and the armature impedance are  $\omega_e$  dependant. As a consequence, appropriate compensation can be achieved if the angular speed of the rotor is known, which can be retrieved from (3.18).

To obtain an optimal commutation process, the rotor position can now be compensated for the errors mentioned, which gives:

$$\theta_r = \theta_n + \left( \frac{180}{\pi} \right) \cdot (\omega_r \cdot \Delta t_s + \phi_1 - \phi_2) \quad (3.22)$$

### 3.5.5 ROBUSTNESS

During machine operation, voltage spikes, as shown in Figure 3.13, are created by the residual current when the armature current is blocked by the power switches. This is the main cause for the commutation error in the conventional BEMF terminal voltage sensing method [32], [36]. In these methods, the BEMF is compared with the EM (virtual) neutral voltage or a fixed DC level, therefore the non-continuous voltage spikes will result in noisy (virtual) ZCPs. To deal with these noisy ZCPs, additional complex digital filters are indispensable, which definitely increase the complexity of the algorithm. As illustrated in Figure 3.13, the phase to phase voltage is not sensitive to the voltage spikes, *i.e.* the noisy ZCP will not occur during switching [37].

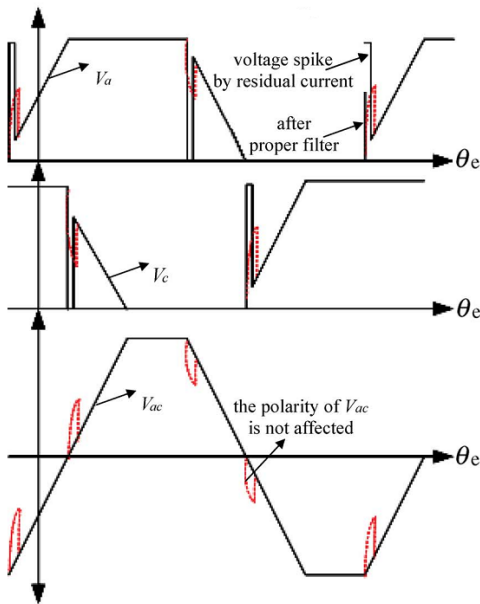


**Figure 3.13 - Voltage spikes in zero crossing detection for phase voltages a and c, and spikes absence in phase to phase voltage ac [37]**

The proposed method proves to be more robust and easier to implement than the conventional solutions.

### 3.6 SUMMARY

This chapter presented the principles of electrical machine (EM) control, which can be divided in two main areas: sensorless control and sensored control, depending on whether sensors are used or not to determine rotor position. For its advantages in cost and reliability, sensorless control is chosen as the basis of this dissertation and is thoroughly explained. It can be divided into flux measurements techniques, such as FOC, and BEMF sensing methods, such as ZCP. Taking into account the objectives and application scenario of this dissertation, BEMF sensing was the chosen approach.

A new BEMF sensing technique, consisting on average phase to phase BEMF voltage sensing, is thoroughly explained and chosen has the control strategy for the software built, explained in the following chapter. It allows an easily implemented, low cost and reliable control method, when compared to conventional BEMF sensing techniques. Also, it enables an efficient EM control, attaining the application requirements without recurring to the more complex and resource demanding vector control techniques.

# CHAPTER 4

## CONTROL METHOD IMPLEMENTATION

---

This chapter thoroughly describes the practical implementation of the control method, with special focus on the structure of the code and its programming in the microcontroller chosen. It is important to state that the code presented on this thesis was intentionally written by the student for the project in question. The chosen programming language was C.

### 4.1 CONTROL STRUCTURE

To implement a control algorithm such as phase to phase voltage sensing (PPVS), the basic structure of a sensorless, BEMF sensing, control algorithm was taken. A structure of this kind comprises three main stages (Figure 4.1):

- Alignment, where the rotor is forced to a known position, to ensure that when the six-step commutation begins the rotor is in its first step position;
- Open loop (OL), where a given speed ramp is given to the machine without the rotor position feedback, because BEMF is still too low to allow accurate estimation;
- Sensorless run or Lock mode, once the BEMF generated is enough to enable proper acquisition, rotor speed and commutation times start to be calculated according to the information retrieved from BEMF sensing.

#### 4.1.1 ALIGNMENT

In order to create enough startup torque and improve OL start conditions, there is a short time spawn, typically one second or less, during which the rotor is stabilized in a position given by the controller. This process basically consists on applying a PWM signal to only two phases of the EM, *i.e.* referring to six-step commutation, deliver a fixed step to the phase windings.

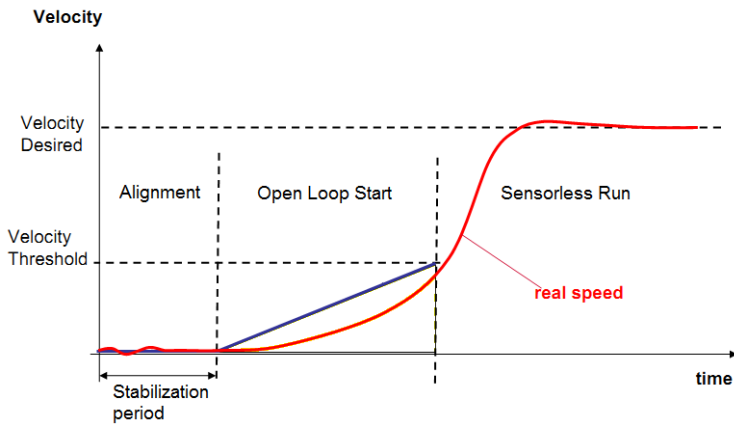


**Figure 4.1 – Sensorless control algorithm stages for a BEMF sensing method**

According to Figure 3.10 and equation (4.1), since the rotor is at standstill once the alignment stage begins, the current flowing in the phase windings will be only limited by the impedance of the winding, which is usually only a few ohms. For this reason, the duration of the alignment must be short, and it is advisable to also limit the current to a maximum value.

$$v = L \frac{di}{dt} \quad (4.1)$$

where  $v$  is the voltage in volts,  $L$  the inductance in henries and  $\frac{di}{dt}$  is the time derivative of the current in amperes/second.

Depending on the machine load, it might be necessary to tune the alignment parameters, namely the duration of the process and the duty cycle. When the machine load is significant, a longer duration together with a higher duty cycle is necessary to guaranty rotor stabilization. If the load is small or inexistence the values must be smaller, otherwise they might lead to rotor oscillation.

#### 4.1.2 OPEN LOOP START

Open loop start is the most critical stage in any sensorless BEMF sensing control method. The BEMF sensing method has the underlying condition that sufficient BEMF must be generated by the EM to enable accurate rotor position calculation. As so, when machine start is made with rotor at standstill, since BEMF is proportional to the rotational speed, it is first necessary to attain a minimum level of rotor rotation to enable BEMF sensing. This is accomplished with an OL start, during which the machine commutation starts without rotor positional feedback.

During this stage the commutation period is controlled by a velocity ramp established by the controller. As a consequence, the torque is lower and not constant. The rotor and stator flux need to be in an approximately 90 degree relation in order not to lose synchronization. Therefore, the position resonance can cause the rotor synchronization loss. This is even more

evident when load is taken into account. Careful calibration of OL ramp parameters has to be made in order to deal with load variations.

#### 4.1.3 SENSORLESS RUN

As soon as the BEMF produced by the machine is enough to enable good rotor position calculations, the control algorithm enters the sensorless run mode. It is often said that a lock on rotor position has been done. In this stage the machine remains at the desired speed or torque, according to user request. Also the EM is checked for locked rotor. This might happen when the machine is suddenly overloaded. Locked rotor detection is performed through comparison of the actual period and the average period. If the difference is too high for a predefined time, a locked rotor or incorrect commutation is detected and the commutation is stopped.

### 4.2 FIRMWARE

All the code was written in C programming language, using the development platform MPLAB® IDE v8.63, provided by Microchip. The MCU used, explained in section 4.2.5.4, also allowed Assembly programming language but the choice for C was obvious, because of the student familiarity with the language and the wide range of resources available in C language. For compilation, Microchip MPLAB® C30 v3.24 optimizing compiler was used. As far as possible, was made an extensive use of MPLAB® C30 16-bit Peripheral Libraries, which resulted in the final code, specially the MCU configuration, to be much more compact and user friendly. To program and debug the choice fell on Microchip PICkit 3 In-Circuit Debugger/Programmer, both for its simplicity and cost.

#### 4.2.1 FEATURES OVERVIEW

The code implemented comprises the aforementioned three main stages, together with:

- reading of three analog values, these being the user demand (potentiometer), DC bus voltage and current;
- calculation of rotor rotational speed according to the Pseudo-Halls signals, value that can be used to determine the stability of the Pseudo-Halls readings. Additionally can calculate rotor rotational speed with the signal retrieved from a single Hall effect sensor;
- software maximum current safety measure that shuts down all the PWM signals if the DC bus current becomes higher than a user-established value;
- locked rotor detection. Monitors the time between every commutation and stops the PWM firing if the value is higher than a user-established value;

- wait for potentiometer reset before restarting commutation. Useful for locked rotor situation or when OL start fails;
- control of rotor PWM duty cycle - user interface done with three buttons -, enabling field weakening [41] and a first degree of braking control capability;
- serial data sending of the power consumption, rotational speed, rotor PWM duty cycle and other optional parameters.

#### 4.2.2 HARDCODE CONFIGURATION

To improve code creation and manipulation, global variables were extensively used. This is more evident in the file `thesis_sensorless_PPVS.c`, which contains the main code. Since all the major variables are visible to all the functions, it is much easier to program; the function headings are shorter; the code becomes more simple; and the use or manipulation of data all across the code is more intuitive. Also this is the method chosen in many application notes [27], [36] and [42].

In addition, there are a set of user-modifiable software parameters that allows controlling code behavior and performance. Alongside, were created a set of flags to improve software status handling. For reference, a listing of all parameters and flags can be found in Appendix A.

#### 4.2.3 COMMUTATION VECTOR

To generate a six-step electrical cycle (see section 3.4.4), a commutation vector is used. This vector comprises six hexagonal values that codify a 16 bit configuration of the OVDCON register [43]. The upper half of the OVDCON register contains 8 bits, POVDxx, that determine which PWM I/O pins will be overridden. The lower half of the OVDCON register contains another 8 bits, POUTxx, that determine the state of the PWM I/O pin when it is overridden via the POVDxx bit. Therefore, it is possible to apply PWM signals only to the high/low side inverter switches, reducing switching losses on the low/high side switches, while achieving the same voltage control; and also to activate only two phases at a time, leaving one inactive, accomplishing the underlying principle of sensorless six-step commutation [36].

Sensored commutation [27] uses the three Hall sensors readings to codify a three bit binary number that works as a pointer to the commutation vector. The 16 bit OVDCON configuration retrieved is then used to correctly energize the EM phase windings. Over a complete electrical cycle, the three bit Hall sensor number obeys a certain pattern, this being 5, 4, 6, 2, 3, 1. It can occur either in a left to right, or right to left sequence, depending on rotor rotation being clockwise or counter-clockwise. Table 4.1 depicts the Hall sensor readings, the corresponding vector pointer retrieved and each phase energizing.

Sequence # (vector pointer)	Hall Sensor Input			Phase Energizing		
	A	B	C	A	B	C
5	1	0	1	Off	DC+ (PWM)	DC-
4	1	0	0	DC-	DC+ (PWM)	Off
6	1	1	0	DC-	Off	DC+ (PWM)
2	0	1	0	Off	DC-	DC+ (PWM)
3	0	1	1	DC+ (PWM)	DC-	Off
1	0	0	1	DC+ (PWM)	Off	DC-

Table 4.1 - Hall Sensor readings and phase energize sequence for six-step commutation

The PPVS control method used allows sensorless commutation to behave similarly to sensored commutation, since the Pseudo-Hall signal at the comparator output, with great accuracy, recreates the output of conventional Hall effect sensors. Hence, the three bit binary number read straight from the Pseudo-Hall registers can work as a pointer to the commutation vector.

However, if the commutation sequence has to be digitally simulated in the MCU, as it occurs during OL, a loop with programmable period must be implemented (see section 4.2.4.4). Moreover, by ordering the conventional commutation vector with the sequence given by the Hall sensors - 5, 4, 6, 2, 3, and 1 - and utilizing an incremental variable as pointer, the aforementioned Hall sequence can be simulated.

Hence, a total of four commutation vectors were created, they are all global variables at the beginning of the file thesis\_sensorless\_PPVS.c. The reason for this is to have two for PWM signals applied on the high side switches and other two for low side switches. Between these two vectors for each side switches, one is for a commutation sequence directly read from Pseudo-Hall signals; the other is ordered in a way that proper commutation can be generated straight from an incremental code variable.

#### 4.2.4 MAJOR FUNCTIONS FLOW CHARTS

The flow charts of the functions responsible for the actual implementation of the EM control algorithm are presented in Appendix B, these being: *main*, *START\_Motor*, *STOP\_Motor*, *CNInterrupt*, *T1Interrupt* and *Open2Lock\_transition*. In the following sections a brief, yet careful, description of the functions major details will be made.

##### 4.2.4.1 FUNCTION MAIN

This function, as the name indicates, is the main software function. It is where all the peripherals initialization is done, by calling several configuration functions (see section 4.2.5.4 for more

details); commutation start and stop decisions are made; and system calculations handling takes place.

The flow chart in Figure B.4 depicts in more detail the construction of function *main*. It can be seen the potentiometer safeguards implemented, to avoid false starts after commutation halts and when the function is executed for the first time. The first is achieved with the flag *WAIT\_POT\_RESET*, equaled true in function *STOP\_Motor*, which stops the commutation while the potentiometer reading does not reaches zero. But when the function is executed for the first time, a simple loop that only exits when potentiometer readings are equal to zero is used. Moreover, only when the potentiometer reading is greater than the value set by the *POT\_THRESHOLD* parameter, the commutation start decision is taken. This is a safety measure to avoid false starts due to noise in the potentiometer readings.

To call the function *START\_Motor*, not only the potentiometer reading has to be higher than the value set in *POT\_THRESHOLD*, but also the rotor cannot be already running - flag *ROTOR\_RUNNING = FALSE*. In the case when the potentiometer reading is lower than the threshold value and the commutation has already started - *ROTOR\_RUNNING = TRUE* -, the function *STOP\_Motor* is called.

Apart from the initial potentiometer check and peripherals initialization, all the function is inside a true cycle that at the end of every loop calls the function *System\_routines* (see section 4.2.5).

#### 4.2.4.2 FUNCTION START\_MOTOR

The alignment stage of the control algorithm was implemented on this function. As mentioned in 4.1.1 it is necessary to stabilize the rotor in a know position before the OL ramp begins.

Figure B.2 flow chart shows actual function organization. Before the alignment procedure it is first configured the initial electrical cycle frequency of the OL ramp, together with the initialization of the rotor PWM duty cycle. To properly align the rotor, a given commutation step is applied to the stator windings during an established time (*STABILITY\_DELAY*), and it is expected that the rotor aligns with the created stator magnetic field. This process is done two consecutive times, for two different commutation steps, granting better stabilization results. The duration and stator PWM duty cycle depend mainly on machine load and rotor PWM duty cycle.

At the end of the function, the flags that control commutation (*ROTOR\_RUNNING*) and OL ramp initiation (*OPENSTART\_ON*) are set true, enabling the next stage in OL machine start. Also, rotor beginning position in the OL ramp, which is the last commutation step applied to the stator, is passed to function *T1Interrupt*, where OL ramp has been implemented. This is important to keep at minimum the chances of rotor synchronization loss.

#### 4.2.4.3 FUNCTION STOP\_MOTOR

As depicted in the flow chart of Figure B.1, this function is responsible for: stopping the commutation process; the interrupt functions related with the commutation; and resetting all control flags to initial conditions.

#### 4.2.4.4 FUNCTION T1INTERRUPT

The OL ramp was implemented on this function. To determine rotor position based on BEMF sensing techniques, it is necessary to achieve a minimum level of rotor rotation, as referred in 4.1.2. In order to do so, during this stage the commutation period is controlled by a velocity ramp established by the controller, without rotor positional feedback.

The commutation period needs to be precisely controlled, so it is important to guarantee that the function which controls OL commutation is executed with minimum interference from the rest of the code. The MCU used (see section 4.2.5.4) is capable of handling interrupt functions, to which can be assigned one of seven priority levels defined by the user [43]. Once a process begins, the CPU can only be interrupted by a source with a higher user-assigned priority. As so, the OL ramp control was implemented in the interrupt function of TIMER1, to which was user-assigned a priority level only below *ADCInterrupt* and *CNInterrupt*. This means that *T1Interrupt* can only be halted by the functions responsible for ADC and change notification readings, respectively, and has execution priority above all the rest of the code. See section 4.3.8 for further details on user-defined interrupt priorities.

Actual implementation is depicted in Figure B.5. *T1Interrup* is configured in function main in the peripherals initialization, however it is the flag *OPENSTART\_ON* that handles the beginning of the OL ramp. Before any further decision, is verified if the electrical cycle period (register PR1) is smaller than the end ramp period (*RAMP\_END*). If true, it is assumed that an OL ramp failure has occurred and the function *STOP\_MOTOR* is called to stop the commutation. Though, if false, the variable *OLoop\_SECTOR*, which is the commutation vector pointer, is incremented to enable energize the EM windings with the next step in sequence.

The bottom half of *T1Interrup* is related to electrical cycle period (PR1) calculations. At first it is checked whether the actual value loaded into the PR1 register is smaller than a threshold value, defined by the user, below which the transition to sensorless run mode begins. Alongside, this decision also controls the shift between the two ramp stages that were specifically created. As mentioned, it is first necessary to attain a certain rotational speed for sufficient BEMF to be generated, and in order to do so there are two speed ramps that control the decrease of the electrical cycle period. The first encompasses a linear decrement of PR1 register by the value stored in *RAMP\_SLOPE* - equation (4.2) - and occurs in the first half of the ramp. The second

stage is non-linear, as shown in (4.3), where *RAMP\_SLOPE2* is a positive decimal smaller than one.

$$PR1 = PR1 - RAMP\_SLOPE \quad (4.2)$$

$$PR1 = PR1 - PR1 \times RAMP\_SLOPE2 \quad (4.3)$$

The reason behind this choice is to allow a steady increase of the electrical cycle frequency at an early stage of the ramp, and a more efficient OL commutation in the second half of the ramp to improve BEMF sensing.

Furthermore, in the first steps of the OL ramp the BEMF signals have a great amount of noise, caused by the PWM signals superimposed. As so, during the first stage of the OL ramp the function *CNInterrupt* is disabled and only on the second stage it is enabled, when Pseudo-Halls signals validation is more accurate. The process of validation is specifically implemented in function *Open2Lock\_transition*.

In [36] it is said that the electrical cycle frequency of an OL ramp should be between 1/60th and 1/6th of the rated EM speed. Having these constraints in mind and also the fact that phase to phase voltage is larger than the phase voltage itself, which improves BEMF detection, the parameters *RAMP\_START*, *RAMP\_END* and *RAMP\_THRESHOLD* (see Appendix A) were determined. According to equation (3.3) and the electrical machine details (see section 2.5.2), 1/60th and 1/6th of the rated EM speed, in terms of electrical cycles, are:

$$\frac{6600 \text{ rpm}}{60} \times 6 \text{ pole pairs} = 660 \text{ rpm} \rightarrow 11 \text{ Hz} \quad (4.4)$$

$$\frac{6600 \text{ rpm}}{6} \times 6 \text{ pole pairs} = 6600 \text{ rpm} \rightarrow 110 \text{ Hz} \quad (4.5)$$

where it is assumed a machine top rated speed of 6600 rpm and 6 pole pairs. In order to translate these values in Hz to the values that will be loaded on PR1, it is important to understand the PR1 incrementing process.

The module TIMER1 is configured with a prescaler of 1:64 [43] (see section 4.3.3), which means that the timer register is only incremented after 64 system clock increments. The system clock (FCY), see section 4.2.5.4, increments 29491200 times in a second, so TIMER1 counts a total of 460800 times in a second. However, the timer period register size is only 16 bit, which gives 65.536 ( $2^{16}$ ) increments total, after which the timer count is reset.

After practical experimentation on the system, and bearing this in mind, the parameters were defined as follows:

$$RAMP\_START = 8000 \quad (4.6)$$

$$RAMP\_END = 1000 \quad (4.7)$$

$$RAMP\_THRESHOLD = 4000 \quad (4.8)$$

The electrical cycle frequencies that correspond to the PR1 values mentioned are shown in (4.9)-(4.11).

$$RAMP\_START \rightarrow \frac{460800}{8000} \times \frac{1}{6} = 9.6\text{Hz} \quad (4.9)$$

$$RAMP\_END \rightarrow \frac{460800}{1000} \times \frac{1}{6} = 76.8\text{Hz} \quad (4.10)$$

$$RAMP\_THRESHOLD \rightarrow \frac{460800}{4000} \times \frac{1}{6} = 19.2\text{Hz} \quad (4.11)$$

All the values are divided by 6 since the function is executed a total of six times before a complete electrical cycle is completed (six-step commutation). It is important to mention that practical tests showed that the shift to sensorless run is made shortly after the threshold value. The *RAMP-END* works only as a safety limit that if reached stops the commutation. Therefore, it is evident the improvement obtained by the PPVS method in low speed commutation, when compared to (4.4) and (4.5).

#### 4.2.4.5 FUNCTION OPEN2LOCK\_TRANSITION

This function implements auxiliary calculus of function *T1Interrupt*. In order to stop the OL ramp and start sensorless run, it is first necessary to verify if the commutation vector pointer obtained from the Pseudo-Halls readings respects the commutation sequence, stated in 4.2.3. This is done by comparing the OVDCON configuration value pointed by the Pseudo-Halls (*PHallValue*), with the value pointed by the OL ramp pointer (*OLoop\_SECTOR*). If they are coincident twelve times, which corresponds to two complete electrical cycles, it is assumed that the Pseudo-Halls readings are valid, and sensorless run begins. This is controlled with the flag *OPENSTART\_ON* that halts the OL ramp and passes the commutation calculation task to *CNInterrupt*. The flow chart in Figure B.6 shows this function behavior.

#### 4.2.4.6 FUNCTION CNINTERRUPT

The sensorless run is implemented on this function. The PPVS method employed allows a direct reading of the Pseudo-Halls at the output of the comparators, which is directly converted to a pointer of the commutation vector, determining the commutation sequence and timing. The flow chart in Figure B.3 illustrates this process.

The *CNInterrupt* is the highest priority function, since it performs the most crucial task during machine operation, this being the determination of the commutation step to be loaded into the OVDCON register. Also, it is where a rotor locked situation is checked. The counter variable *Rotor\_locked* is incremented in each TIMER2 interrupt and checked for overflow, and it can only

be reset to zero in the evidence of a new commutation step. Since the commutation is controlled by the Pseudo-Halls readings in *CNInterrupt*, if the rotor is locked there will be no variation in the readings, causing the overflow.

#### 4.2.5 REAL-TIME UPDATES

In the following sections will be summarized the real-time routines preformed in the software. All of them are contained in the function *System\_routines* and have an execution frequency according to what established in the *REALTIME\_UPDT* parameter.

##### 4.2.5.1 MCPWM DUTY CYCLE CALCULATION

To calculate the duty cycle of the MCPWM module, equation (4.12) is employed.

$$Duty\_CALC = \frac{Potvalue}{1024} \times PTPER \quad (4.12)$$

Since the ADC result output format is configured to integer, for a 10-bit ADC value, such as *Potvalue*, the range will be between 0 and 1024. A duty cycle value equal to *PTPER* results in all the power to be applied to the EM; and a duty cycle of *PTPER*/2 results in half the power to be applied to the EM. This way, it is possible to control the average power supplied to the EM windings with the variable *Potvalue*. Moreover, the speed of the EM is directly proportional to the power supplied, so varying the PWM duty cycle linearly from 0% to 100% of *PTPER* will result in a linear speed control from 0% to 100% of the maximum speed [27], [40].

Due to dead time insertion, to avoid PWM distortion [43] it is necessary to limit the duty cycle range to maximum and minimum values. These are defined in the parameters *DUTYC\_MIN* and *DUTYC\_MAX*.

##### 4.2.5.2 PSEUDO-HALLS FREQUENCY

The calculation of the Pseudo-Halls frequency is based on the input capture values and is shown in equation (4.13).

$$Hall\_Speed_BEMF = \frac{FCY}{IC\_period \times TIMER3\_PRESCALE} \quad (4.13)$$

##### 4.2.5.3 ROTOR ROTATIONAL SPEED

Taking into account equation (3.3), follows that rotor rotational speed is equal to:

$$Rotor\_Speed_BEMF = \frac{Hall\_Speed_BEMF}{POLE\_PAIRS} \quad (4.14)$$

##### 4.2.5.4 DC BUS CURRENT AND VOLTAGE

To calculate the DC bus current, equation (4.15) is applied.

$$BatCurrent\_CALC = \frac{BatCurrent - IBAT\_OFFSET}{IBAT\_FACTOR} \quad (4.15)$$

This value is limited to a maximum DC bus current value defined in *CURRENT\_THRESHOLD*. If greater, PWM commutation is disabled.

To calculate the DC bus voltage, equation (4.16) is applied.

$$BatVoltage\_CALC = \frac{BatVoltage - VBAT\_OFFSET}{VBAT\_FACTOR} \quad (4.16)$$

### 4.3 MICROCONTROLLER IMPLEMENTATION

Regarding the MCU implementation, the choice fell on dsPIC30F4011 by Microchip [44], belonging to the dsPIC30F family. It is a high-performance, 16-bit digital signal controller, which features a motor control PWM module (MCPWM). Given that EM control was the primary concern, the choice is well sustained by this module. Also, it posses all other important features, such as an advanced 10-bit analog-to-digital (A/D) converter; two UART modules with FIFO buffers; 16-bit input capture functions; 16-bit timers with optional pairing into 32-bit timer modules; high-current sink/source I/O pins (25mA/25mA); seven user-selectable priority levels for each of the 30 interrupt sources; low cost, low-power and fast operation; and also C compiler optimized instruction set architecture.

The developed software uses 318 bytes of data memory storage, which represents only 15% of total memory. The rest of the device memory is available as dynamic storage for the software stack. It is important to refer that an external oscillator was used with a frequency of 7.3728 MHz, which together with a PLL of sixteen gives a clock frequency of 117.9648 MHz (FOSC). Though, each instruction needs four clock cycles to complete, resulting in an instruction frequency of 29.4912 MHz (FCY). Table 4.2 summarizes the major configuration bits settings.

Category	Setting
<b>Primary oscillator mode</b>	XT with PLL 16x
<b>Watchdog timer</b>	Disabled
<b>Low-side PWM output polarity</b>	Active high
<b>High-side PWM output polarity</b>	Active high
<b>Master clear enable</b>	Enabled
<b>Communication channel select</b>	Use PGC/EMUC and PGD/EMUD

Table 4.2 - dsPIC30F4011 major configuration bits settings

#### 4.3.1 ADC CONFIGURATION

The ADC module is of foremost importance to this project since it is where the potentiometer, DC bus current and voltage readings take place. Concerning the configuration, Table 4.3

summarizes the most important settings [43]. The code was written according to MPLAB® C30 16-bit Peripheral Libraries functions.

<b>Category</b>	<b>Setting</b>
<b>Idle mode operation</b>	Stopped
<b>Result output format</b>	Integer
<b>Conversion trigger source</b>	MCPWM
<b>Auto sampling select</b>	Auto sampling on
<b>Simultaneous sampling</b>	Sample individual
<b>Voltage reference</b>	AVDD and AVSS
<b>Scan selection</b>	Scan on
<b>A/D channels utilized</b>	CH0
<b>Number of samples between interrupts</b>	3 samples
<b>Buffer mode select</b>	Buffer off
<b>Alternate input sample mode select</b>	Input off
<b>Auto sample time bits</b>	2 TAD
<b>Conversion clock source select</b>	System clock
<b>Conversion clock select</b>	8 Tcy
<b>Pins selected to be configured into ADPCFG</b>	AN6, AN7 and AN8
<b>Scan select parameter configured into ADCSSL</b>	Skip AN0, AN1, AN2, AN3, AN4, AN5

Table 4.3 - dsPIC30F4011 ADC module configuration

The conversion trigger source is configured to be given by the MCPWM module, hence allowing better readings by decreasing PWM interference.

Furthermore, it was necessary to calibrate the ADC readings referring to DC bus current and voltage. As so, it was experimentally determined that for the DC bus current, with a four wire shunt of  $1.2\text{m}\Omega$  (see section 5.3), the ADC value was 6.5 for each ampere, value that was loaded to the parameter *IBAT\_FACTOR*. Also, the value of *IBAT\_OFFSET* was determined to be 514. This value is approximately half of the maximum readable value, which is 1024 ( $2^{10}$ ). That is in accordance to what was designed since the system is supposed to measure the same amount of positive and negative current.

Referring to DC bus voltage measurements, it was verified that the ADC value was 10 for each volt, so to *VBAT\_FACTOR* was given the value of 10. There is also a small offset to be calibrated which was determined to be 13 in the ADC readings.

#### 4.3.2 UART CONFIGURATION

In order to keep track of the power consumption of the system, rotational speed and rotor PWM duty cycle, between others, the UART module was used to establish a RS232 connection between the dsPIC® and a USB computer port. A serial-to-USB converter was used to enable this. Table 4.4 summarizes the most important settings [43].

Category	Setting
<b>Baud rate</b>	115200
<b>UART2 Status</b>	Enabled
<b>Idle mode operation</b>	Continue operation
<b>Alternate I/O selection bit</b>	Use U2TX and U2RX I/O pins
<b>Wake-up during sleep mode</b>	Disabled
<b>Loopback mode</b>	Disabled
<b>Parity and data selection</b>	8 bits without parity
<b>Stop bit</b>	1 Stop bit
<b>Transmission interrupt mode</b>	Interrupt when transmission buffer is empty
<b>Transmit break</b>	No break, UxTX pin operates normally
<b>Transmit</b>	Enabled
<b>Receive interrupt mode</b>	Interrupt when Receive buffer is 3/4 full
<b>Address character detect</b>	Disabled for data reception

Table 4.4 - dsPIC30F4011 UART module configuration

#### 4.3.3 TIMERS CONFIGURATION

It is of most importance the TIMERS configuration, since they are directly related to rotor PWM generation (Output compare), OL ramp creation (*T1Interrupt*), rotor locked detection and Pseudo-Halls period calculation. As so, a total of three TIMERS were used and their configuration [43] is listed in Table 4.5. The code was written according to MPLAB® C30 16-bit Peripheral Libraries functions.

Category	Setting
<b>TIMER1</b>	
<b>Period</b>	Defined by open loop ramp parameters
<b>Gated time accumulation</b>	Disabled
<b>Idle mode operation</b>	Stopped
<b>Input clock prescale</b>	1:64
<b>Clock source</b>	Internal clock (FOSC/4)
<b>TIMER2</b>	
<b>Period</b>	Rotor PWM period ( <i>FPWM_ROTOR</i> )
<b>Gated time accumulation</b>	Disabled
<b>Idle mode operation</b>	Stopped
<b>Input clock prescale</b>	1:1
<b>Clock source</b>	Internal clock (FOSC/4)
<b>TIMER3</b>	
<b>Period</b>	Maximum allowed (0xFFFF)
<b>Gated time accumulation</b>	Disabled
<b>Idle mode operation</b>	Stopped
<b>Input clock prescale</b>	1:256
<b>Clock source</b>	Internal clock (FOSC/4)

Table 4.5 - dsPIC30F4011 TIMER module configuration

Regarding TIMER1 settings, the choices are sustained by section 4.2.4.4. For TIMER2, section 4.3.5 presents explanation on period choice. As for TIMER3 period, the main concern is to have a

timer with the slowest increment rate possible. Hence, the period and prescale choices were the highest possible. This matter will be further explained in section 4.3.6.

#### 4.3.4 MCPWM CONFIGURATION

A major asset of dsPIC30F4011 is to comprise the motor control PWM module [43]. This module is specifically made to enhance power and motion control applications. A total of six PWM signals are necessary to control a three-phase inverter bridge (Figure C.5 on Appendix C), all of which were generated in this module. The code was written according to MPLAB® C30 16-bit Peripheral Libraries functions and the configuration can be found in Table 4.6.

Category	Setting
<b>Frequency</b>	15kHz
<b>Idle mode operation</b>	Stopped
<b>Time base Output postscale</b>	1:1
<b>Time base Input prescale</b>	Tcy
<b>Time base Mode</b>	Continuous Up/down
<b>Special event trigger time base direction</b>	Counting upwards
<b>Special event compare value</b>	0
<b>PWM I/O pairs 1, 2 and 3 Mode</b>	Complementary output mode
<b>PWM1H/2H/3H and PWM1L/2L/3L</b>	Enabled for PWM output
<b>Special event trigger output postscale</b>	1:16
<b>Immediate update</b>	Synchronized with PWM time base
<b>Output override synchronization</b>	Synchronized with PWM time base

Table 4.6 - dsPIC30F4011 MCPWM module configuration

The construction of the electrical machine determines its magnetic characteristics, which in turn has an influence on PWM frequency setting. High PWM frequencies result in higher switching losses, but are "filtered" by the machine parasitic inductance [27], [40]. This allows averaging the current on each phase windings to levels different from the DC bus current, enabling torque and speed control. Low frequencies determine that the current in the windings will be a series of high current pulses instead of the desired average current. After practical experimentation, a good machine behavior was attained for a PWM frequency of 15kHz.

Moreover, because the power switches cannot instantaneously change, some delay must be introduced between the turn-off event of one PWM output in a complementary pair and the turn-on event of the other switch. This delay, called dead time, is important to avoid unwanted short-circuits. Hence, programmable dead time was implemented.

#### 4.3.5 OUTPUT COMPARE CONFIGURATION

Besides the six PWM signals necessary to control a three-phase inverter bridge, it was also necessary to have a seventh PWM signal to control the rotor magnetic field. The output compare

module enables PWM signal creation, and so OC4 was used. Table 4.7 lists the module configuration.

Given rotor magnetic characteristics, mainly its inductance, practical experimentation showed a good machine behavior when the rotor PWM frequency (FPWM\_ROTOR) was 1kHz. This value is much lower than the one defined for MCPWM, being the main reason the fact that the rotor inductance is much higher than the stator inductance.

Category	Setting
<b>Frequency</b>	1kHz - defined by TIMER2 period
<b>Idle mode operation</b>	Continue
<b>Timer source</b>	TIMER2
<b>Mode</b>	PWM mode on OC4, Fault pin disabled

Table 4.7 - dsPIC30F4011 OUTPUT COMPARISON module configuration

#### 4.3.6 INPUT CAPTURE CONFIGURATION

To determine rotor rotational speed, the period of the Pseudo-Halls signals was calculated. The input capture enables this by capturing a timer period content when triggered by a configured event [43]. In this particular case, the event was the edges of the square wave at the comparator output, *i.e.* the Pseudo-Hall signal. The period calculations were realized upon two signals, in the IC7 and IC8 pins, both configured in the same way. The code was written according to MPLAB® C30 16-bit Peripheral Libraries functions and Table 4.8 shows the module configuration.

Category	Setting
<b>Idle mode operation</b>	Stopped
<b>Timer source</b>	TIMER3
<b>Number of captures per Interrupt</b>	1 Capture
<b>Capture mode</b>	Every edge

Table 4.8 - dsPIC30F4011 INPUT CAPTURE module configuration

The reason of this module operation is to measure the period of the Pseudo-Halls signals. As so, if the timer period is smaller than the signal period, it will be impossible to correctly relate two consecutive edges of a signal in the same time scale. So it is necessary to assure that the timer period is greater than the signal period for the period calculations to be valid.

#### 4.3.7 CHANGE NOTIFICATION CONFIGURATION

The change notification module enables an interrupt generation (*CNInterrupt*) whenever there is a change of state (high-to-low or low-to-high) in one of the Pseudo-Halls signals. These signals are square waves and the high or low state of the three, at a given time, codify a binary pointer to the commutation table. This allows direct commutation based on the Pseudo-Halls.

The pins CN5, CN6 and CN7 were configured to generate an interrupt on every input change and the internal pull-ups were enabled. This was necessary because the comparators outputs were open-collector.

#### 4.3.8 INTERRUPTS CONFIGURATION

The dsPIC30F4011 allows up to seven user-selectable priority levels for each interrupt source. The highest interrupt priority level is 7 and the lowest is 1 [43]. In Table 4.8 are summarized the priority levels of the interrupt functions in use.

Interrupt function	Priority level
<i>CNInterrupt</i>	6
<i>ADCInterrupt</i>	5
<i>T1Interrupt</i>	4
<i>T2Interrupt</i>	3
<i>IC7Interrupt</i>	2
<i>I87Interrupt</i>	2
<i>U2TXInterrupt</i>	1
<i>U2RXInterrupt</i>	1

Table 4.9 - Software interrupt functions priorities

## 4.4 SUMMARY

In this chapter was thoroughly explained the software created for EM control. The control algorithm comprises three main stages: alignment, open loop (OL) start and sensorless run. The first was implemented in the function *START\_Motor*, followed by the OL start implemented in function *T1Interrupt*, and the last stage was realized in function *CNInterrupt*. These three functions, together with functions *main*, *STOP\_Motor*, *Open2Lock\_transition*, of foremost importance to the software, were thoroughly analyzed with the support of the flow charts presented in Appendix B.

Moreover, all the dsPIC® configuration and programming was explained and itemized in tables to enable a more straightforward comprehension.

# CHAPTER 5

## HARDWARE DESCRIPTION

---

The controller used on this dissertation was thoroughly developed by the student, with the grounds of achieving a user-customizable, versatile and low cost development tool for electrical machine control. This chapter describes in detail all the development process, from the concept stage, through the Spice simulations, until actual implementation in hardware.

### 5.1 PURPOSE AND OVERVIEW

An EM controller comprises two main modules: the control module and the power module. In detail, the control module comprehends the MCU and all the electronics responsible for signal acquisition and conditioning; user interface; and power switches drive. The power module encompasses the power switches (MOSFETs, IGBTs, Thyristor) together with all the directly related electronics, such as power diodes, capacitors and shunt resistors. An electrical machine is directly connected to the power module terminals, and the control signals, that implement the control method, are given by the control module. The connection between the two can be made with or without isolation, usually in the form of opto-isolators. However, they are very expensive and only greatly used in power requirements much beyond this thesis purpose.

This dissertation focuses on electrical machine sensorless control, with emphasis on testing control methodologies. Hence, a fairly versatile platform where these solutions could be implemented was a key element to this project. The following sections describe what drove the student into the making of an EM controller from scratch, and a system overview is presented.

#### 5.1.1 PURPOSE

There are several market available solutions that enable testing of a desired control method. These are known as design kits, or development boards, and provide a user-modifiable platform

that allows control of a wide range of EMs. Microchip [45], [46], [47] and [48], Freescale [49] and International Rectifier [50], to reference some, offer many types of development boards. These go from low to high-voltage; opto-isolated to no isolation; text to graphical user-interface, between many other features. What they all have in common is programmable MCUs and some hardware versatility that allow the user to implement customizable control methods. However, a common denominator is the power handling capability, which, in most cases, is limited to less than 2kW. Concerning the prices, they vary between 100€ and 600€.

Furthermore, this project pretends to control a three-phase synchronous EM with a wound-rotor, which meant an architecture with an extra power control feature for the rotor. Though, the market available development boards are mostly targeted to three-phase EMs with permanently magnetized rotor or three-phase induction machines. As so, the controller developed on this dissertation aimed to deliver, at once, a high-power (up to 10kW), low cost (under 100€) and three-phase wound-rotor development board - Table 5.1.

<b>Category</b>	<b>Developed controller</b>
<b>Input Power</b>	10kW (maximum)
<b>Input Voltage</b>	100V (maximum)
<b>Input Current</b>	100A (maximum)
<b>PWM frequency</b>	10-20kHz
<b>Rotational Speed</b>	6600 rpm for 6 pole pairs (maximum)
<b>EM Phases</b>	three-phase
<b>Rotor</b>	Wound or Permanent Magnet
<b>Price</b>	approx. 70€

**Table 5.1 - Developed controller major requirements**

Additionally, it is of most importance for an engineering student to get in contact with all the development stages inherent to the solution of a given problem.

### 5.1.2 OVERVIEW

In Figure 5.1 is depicted the block diagram of the developed controller. The system uses Microchip dsPIC30F4011 digital signal controller, where the commutation sequence, rotational speed and torque are determined using the sensorless PPVS signals. All of the six stator PWM signals are applied through MOSFET gate drivers, being the rotor PWM the only signal directly applied to the MOSFET gate. A potentiometer is used to set the user-demand and three switches enable the user to directly control rotor PWM duty cycle. Also, the DC bus current is sensed through a four wire shunt resistor placed in the DC- terminal.

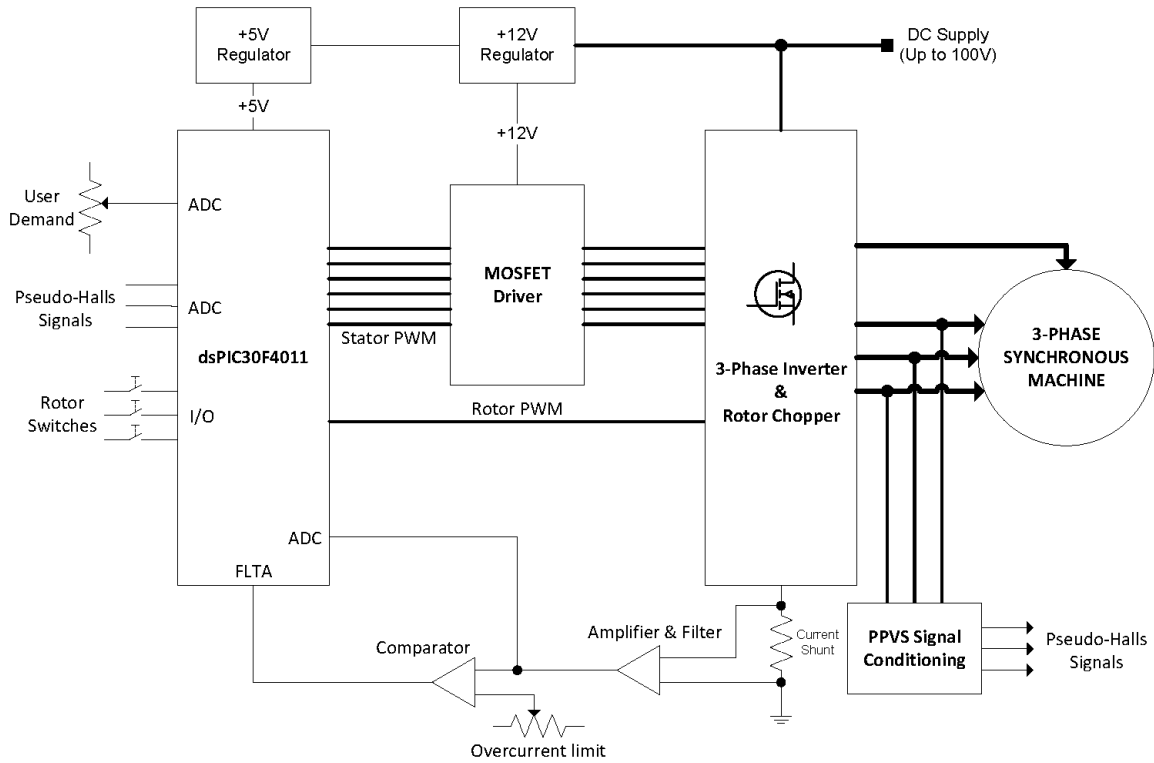


**Figure 5.1 - Developed controller block diagram**

The controller has the following features:

- Machine control interfaces:
  - Three-phase inverter bridge with a 10kW power rating
  - 2A MOSFET gate drivers with undervoltage protection
  - Additional wound-rotor control through chopper circuit
  - Hall sensors interface for sensored control
  - Gear-tooth speed sensor interface for sensored speed calculation
  - Phase voltage feedback for sensorless BEMF sensing control
  - Phase to Phase voltage sensing (PPVS) method implemented
  - Phase current sense four wire shunt for sensorless vector control
  - DC bus current sense four wire shunt
  - Overcurrent protection (FAULT pin [43])
- Input/Output interfaces:
  - Three switches for rotor PWM duty cycle direct control
  - Potentiometer for user-demand
  - LED indicator for PWM outputs
- Communication ports:
  - UART communication via RS-232
- Programming connectors:
  - RJ11 connector for dsPIC® programming

- Power connectors:
  - Cooper terminals for DC bus, EM phases and rotor connections
  - Auxiliary 12V power input connector for dsPIC® device and control circuitry
- Power module extra features:
  - Solder-free, for improved reliability
  - Compact and versatile

As a result, the developed controller (Figure 5.2) can be used in many scenarios, either for sensorless or sensored control, enabling implementation of various control methods. Moreover, it is possible to control several electrical machines, such as AC induction machines (ACIM); brushless DC (BLDC) machines; permanent magnet synchronous machines (PMSM); and synchronous machines with wound-rotor, which is a major asset among the market available solutions.

To develop the aforementioned controller, it was used the EAGLE PCB Design software v5.10 for PCB schematics and layout. In order to SPICE simulate the filters and specific circuitry, it was used the software LTspice IV v4.11. All the schematics are provided in Appendix C.

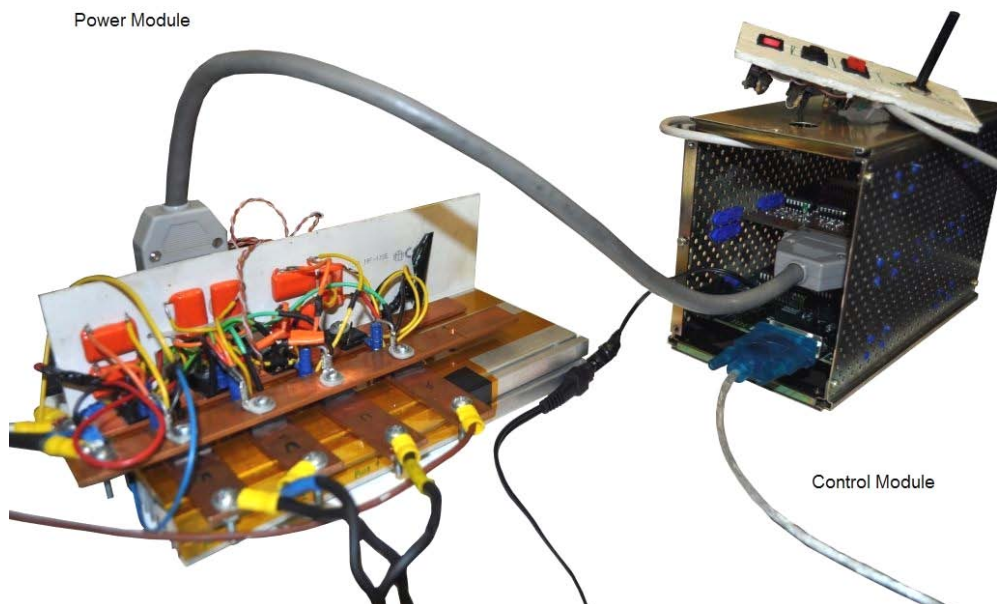


**Figure 5.2 - Developed controller overview**

## 5.2 CONTROL MODULE

This section addresses in detail the control module architecture and its features (Figure 5.3). It encompasses all the signal conditioning, user interface, dsPIC® and MOSFET gate drivers, which

makes it the keystone of the controller. Also, the development was made to support the design requirements shown in Table 5.1.

The dsPIC® interface and correspondent supporting circuitry was not developed by the student. In detail, the control module can be divided in two separate printed circuit boards (PCB), which are connected to each other: the EM control board and the dsPIC® board. The EM control board, which is the core of all the hardware for EM control, was entirely developed by the student and will be the main focus of the following sections. As for the dsPIC® board, it was developed by IPFN.

To mention that the control module was deliberately separated from the power module to further improve the controller versatility. Therefore, different power modules can be connected to this control module, depending on application requirements and machine type.

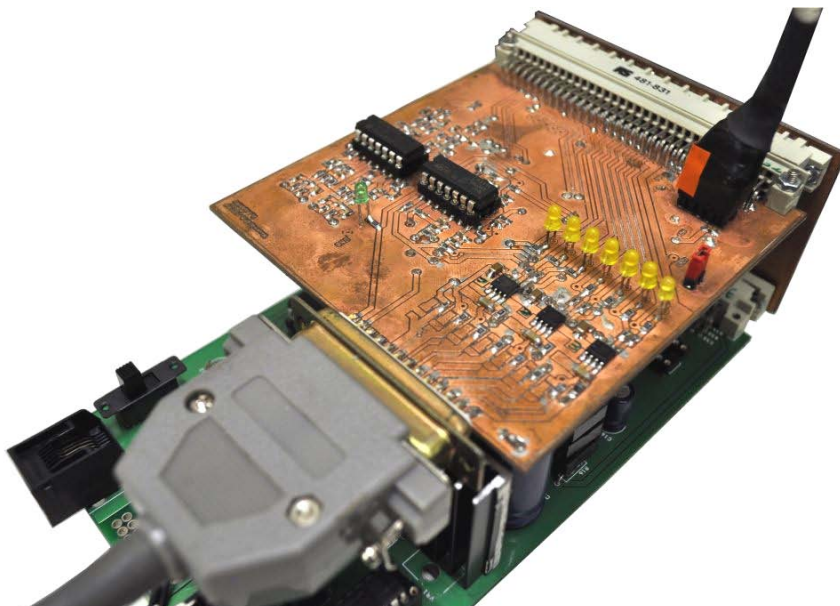


**Figure 5.3 - Control module developed for this thesis (dsPIC® and EM control boards)**

#### 5.2.1 dsPIC® CONTROL BOARD

For this thesis was used the dsPIC30F4011 [44] by Microchip, where the code was programmed. In order for it to work, a proper interface and supporting circuitry was provided by the dsPIC® board developed by IPFN (Figure 5.4). The board comprises:

- voltage regulators, which convert the 12V DC source into 5V that supply the dsPIC® and EM control board;
- serial communication/programming through a DB9 connector;
- dsPIC® programming through a RJ11 connector;
- a 96 pin DIN connector with all the dsPIC® I/Os, grounds and the voltage sources.

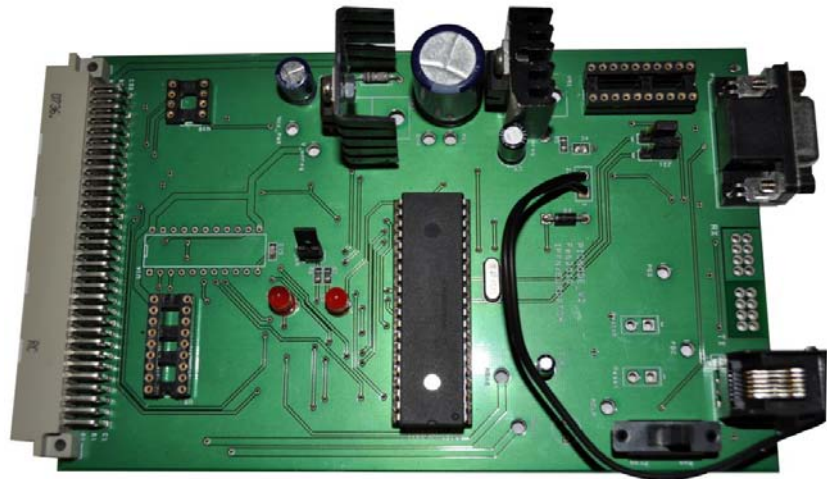


**Figure 5.4 - dsPIC30F4011 board developed by IPFN**

The dsPIC® board connects to the EM control board seen in Figure 5.3, through a backplane board containing two 96 pin DIN connectors.

### 5.2.2 EM CONTROL BOARD

The following sections describe in detail what was implemented in the EM control board.

#### 5.2.2.1 MOSFET GATE DRIVERS

In section 5.3.1 it is mentioned that the power switch choice for this dissertation fell on N-Channel MOSFETs. However, MOSFETs capable of handling the power requirements (10kW) defined for this controller inherently have a gate input capacitance of four to six thousands picofarads [51], [52]. Hence, to attain the established switching frequencies, it is necessary to use dedicated integrated circuits (IC) capable of rapidly charging the gate input capacitance. These ICs are called MOSFET gate drivers.

Also, the topology of a three-phase inverter imposes that the top side n-channel MOSFETs are not referenced to ground. As a consequence, the voltage of the PWM signal at the gate must be 10V to 15V higher than the source voltage [53]. There are many techniques to cope with this issue, but the most common is the bootstrap method, which was the one used on this thesis. On the other hand, to the low side MOSFET a simple current buffer is employed to increase the current of the dsPIC® PWM I/O.

#### Chosen driver

In order to choose a MOSFET gate driver, it was first taken into consideration the driver topology. There are single IC units capable of driving a total of six MOSFET gates, three high-sides and three low-sides; others are only for one half-bridge, meaning that can drive only one

high-side gate and the corresponding low-side. The later was the chosen to improve system reliability.

To narrow the drivers universe, the maximum voltage of the controller (100V) was taken into account. Also, it was preferable a high peak current, that could guarantee gate charging between the limits imposed by the PWM frequency. As so, the elected driver was the *LM5101BMA* from National Semiconductor [54]. This driver has the following characteristics:

- Supply voltage up to 118V DC;
- 2A of gate drive current;
- drives low-side and high-side n-channel MOSFETS (bootstrap method);
- supply rail undervoltage lockout;

It is important to mention the undervoltage lockout, which introduces an extra safety feature on the controller.

### Bootstrap dimensioning

The chosen driver employs a bootstrap method [51], [52] to drive the high side n-channel MOSFET (Figure 5.5).

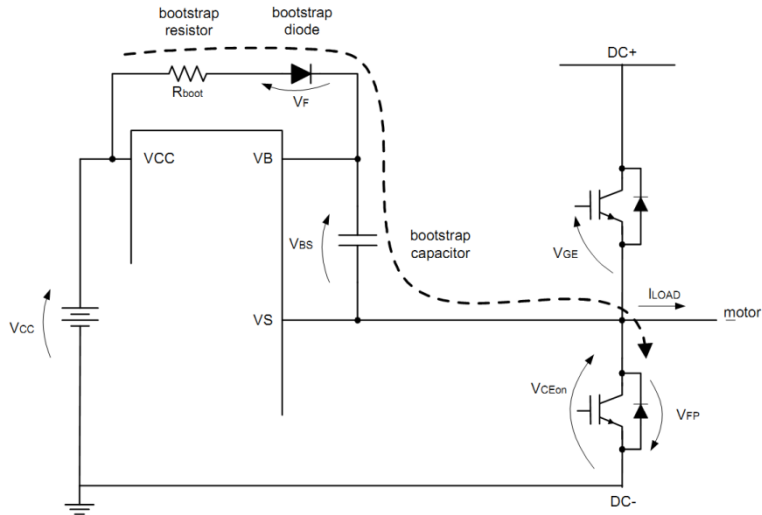


**Figure 5.5 - Bootstrap method schematic representation**

For a correct functioning of the driver, and particularly of the bootstrap circuit, it is important to determine the values of the bootstrap resistor, diode and capacitor [53], [55] and [56]. The resistor is placed in series with the diode so to limit the current when the capacitor is charged, and is usually not necessary. Concerning the diode, it is responsible for charging the bootstrap capacitor, has to be of fast recovery and able to block full power rail voltage, which is seen when the high-side MOSFET is switched on. However, the chosen driver already includes an internal

bootstrap diode, being the inclusion of the external diode only optional. This applies to cases when the internal diode is insufficient to charge the bootstrap capacitor. Regarding the capacitor, it is the vital component and its dimensioning is quite important. In detail, the PWM frequency and duty-cycle are limited by the requirement of refreshing the charge in the bootstrap capacitor.

As so, the size of the bootstrap capacitor must obey the following [53], [56]:

$$C_{BOOTmin} \geq \frac{Q_{TOT}}{\Delta V_{BS}} \quad (5.1)$$

$$Q_{TOT} = Q_G + Q_{LS} + (I_{LK\_GE} + I_{QBS} + I_{LK} + I_{LK\_DIODE} + I_{LK\_CAP} + I_{DS-}) \cdot t_{HON} \quad (5.2)$$

$$\Delta V_{BS} \leq V_{CC} - V_F - V_{LS} - V_{Min} \quad (5.3)$$

where  $Q_G$  is the MOSFET turn-on required gate charge;  $Q_{LS}$  is the charge required by the internal level shifters;  $I_{LK\_GE}$  is the MOSFET gate-source leakage current;  $I_{QBS}$  is the floating section quiescent current;  $I_{LK}$  is the floating section leakage current;  $I_{LK\_DIODE}$  is the bootstrap diode leakage current;  $I_{DS-}$  is the desat diode bias when on;  $I_{LK\_CAP}$  is the bootstrap capacitor leakage current;  $t_{HON}$  is the high-side MOSFET on time for the lowest PWM frequency;  $V_{CC}$  is the IC voltage supply;  $V_F$  is the bootstrap diode forward voltage;  $V_{LS}$  is the voltage drop across the low-side MOSFET or load; and  $V_{Min}$  is the minimum voltage between  $V_B$  and  $V_S$ .

Referring to the data sheets from the driver *LM5101BMA* and the n-channel MOSFET *IRFP4310ZPBF* (section 5.3.1), the following was obtained:

- $Q_G = 170nC$  (*IRFP4310ZPBF*)
- $I_{LK\_GE} = 100nA$  (*IRFP4310ZPBF*)
- $I_{QBS} = 200\mu A$  (*LM5101BMA*)
- $I_{LK} = 10\mu A$  (*LM5101BMA*)
- $I_{LK\_DIODE} = 100\mu A$  (typical)
- $I_{DS-} = 100\mu A$  (*LM5101BMA*)
- $Q_{LS} = 5nC$  (typical)
- $I_{LK\_CAP} = 0$  (negligible for ceramic capacitors)
- $t_{HON} = 100\mu s$  (10kHz)
- $V_{CC} = 12V$  (*LM5101BMA*)
- $V_F = 1V$  (*LM5101BMA*)
- $V_{LS} = 0.6V$  (*IRFP4310ZPBF*)
- $V_{Min} = 8V$  (*LM5101BMA*)

this results in:

$$C_{BOOTmin} \geq \frac{216 nC}{2.4} = 90nF \quad (5.4)$$

This value is the absolute minimum required, and due to the nature of the bootstrap circuit operation, a low value capacitor can lead to overcharging, which could in turn damage the IC. Therefore, to minimize this risk, the value obtained from equation (5.4) was multiplied by at least a factor of 10 (rule of thumb). This resulted in the following:

$$C_{BOOTfinal} = 1\mu F \quad (5.5)$$

The chosen capacitor was ceramic, because of its negligible leakage and low equivalent series resistance (ESR), with the value abovementioned. Also, according to [51] it is advisable to place another capacitor, as close as possible to the VDD of the IC, with a capacitance ten times larger. The aim is to filter eventual switching noise present in the IC ground plane. The final driver configuration can be seen in Figure 5.6.

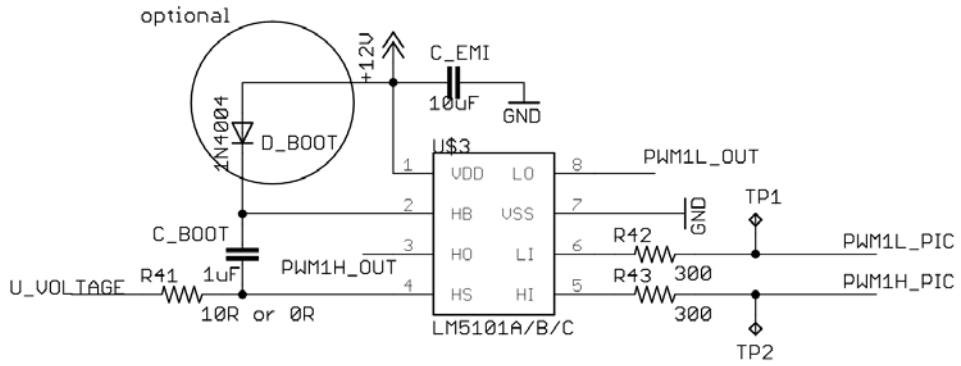


**Figure 5.6 - Schematic of the MOSFET gate driver circuit for pair PWM1**

### Managing voltage transients

When working with power switches such as MOSFETs, it is important to take into consideration the parasitic inductances present in the power circuit [53], [56] and [57]. In Figure 5.7 are depicted these unwanted inductances, labeled LS1,2 and LD1,2.

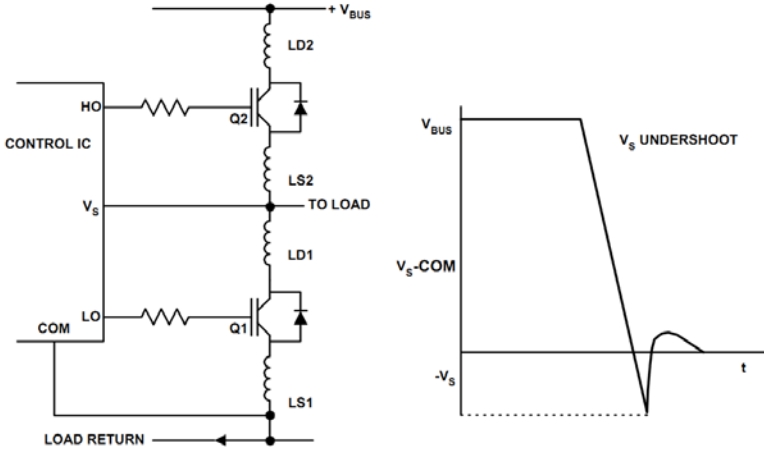


**Figure 5.7 - Parasitic inductances in half-bridge and the consequent VS pin undershoot**

There are also parasitic inductances in the gate drive circuit itself, but the highest current variations will occur in the mentioned power circuit, which will be the focus of this section. During switching, high variations in the half-bridge current induce voltage transients across all the shown parasitics. These transients induce noise in the circuitry, increase MOSFET dissipation and eventually might damage the IC.

Of all the problems caused by unwanted inductances, the one that demands more attention to IC operation is the tendency of the Vs node to undershoot ground. The high-side MOSFET turn-off causes the load current to suddenly flow in the low-side free-wheeling diode. However, the diode does not start to conduct immediately, as it possesses a turn-on time, which together with inductances LS1+LD1 lead to Vs undershoot below ground.

To address the Vs pin undershoot issue, there are many PCB layout guidelines [53], [56] and [57], being the most important recommendation to place the source of the high-side MOSFET as close as possible to the drain of the low-side MOSFET. To cope with this guideline, a new solder-free half-bridge construction method is presented in 5.3.4.1.

Also, to further improve Vs undershoot immunity two more methods can be employed [57]: placing a resistor between the Vs pin and the half-bridge center, to limit the current flow into the Vs pin during undershoot (method A); insertion of a resistor between IC GND pin and the power ground, to limit the current flow in the internal bootstrap diode (method B). In Figure 5.6 the resistor R41 realizes method A. Regarding method B, it was not implemented to avoid disruption of the IC ground reference.

### Ground Considerations

Since all the currents of the power circuit, including the ones caused by the parasitic inductances must return to the ground of the power module, the bootstrap portion of the IC driver must be referenced to power ground. However the MOSFET gate driver used has only one ground connection, which is common to the PWM control signals and bootstrap circuit. As so, to decrease switching noise coupling, the EM control board ground plane does not encompass the power module DC- bar. The two modules are separated from each other, sharing a low impedance common ground connection to minimize the potential difference between the two.

### Gate resistances

It is also important to fine tune the MOSFET turn-on and turn-off times, which have to be in accordance to the desired PWM frequency. In order to do so the topology shown in Figure 5.8 was implemented.

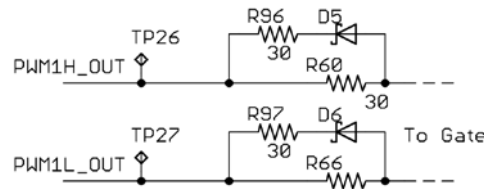


**Figure 5.8 - Schematic of the asymmetric gate resistor network circuit for pair PWM1**

The chosen value of the turn-on resistor (R66 and R60) was 30ohm. According to equation (5.6) [56], the turn-on time of the n-channel MOSFET used can be calculated, where  $R_{DRp}$  is the driver equivalent on-resistance;  $R_{Gon}$  is the turn-on resistor;  $Q_{gd}$  is the MOSFET gate-to-drain charge;  $Q_{gs}$  is the MOSFET gate-to-source charge; and  $V_{gs}^*$  is the gate-to-source plateau (Miller) voltage .

$$t_{on} = (R_{DRp} + R_{Gon}) \cdot \frac{Q_{gd} + Q_{gs}}{V_{cc} - V_{gs}^*} \quad (5.6)$$

Using the values taken from the respective datasheets and  $V_{cc} = 12V$ , was obtained:

$$t_{on} = (1.65 \Omega + 30 \Omega) \cdot \frac{29 nC + 35 nC}{12 V - 5 V} = 290ns \quad (5.7)$$

Taking into account that the minimum PWM period is 50μs, if the minimum duty cycle is considered to be 1%, this gives that the smallest pulse possible will have a 500ns duration. Hence, the turn-on resistor of 30ohm is suitable, since the turn-on time of the MOSFET will be 290ns. The value of the turn-off resistor was chosen to be the same, since the turn-on is the most critical situation to be addressed, being the turn-off duration much smaller.

### 5.2.2.2 DC Bus VOLTAGE FEEDBACK

In order to sense the DC bus voltage a simple voltage divider with a RC low-pass filter was implemented (Figure 5.9). Since the maximum bus voltage is 100V and the dsPIC® I/Os are limited to 5V, a voltage division of 20 was made using  $R84 = 200k\Omega$  and  $R86 = 10k\Omega$ . The electrolytic capacitor  $C41 = 10\mu F$  places the RC filter cutoff frequency ( $f_{-3dB}$ ) at 5Hz, to obtain stable measurements. The ceramic capacitor  $C40 = 100nF$  is used to cut the high frequencies.

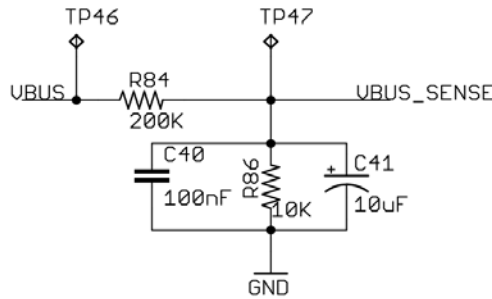


**Figure 5.9 - Schematic of the DC bus voltage feedback circuit**

### 5.2.2.3 DC BUS CURRENT FEEDBACK

To measure the DC bus current a low-side four wire shunt resistor was used, for its good accuracy at a low cost [58]. In detail, was implemented the low-side current measurement circuit shown in Figure 5.10 and a  $1.2m\Omega$  four wire shunt resistor was placed on the negative DC terminal.

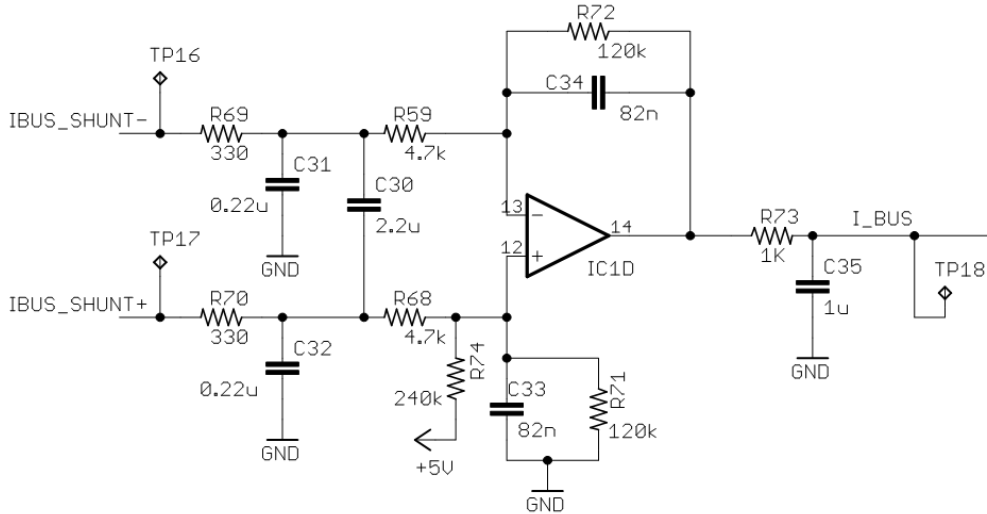


**Figure 5.10 - Schematic of the low-side DC bus current measurement circuit**

When the current flows through the shunt resistor, a voltage drop proportional to the amount of current flowing is created. Measuring the value of the voltage drop, and since the value of the shunt resistor is known, by Ohm's law the value of the current is obtained. However, the voltage drop is very small (dozens of millivolts), possesses EMI noise and also the switching noise is present.

The circuit shown is the combination of a differential amplifier with a high common-mode rejection ratio (CMRR), discrete RC filter and an offset adjustment circuit [58]. The first two amplify and filter the voltage readings. The offset circuit is essential to allow measurements of both positive and negative currents, *i.e.* positive and negative voltage drop readings, because the ADC readings are unipolar.

The RC combinations of  $R_{69}C_{31}$  and  $R_{70}C_{32}$  reduce the noise imposed on the two input lines, functioning as low-pass filters. Though, it is important that the resistors and capacitors are matched as close as possible. In fact, any difference in these networks will result in a degradation of the amplifier CMRR. Therefore, capacitor  $C_{30}$  is used as a RC differential filter that compensates for any mismatch in the previous RC networks, *i.e.* the differential filter formed by  $R_{69}C_{30}$  and  $R_{70}C_{30}$  will attenuate the differential signal at the amplifier caused by tolerance deviations of the common mode filers. Ultimately, the RC feedback networks  $R_{71}C_{33}$  and  $R_{72}C_{34}$  provide a low-pass filter response to the differential amplifier.

It is important to dimension the RC networks in a way that the cutoff frequency of each one is approximately the same, in order to have the maximum attenuation possible for frequencies above the desired  $f_{-3dB}$ . The theoretical gain,  $f_{-3dB}$  and offset voltage are given by:

$$|Gain| = \frac{R_{72}}{R_{69} + R_{59}} \quad (5.8)$$

$$f_{-3dB} = \frac{1}{2\pi \cdot R_{72} \cdot C_{34}} \quad (5.9)$$

$$offset = \frac{R_{71}}{R_{71} + R_{74}} \cdot Vcc \quad (5.10)$$

and replacing with the values from Figure 5.10 ( $Vcc = 5V$ ) comes  $Gain = 23.86$ ,  $f_{-3dB} = 16.17Hz$  and  $offset = 2.5V$ . This gain, with a  $1.2m\Omega$  four wire shunt and a  $2.5V$  offset, enables current readings from minus 87A to 87A, using a rail-to-rail operational amplifier (op-amp). Despite not allowing current measurements up to the established 100A, this range is already quite significant and does not notably reduce the application universe of the controller. Regarding op-amp choice, the elected was MCP6024 [59] by Microchip.

In Figure 5.11 is the bode plot of the SPICE simulation of the circuit, where it can be confirmed that  $f_{-3dB}$  goes in compliance with the calculated value. Also, one can state that three RC networks implemented permit an attenuation of -60dB/decade above 1kHz, -20dB/decade for each RC filter. If taken into consideration that the ADC readings will have 10 bits, a -60dB/decade attenuation above 1kHz signifies that frequencies above this value will only affect the least significant bit (LSB). Therefore, the noise present in the readings can be negligible.

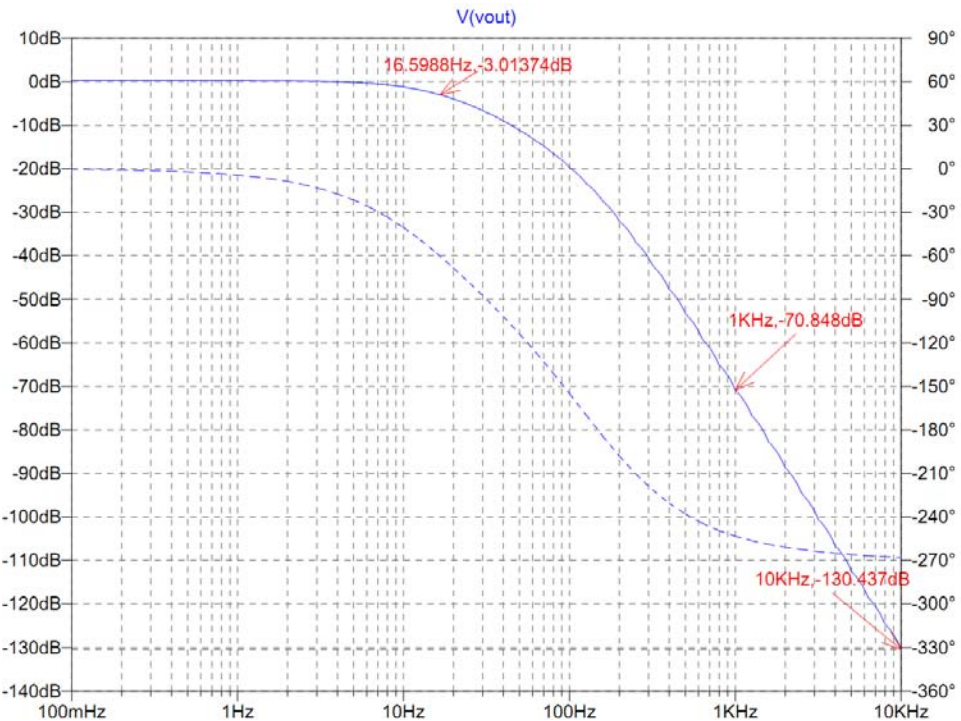


**Figure 5.11 - Bode plot of spice simulation pertaining to the low-side DC bus current measurement circuit (signal I\_BUS), where it can be verified that  $f_{-3dB} = 16.6Hz$  and 60dB/decade attenuation**

#### 5.2.2.4 OVERCURRENT SAFETY FUNCTION

To provide an overcurrent safety feature, the DC bus current filtered and amplified at the output of the circuit exhibited in Figure 5.10 ( $I_{BUS}$ ), is fed to the comparator shown in Figure 5.12. Here it is compared with the voltage given by  $\frac{R_{100}}{R_{99}+R_{100}} \cdot V_{CC}$  and if it exceeds this value, a FAULT [43] condition is detected and all PWMs are disabled.

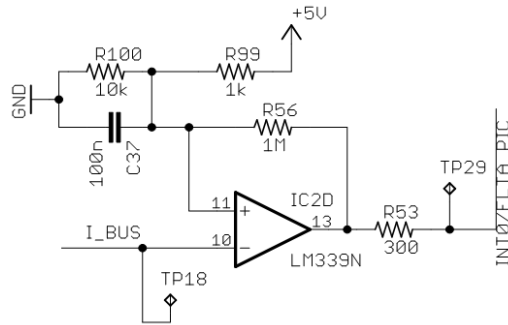


**Figure 5.12 - Schematic of the overcurrent detection circuit**

#### 5.2.2.5 BEMF VOLTAGE FEEDBACK

The BEMF voltage sensing is essential to implement the sensorless PPVS method of this thesis. As so, the circuitry aforementioned in Figure 3.12 was realized. It consists of a simple voltage divider, together with a RC filter and a comparator. This is show in Figure 5.13 for phase voltage U.

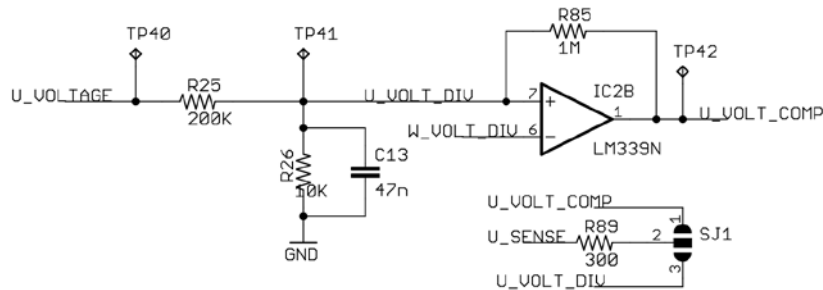


**Figure 5.13 - Schematic of the BEMF sensing circuit for phase U**

The voltage divider was dimensioned in the same way than for the DC bus voltage feedback. In relation to the RC filter, it was first necessary to establish the maximum BEMF frequency allowed. This is a direct result of the rotor rotation and EM pole pairs, which are both set in Table 5.1. Hence, using equation (3.3), the maximum established frequency of the electrical cycle is 660Hz. With the values used in Figure 5.13 it is obtained  $f_{-3dB} = 896Hz$ , allowing high frequency noise filtering. Though, at 660Hz the circuit introduces a phase-shift of  $-61.5^\circ$  on the BEMF signal. This results in the commutation signals of the PPVS method to be one step ahead of the ideal commutation sequence, causing a big slip and drastically reducing torque.

The reason behind this choice was due to the priority, at this stage of development of the hardware, to enable good Pseudo-Halls readings as early as possible in the open loop start process, to improve EM start. The values in section 4.2.4.4 show the improvement achieved for open loop start, since the BEMF filtering was effective enough to allow good Pseudo-Hall readings early than what theoretically anticipated. Furthermore, the maximum electrical cycle frequency registered during tests was 120Hz (see section 6.3.3), and for this frequency the phase-shift is  $-18.5^\circ$ , which is perfectly tolerable and does not greatly influences the EM performance.

After the BEMF voltage division and filtering, the signals are fed to the comparators in order to perform phase to phase voltage comparison. At the output are obtained the aforementioned Pseudo-Halls signals. However, it is also possible to directly feed the dsPIC® with the filtered BEMF voltage, using jumper SJ1.

#### 5.2.2.6 PHASE CURRENT FEEDBACK

To sense the phase current it was followed the same approach taken for the DC bus current sensing. A  $1\text{m}\Omega$  four wire shunt resistor was placed on the low-side of each half-bridge (Appendix C) and the voltage drop across it was filtered and amplified by a circuit identical to the one shown in Figure 5.10. The only difference between the phase current feedback circuit and the one from DC bus current feedback is the capacitors value. As a result, it presents the same gain and offset values, but with  $f_{-3dB} = 2.86\text{kHz}$ , being the attenuation also  $-60\text{dB/decade}$ .

It should be mentioned that the current measured is in fact the half-bridge current. Although, the actual phase voltage can be reconstructed in the dsPIC® with the signals retrieved from the BEMF voltage sensing circuit and this low-side current measuring circuit. That was taken into consideration when dimensioning the filters and is the reason why the cutoff frequency of this circuit is higher than the one of the BEMF sensing circuit. In fact, with a higher cutoff frequency, less phase delay is introduced in the half-bridge current readings. Though, the high frequency noise will also be less attenuated, so it had to be made a compromise between the two. All things considered, the phase current feedback circuit, with  $f_{-3dB} = 2.86\text{kHz}$ , exhibits a phase-shift of  $-15.7^\circ$  for BEMF signals at 660Hz, which represents a negligible impact on phase current reconstruction.

This solution is low cost and accurate, and proved to be a reliable alternative to direct phase current measurement, which requires an expensive high-voltage amplifier that can withstand a high common mode voltage.

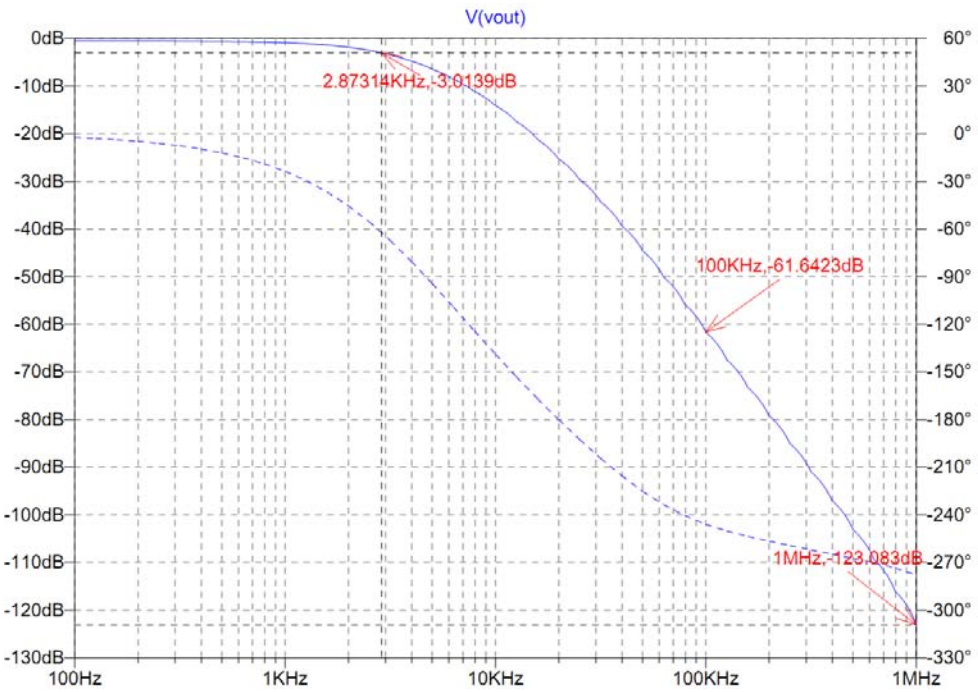


**Figure 5.14 - Bode plot of the spice simulation pertaining to the low-side phase current measurement circuit (signal I\_Phase\_U), where it can be verified that  $f_{-3dB} = 2.87\text{kHz}$  and 60dB/decade attenuation**

#### 5.2.2.7 HALL EFFECT AND GEAR-TOOTH SENSORS

The EM control board also includes a Hall effect and gear-tooth sensor interface to enable sensored control. The Hall effect sensor interface (Figure 5.15) is designed to accept sensors with voltage ratings higher than the dsPIC® I/O limit of 5V, through the voltage division made with resistors  $R_{22,44,48}$  and  $R_{20,45,47}$ . Additionally, a simple RC network is implemented with capacitors  $C_{15}$ ,  $C_{21}$  and  $C_{29}$  to filter signal noise. It was also included the pull-up resistors  $R_{23}$ ,  $R_{46}$  and  $R_{49}$  for enhanced compatibility with open-collector sensors. The jumpers SJ4, SJ5 and SJ7 enable changing between the sensorless BEMF voltage signals and the Hall effect sensors.

In regard to the gear-tooth sensor, was used the Allegro ATS642LSH [60], which from the circuit analyses point of view behaves like a current source. As so, when a tooth is detected the current flowing through  $R_{76}$  increases to a level that the voltage drop across it reaches the gate-to-source voltage threshold of the transistor, pulling-down the signal *GEARTOOTH\_SENSE* (Figure 5.16). As a result, the signal fed to the dsPIC® is a square wave with a frequency equal to the tooth sensing frequency. The value of  $R_{76} = 68\Omega$  was chosen taking into account that the sensor current when a tooth is detected is of 14mA, which by Ohm's law results in a voltage drop of 0.95V.

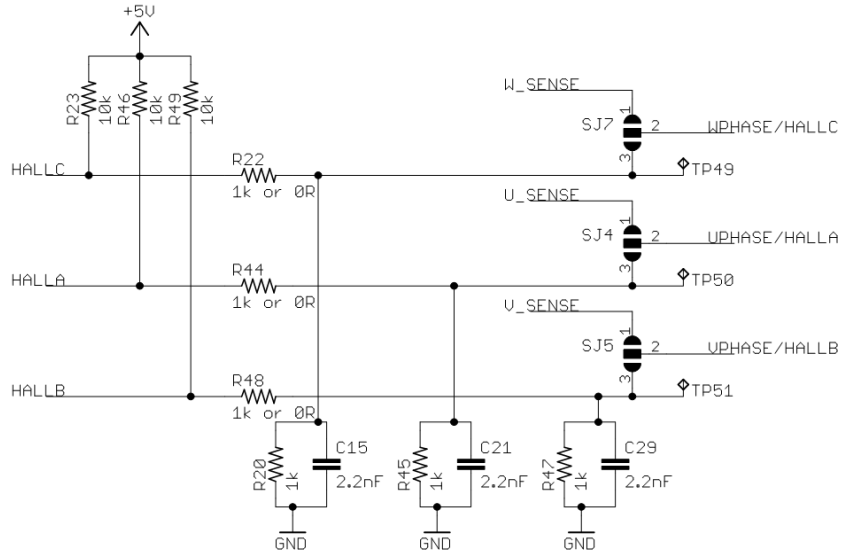


**Figure 5.15 - Schematic of the Hall effect sensor interface circuit**

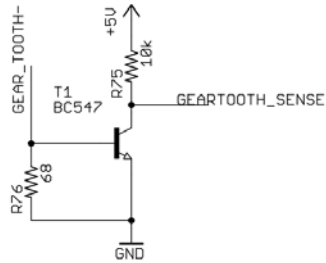


**Figure 5.16 - Schematic of the gear-tooth sensor interface circuit**

#### 5.2.2.8 VOLTAGE REFERENCES

The control module contains devices that require 12V and 5V voltage levels. The 12V can be obtained from a DC-DC converter in the power module that converts the DC bus 100V in 12V, which are directly fed to the MOSFET gate drivers and to voltage regulators. There are two voltage regulators, both performing a conversion from the 12V to 5V. One is dedicated to dsPIC® powering and the other powers the comparator and op-amp ICs. The reason for this is to isolate the digital noise introduced by the dsPIC® functioning from the rest of the analog components.

#### 5.2.2.9 CONTROL SWITCHES AND POTENTIOMETER

The EM control board contains a user-interface composed by a potentiometer and four control switches. Three of the switches are of general use and one is directly connected to the dsPIC® INT0/FLTA pin, which can generate an interrupt or disable all PWM firing, on a pin event.

### 5.3 POWER MODULE

Concerning the power module (Figure 5.17), this section describes the architecture followed and important construction details. Furthermore, this module concerns all the power electronics

responsible for power delivery to the EM phase windings. It is a three-phase bridge with an extra chopper circuit to enable control of a wound-rotor. To mention its solder-free construction method, which improves reliability, while decreasing parasitic inductances.

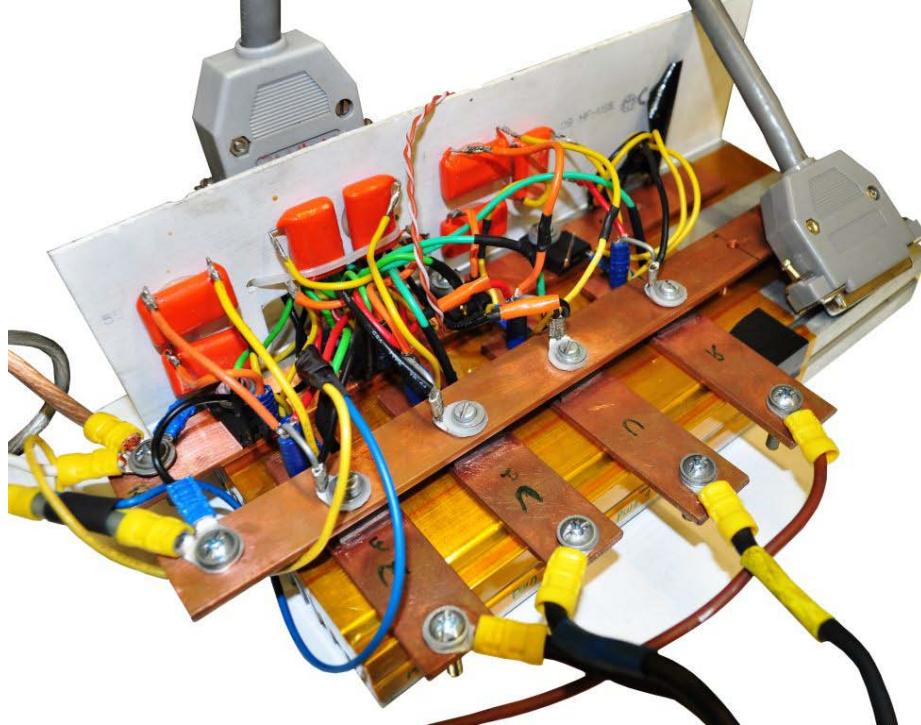


**Figure 5.17 - Developed solder-free three-phase power module with extra rotor terminal**

### 5.3.1 POWER SWITCHES

The power switches are a key component in any EM controller, since they are directly responsible for handling the power delivered to the EM windings, according to what is implemented in the control software. To determine the power switches to employ on this project, the application specifics are essential. In detail, the DC bus voltage, controller power and PWM switching frequency are the key factors to take into consideration [61].

According to this project maximum DC bus voltage (100V), PWM switching frequency (20kHz) and power (10kW), the MOSFET arose as the best solution [61]. In detail, the N-Channel MOSFET *IRFP4310ZPBF* by International Rectifier [62] was used. This MOSFET has a drain-to-source breakdown voltage of 100V and a continuous drain current of 120A, enabling the established requisites.

### 5.3.2 SOLDER-FREE CONSTRUCTION

The MOSFETs used contain a big conducting plane in the back which is the drain terminal. Taking advantage of this and following the typical three-phase bridge configuration show in Appendix C, the power module was structured has follows:

- the high-side MOSFETs have the drain connected to the DC+ bus, so the drain plane of each high-side MOSFET was directly screwed against a cooper bar that became the DC+ terminal;
- the low-side MOSFETs have the drain connected to the high-side MOSFET source and to the phase terminal. As so, for each phase, the low-side MOSFET drain plane was directly screwed against a cooper bar which became the phase terminal, and the high-side source and low-side drain pins were carved to each other (see section 5.3.4.1);
- to all the low-side MOSFETs source pins was carved a  $1\text{m}\Omega$  four wire shunt, for half-bridge current measurement, which was then screwed to a cooper bar that became the DC- bar;
- the DC- bus  $1.2\text{ m}\Omega$  four wire shunt resistor was directly screwed to the DC- bar and the shunt other end became the DC- terminal.

In Figure 5.18 is shown a schematic representation of this solder-free three-phase bridge architecture.

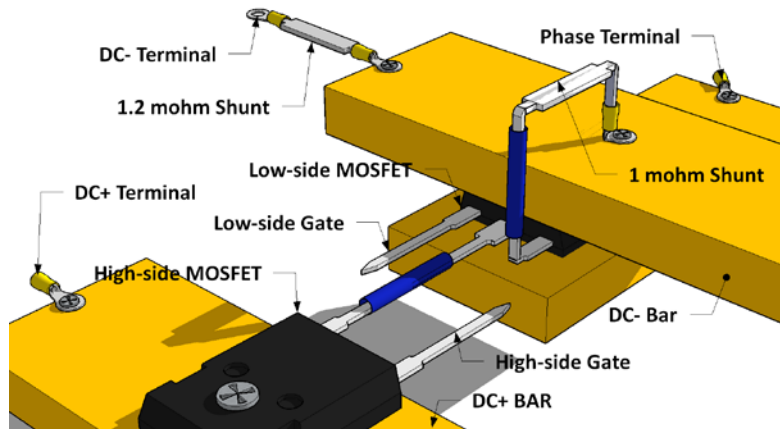


**Figure 5.18 - Schematic representation of the developed solder-free three-phase bridge**

### 5.3.3 POWER DISSIPATION

As abovementioned, all the MOSFETs are directly screwed to a cooper bar, that works both as a terminal for power and EM connections, and also as a power dissipation device. To further increase power dissipation, the cooper bars are also screwed to an electrically isolated aluminum heat sink. This hybrid solution, allows a rapid and good power dissipation by the cooper bars, which is further and more slowly dissipated in the aluminum. Also, the cooper bars are an excellent terminal for their great electric conductive characteristics. Overall the system attains a very good performance at a low price.

### 5.3.4 TRANSIENTS AND NOISE SUPPRESSION FEATURES

Important measures were taken in the power module design to reduce the problematic of voltage transients that might affect the stability and performance of the MOSFET drive circuitry. Also, the noise produced by the power switches was taken into account, with proper ground layout considerations.

#### 5.3.4.1 SOLDER-FREE HALF-BRIDGE

As mentioned in section 5.2.2.1, the urging issue in voltage transients is the tendency of the Vs node to undershoot ground. Above all causes prevails the parasitic inductances LS2 and LD1 (Figure 5.7), which effectively isolate the Vs node from the clamping action of the low-side freewheeling diode.

The most effective way of dealing with this Vs node undershoot, is to place the source of the high-side MOSFET very close to the drain of the low-side one [53]. Hence, the half-bridge was built as shown in Figure 5.19, with the source pin of the high-side MOSFET directly carved to the drain pin of the low-side MOSFET. This technique allows a solder-free connection between the two, which improves system reliability with thermal variances, and drastically reduces the parasitic inductances LS2 and LD1 that cause Vs node undershoot.

Also, as mentioned in 5.3.2, the high-side MOSFET drain is directly screwed to the DC+ bar, which radically decreases the parasitic inductance LD2, and further improves voltage spikes suppression. The inductance LS1 is not directly addressed with the proposed solder-free topology, since a  $1\text{m}\Omega$  four wire shunt is used between the source of the low-side MOSFET and the DC- bar. However, decoupling capacitors (section 5.3.4.2) are used to overcome this issue.

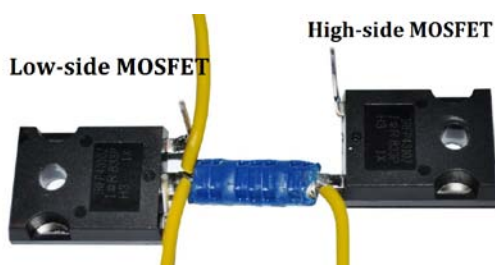


Figure 5.19 - Developed solder-free half-bridge

#### 5.3.4.2 BYPASS CAPACITORS

In order to eliminate the effects of the inductance of the wiring between the power supply and the three-phase bridge, electrolytic capacitors were connected between the DC+ and DC- bars, as can be seen on Appendix C. This, by itself, virtually eliminates the parasitic inductances LD2 and LS1. Furthermore, these capacitors also aid in the suppression of the DC supply transients. It was used two 100V,  $1000\mu\text{F}$  electrolytic capacitors.

Alongside, between the drain and source of each MOSFET was connected a ceramic capacitor to further improve the suppression of voltage transients that occur due to switching of the MOSFETs. In order to determine the capacitance of this component, it is necessary to take into consideration that a small capacitance will have little effect on suppressing voltage transients, while a higher capacitance will better absorb the transients but will also affect the rise and fall times of the current across the MOSFET. Therefore, a compromise has to be made and the value of the capacitance used on this dissertation was 1uF. This value was established based on what is used amongst market available solutions.

## 5.4 SUMMARY

This chapter presented the control and power modules built for EM control. Pertaining to the control module, dedicated MOSFET gate drivers were used to ensure a proper switching at the established frequencies. The module was built to allow sensored and sensorless control, encompassing feedback circuitry and Hall sensors interface. Furthermore, the system enables the implementation of BEMF sensing techniques and vector control methods, since both phase current and voltage are sensed. Power consumption can also be sensed through DC bus sensing circuitry. The microcontroller used was a dsPIC30f4011.

In relation to the power module, it employs a solder-free construction method, which improves transient voltage immunity, while also increasing the module thermal and mechanical reliability.



# CHAPTER 6

## TESTS AND RESULTS

---

In order to assess the practical performance of the developed hardware and software, and infer potential of applicability on an airplane, a series of tests were undertaken to determine the speed, power and torque ratings. This chapter depicts and discusses the retrieved data, presenting an analysis of the prototype performance, with special focus on the PPVS control method. To mention that all the data was collected solely recurring to the features available in the hardware built.

### 6.1 TESTING STRUCTURE ASSEMBLY

A testing structure was built according to what was presented in section 2.5.3. The final result can be seen in Figure 6.1.

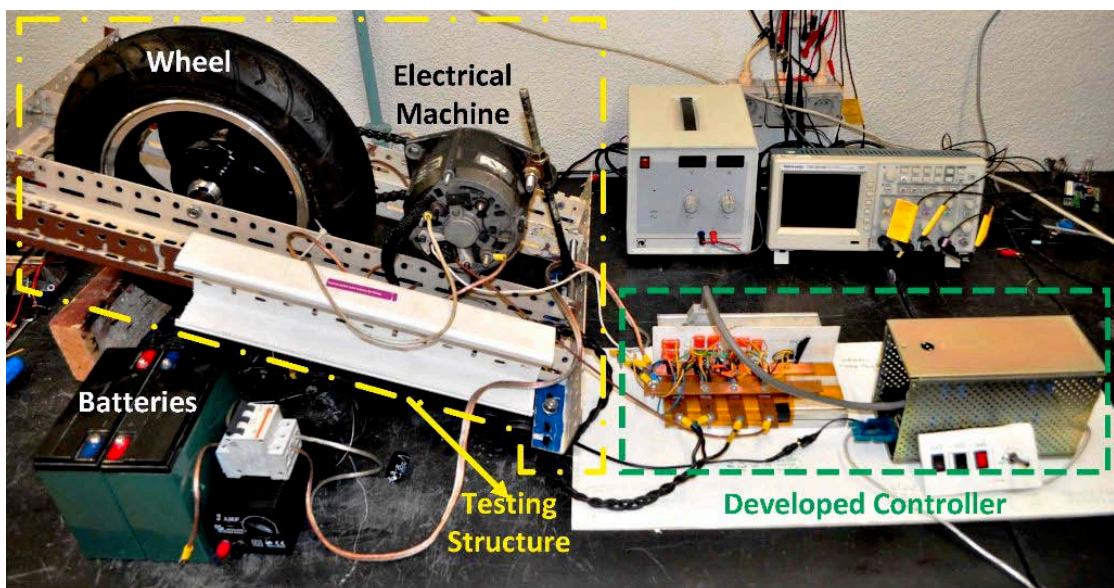


Figure 6.1 - Testing structure built for this dissertation

As mentioned in 2.5.2, the EM used was a truck alternator, in detail a 28V, 80A Bosch alternator. Despite being rated for 28V operation, it can withstand up to the double of the rated voltage while in motor mode. Though, all the tests were performed either at 12VDC or at 24VDC, using one/two 12V 36Ah lead acid batteries. This was decided in order to preserve the integrity of the system by limiting the input power at this testing stage. At the same time, this range of supply voltages already allows an accurate assessment of the system performance.

In relation to the transmission between the alternator and the wheel, a chain was used. The gear ratio between the two was 5.3 due to an 8 teeth gear in the alternator and a 42 teeth gear in the wheel.

## 6.2 CONTROL METHOD VALIDATION

The first test to be performed was concerned to the validation of the PPVS control method employed on this dissertation, in specific, assess the accordance of the Pseudo-Halls signals at the comparators outputs with actual Hall effect sensors outputs. Therefore, a BLDC electrical machine, with Hall effect sensors already placed in the stator, was controlled using the developed hardware and software. The BLDC was controlled in sensorless mode and the signals from the Hall sensors were compared, in the oscilloscope, with the Pseudo-Halls signals retrieved from the control module BEMF voltage feedback circuitry. The result can be seen in Figure 6.2.

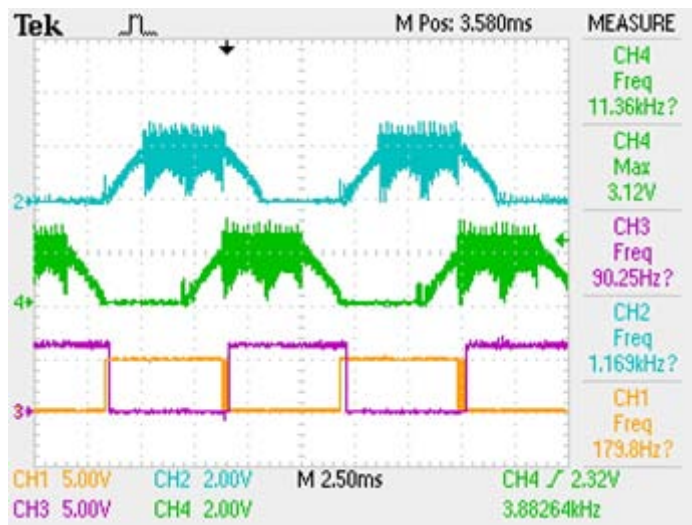


**Figure 6.2 - Comparison between the pseudo-Hall signal *U\_VOLT\_COMP* (CH1) and the correspondent Hall sensor Signal (CH3); CH2 and CH4 are BEMF voltages of phases U and W respectively (Appendix C)**

It is possible to verify that the Pseudo-Hall signal (CH1) is  $180^\circ$  out of phase in relation to the Hall sensor signal (CH3). This is due to the fact that the two BEMF signals (CH2 and CH4) that

are compared to generate the Pseudo-Hall signal, are switched at the comparator input, which can be easily compensated in the software.

This result proves the concept discussed in section 3.5, showing that it is possible to replace Hall effect sensors by a phase to phase voltage sensing method. To mention that the noise of the PWM superimposed on the BEMF signal cannot be totally suppressed by the low-pass filters, which results in the CH1 transitions not to be exactly 180degrees out of phase in relation to CH3. As a result, there is a slightly earlier commutation, when compared to a control method that employs Hall sensors. This introduces an amount of slip that, at this testing stage, can be considered as negligible without a great loss of accuracy.

## 6.3 PROTOTYPE PERFORMANCE

The following sections exhibit and discuss the tests performed on the prototype to assess the practical performance of the developed software and hardware. All the data was retrieved utilizing the voltage and current feedback circuitry present in the hardware built. Moreover, the tests were performed on the testing structure itself according to the following:

- for tests performed with no load, the wheel was in free rotation in the air, without any other external interference;
- to achieve load, force was applied on the wheel in order to simulate the scenario in which the testing structure would tow a vehicle connected to it.

In this stage of development and testing of the technology, no tests were conducted under real world conditions, *i.e.* with the testing structure towing a vehicle. The reason behind this decision was to enable a first contact with the behavior and performance of the system, in a controllable environment, to early detect any system failure that could compromise its integrity.

### 6.3.1 OPEN LOOP START

As mentioned in section 4.1, the developed sensorless control method comprises three stages, which are the alignment, open loop start and sensorless run. These are depicted, in terms of power consumption, in Figure 6.3.

The alignment stage duration is defined by the variable *STABILITY\_DELAY*, which for this test was set in order to enable an alignment period of one second. In relation to the power consumption, the high values verified for both 12V and 24V operations are in accordance to what was mentioned in section 4.1.1: at standstill the current in the stator windings is only limited by the winding impedance, which is virtually equivalent to a short circuit.

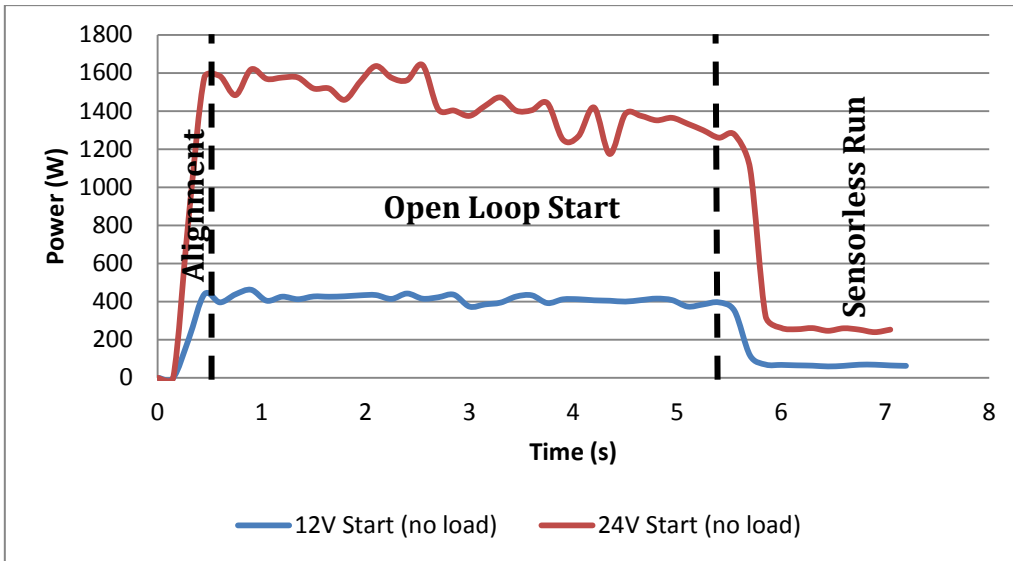


**Figure 6.3 - Power consumption profile during start from standstill (no load), showing the three stages of the control software: alignment, open loop start and sensorless run**

Concerning the open loop start stage, the rotational speed gradually increases until enough BEMF is generated to start the sensorless run. However, during the open loop ramp the commutation period is digitally determined without any knowledge of the rotor position, which leads to the appearance of slip and a high power consumption. This fact is amply verified in Figure 6.3. Though, as soon as enough BEMF is generated to allow the sensorless run, the commutation starts to be determined by the Pseudo-Halls readings, drastically reducing slip and power consumption. Altogether, between the alignment and sensorless run, the open loop start procedure takes a total of 5.5 seconds.

It is also possible to verify that the power consumption while at 24V operation is four times higher than at 12V. According to Ohm's law, at 24V operation the current drawn will double, since the impedance of the windings is a constant. Therefore, the power consumption is expected to quadruple since  $P = I^2 \cdot R$ .

### 6.3.2 SPEED CONTROL

The control method implemented by the software does not include any type of feedback control, *i.e.* the potentiometer set by the user directly determines the stator PWM duty cycle, which in turn controls the power delivered to the stator windings. According to what was mentioned in section 4.2.5, the speed of an EM is directly proportional to the power supplied to the windings, from this results that the user has a direct control over the rotational speed of the EM. Therefore, the speed of the EM is only dependent on the current user request, without any knowledge of the previous state of the system.

However, it is important to state that non-feedback speed control can only be accomplished when on sensorless run mode, since in order to control the EM speed from the stator PWM duty cycle it is first necessary to determine the rotor position. If such control was performed without the knowledge of the rotor position, the synchronism would be lost and the rotor would enter a locked state. Therefore, in order to validate the sensorless run mode, in particular rotor position determination based on the PPVS method, the rotor speed variation in response to a sudden change in the potentiometer was measured. The results are shown in Figure 6.4 and Figure 6.5 and were obtained for a rotor PWM duty cycle of 100%, under no load conditions.

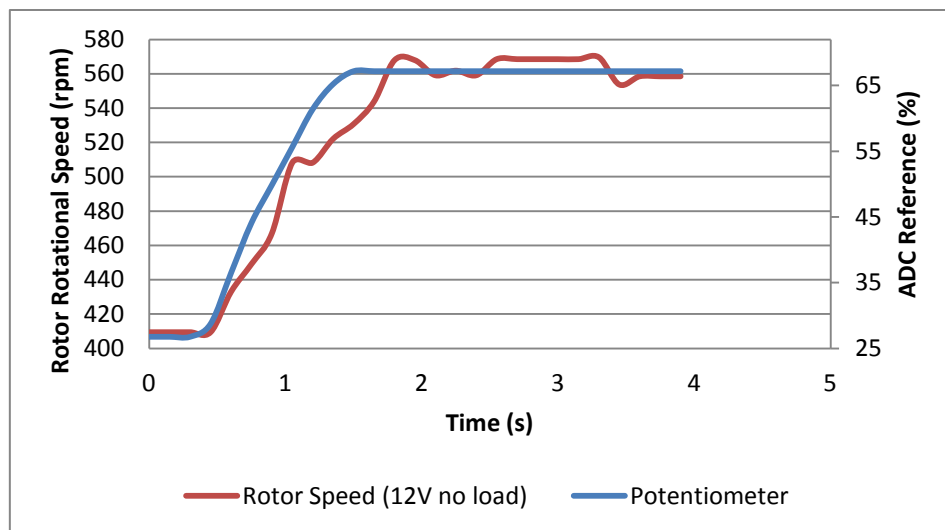


**Figure 6.4 - Rotor rotational speed response to a step in the reference (potentiometer), for 12V operation and no load**

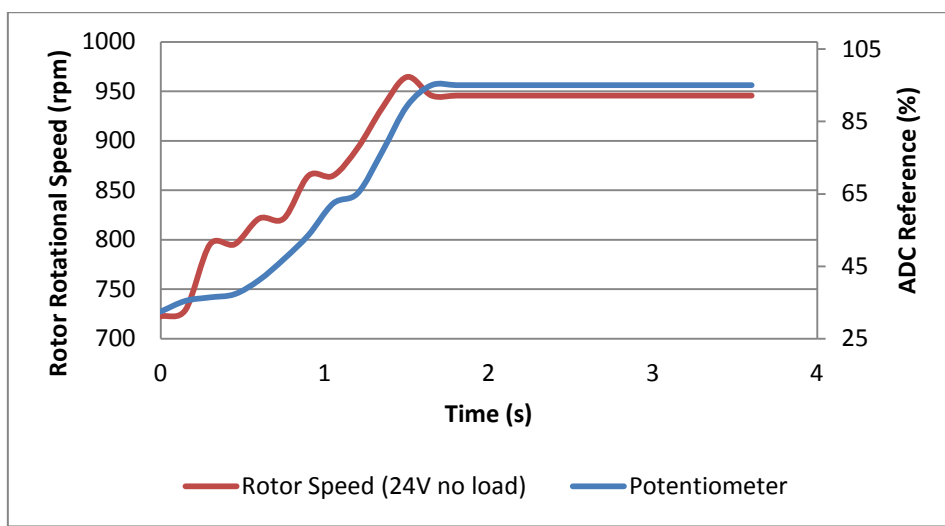


**Figure 6.5 - Rotor rotational speed response to a step in the reference (potentiometer), for 24V operation and no load**

As it can be seen in Figure 6.4 and Figure 6.5, the rotor rotational speed follows accordingly the user request, represented by the blue line (potentiometer). However, it is visible that for 24V

operation the time response is better than at 12V operation. In both cases the system is subjected to a one second variation in the reference - from 0.5 to 1.5 seconds the reference rises from the initial to the final value. At 24V it is shown that the rotor varies from the initial to the final speed also in 1 second. However, at 12V the rotor takes 1.5 seconds to attain the requested speed. This can be explained by the fact that at 24V the EM torque is greater than at 12V, which allows for a faster acceleration (see results of section 6.3.4).

Alongside, since the power delivered to the EM at 24V is four times higher, the rotor speeds are quite superior to those verified at 12V. As a reference, using the gear relation of 5.3 between the rotor and wheel, and considering an external perimeter of the wheel of 1.5m, it is obtained that for 950 rpm in the rotor (Figure 6.5) the wheel is rotating at 16km/h. Despite being conservative, this gear relation was chosen to allow a safe testing environment and also to simulate the taxiing speeds of an airplane.

The previous tests were performed without any load upon the system, in order to validate the PPVS method implemented in the software. Though, to further assess the performance of the sensorless control method, the system was placed under a constant load and the potentiometer was varied extensively within its range, to verify if the speed varied accordingly. The result can be seen in Figure 6.6 and was also obtained with a rotor PWM duty cycle of 100%.

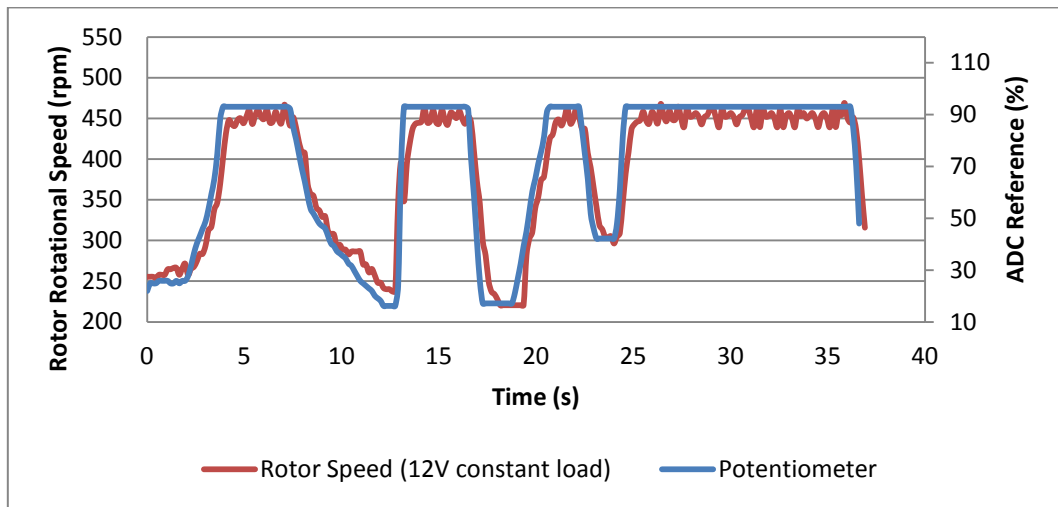


**Figure 6.6 - Rotor rotational speed response to a sequence of variations in the reference (potentiometer) under constant load, for 12v operation**

Although the test was performed at 12V, which results in a lower torque available, the results show that the rotor rotational speed quite accurately follows the user request variations. Still, it is verified that for the same user request the rotor rotational speeds are inferior to the ones verified in no load conditions (Figure 6.4). This is due to the non-feedback controller used, since in order to attain the same speed under load it would be necessary to increase the power delivery, in form of user request, relatively to the situation when the system was not subjected

to any load. In other words, a closed-loop controller would be necessary, so that rotor rotational speed would be the same for an unchanged user request, even when under different load scenarios.

Altogether, the rotor rotational speed response tests show that the PPVS control method implemented in the software, with direct stator PWM duty cycle control by the user potentiometer, enables a good EM control without employing any type of sensors. Nevertheless, the speeds achieved with sensored EM control would have been slightly higher. This is explained by the small phase delay that exists between the Pseudo-Hall signals and ideal commutation points, mentioned in sections 3.5.4 and 6.2.

### 6.3.3 FIELD WEAKENING

The EM used was a synchronous machine with a wound-rotor, which enables controlling the rotor magnetic field intensity by varying the rotor PWM duty cycle. This process is most commonly referred to as field weakening [41] and allows for an EM to rotate faster than its rated speed. In order to do so, the rotor magnetic field intensity is decreased, at a cost of also reducing the EM torque. In Figure 6.7 is shown the rotor rotational speed to 100%, 50% and 25% of rotor PWM duty cycle.

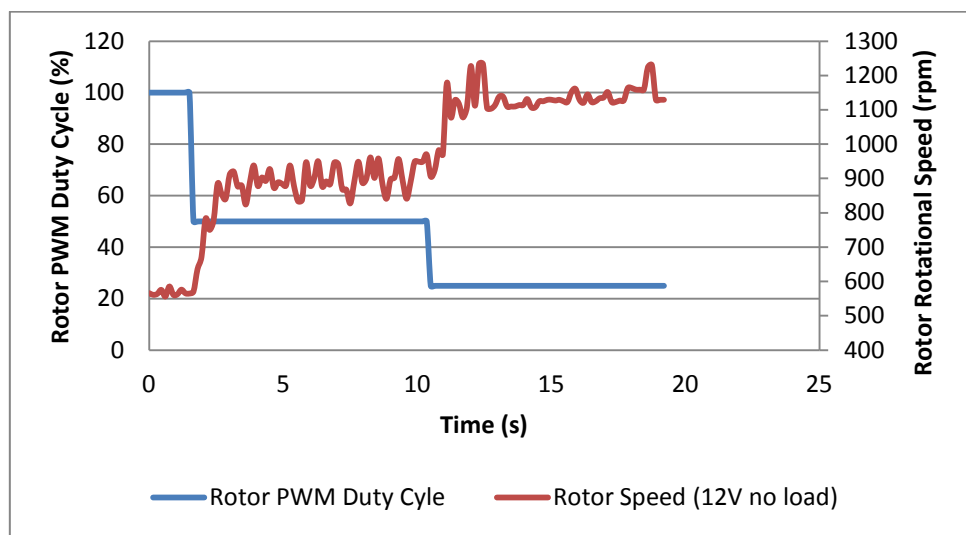


**Figure 6.7 - Rotor rotational speed variation for different rotor magnetic field intensities (field weakening), for 12V operation and no load**

As expected, the rotor rotational speed increases accordingly with the decrease in rotor PWM duty cycle. The test was performed at 12V supply voltage, under no load and with the stator PWM duty cycle steady at 75%, to which corresponds a rotor speed of 560 rpm for a rotor PWM duty cycle of 100%, which can also be verified in Figure 6.7. However, by decreasing the rotor PWM duty cycle to 25%, were achieved rotor speeds of 1200 rpm. This represents a wheel speed of 20km/h.

#### 6.3.4 POWER AND TORQUE

The graphics of Figure 6.8 and Figure 6.9 exhibit the power consumption and torque measurements performed both for 12V and 24V supply voltage under heavy load conditions. In order to obtain these results the system was configured to achieve its maximum performance, since the primary concern was to assess the system behavior under extreme conditions. Therefore, both tests were conducted with the maximum rotor magnetic field intensity (rotor PWM duty cycle at 100%) and the highest power supply possible (stator PWM duty cycle at 100%). It is important to mention that the power and torque data refers to power consumption and not to power and torque output, since the laboratory did not possess tools that enabled power and torque output measurements. The values referent to power were obtained by multiplying the DC bus current with the DC bus voltage, and the torque values were obtained by dividing the power values with the correspondent rotor speed values.

Before getting into more detail about the results, it is important to refer that due to the sensorless control method implemented on this thesis, torque at zero speed could not be measured efficiently. The reason for this is that the open loop start procedure does not allow torque control before the sensorless run stage, as the rotor position cannot yet be determined. If the system is subjected to considerable load variations during the starting procedure, synchronization can be lost and the rotor might get locked. This determines that the system can only be putted under heavy load conditions while in sensorless run, therefore at speeds greater than zero.

Concerning the results, it is shown a typical electrical machine power consumption behavior: when the system is subjected to a load, if the power consumption would stay constant, the speed would decrease; however, in order to try to maintain the speed, since the reference keeps unchanged, the power consumption increases to react against the load action. Therefore, the power consumption data exhibits a linear behavior that can be confirmed by the linear fit curves of Figure 6.8 and Figure 6.9. As expected, the maximum power value is reached at the lowest rotor angular speed. The torque follows the same tendency, with the highest torque to be achieved at low speeds and linearly decreasing with speed.

It is also revealed, for 24V operation, that the rated power of the alternator of 2kW was fully extracted from the supply batteries, to which corresponded 31N.m of torque. Alongside, for 12V operation, since the power available is four times lower, it was verified a 500W peak power consumption, with 12N.m of torque. In addition, the rotational speed of the rotor at 24V also reflects a higher power supply, since the speed achieved under extreme load conditions was of 600 rpm, while at 12V it was only 350 rpm.

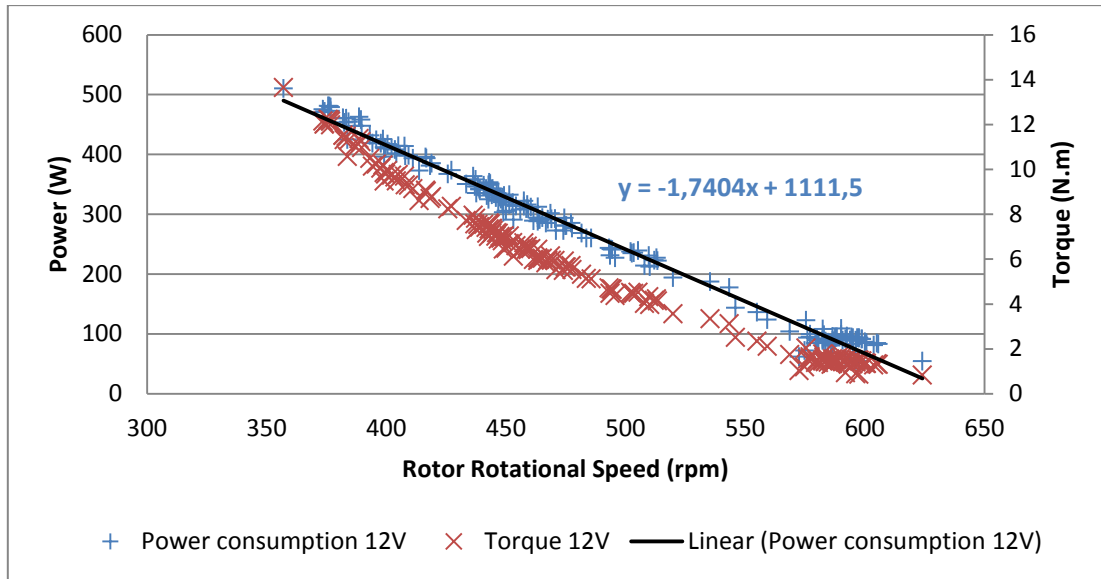


**Figure 6.8 - Power and torque measurements for 12V operation with load**

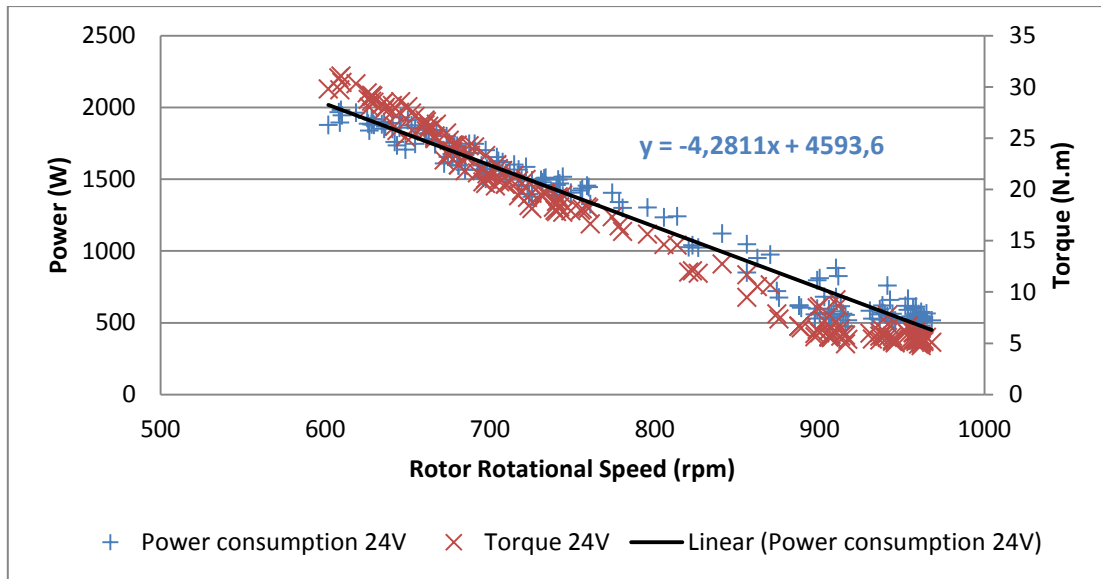


**Figure 6.9 - Power and torque measurements for 24V operation with load**

On the whole, the results of rotor speed control together with the power and torque data, not only validate the PPVS control method implemented, while also demonstrate that without using any sensors for rotor position determination, the EM achieves a good performance and controllability.

The slip introduced by the phase delay between the Pseudo-Hall signals and actual Hall sensors, slightly reduces speed and increases power consumption. Although, the results show that the PPVS control extracts nearly all the potential of the alternator used. Therefore, this phase delay

can be negligible at this stage of development since the lack of performance it introduces is quite small.

This kind of technology might be very attractive for the proposed concept of airplane taxiing, since a good EM control is achieved without the intervention of any sensors. Moreover, sensors present a high risk of malfunction in the adverse environmental conditions that the system would have to withstand. The only issue that needs to be further addressed is the open loop starting procedure.

## 6.4 SUMMARY

This chapter presented all the tests results that were undertaken to assess the performance of the hardware and software created for this dissertation. First it was validated the Pseudo-Halls creation method, by comparing the comparators output with actual Hall effect sensor readings. It was then validated the speed control method implemented, by measuring the rotor rotational speed response to variations in the reference signal. The power consumption and torque ratings were also measured to trace the system behavior in heavy load conditions.

All the results were very encouraging and demonstrated that the power electronics built, employing a sensorless control method, enables an EM performance that rivalries with what would be obtained by sensored control methods.

# CHAPTER 7

## CONCLUSIONS

---

A steep air traffic growth in forthcoming decades is forcing the aeronautical industry to react with a strong quest for efficiency. The MEA, POA and CleanSky initiatives are the face of such mission, establishing the guidelines for cleaner and more efficient airplane operation. One area where it is unavoidable actuate is airplane taxiing and decade pending issues need to be addressed, in order to bring taxiing to an all new era.

The work developed throughout this dissertation aimed at developing and testing new technologies capable of being applied on a new electric taxiing approach. In detail, it was designed and constructed a low cost, reliable and sensorless power electronics for synchronous wound-rotor EM control.

The first step taken was the development of a sensorless control methodology, employing phase to phase voltage sensing (PPVS). This technique enabled the creation of Pseudo-Hall signals and the results show their capability to simulate the behavior of actual Hall effect sensors signals with great accuracy. Therefore, it was possible to create a control method with the best performance/complexity ratio amongst all the methods presented on CHAPTER 3.

In relation to the control and power modules, it was designed and constructed a development platform that allows the implementation and study of several control methods on a wide range of EMs. Though, the system was optimized for synchronous wound-rotor EM control and the PPVS control method was implemented. All the power electronics was then mounted on a testing structure containing an alternator, and several tests were carried out in laboratory conditions to assess the performance of the power electronics and EM used.

On CHAPTER 6 are presented the results obtained with tests performed upon the system. It was first validated the PPVS control method, by comparing the Pseudo-Hall signals with real Hall

sensor signals. Though, the main focus of the tests was the evaluation of the power electronics, together with the open loop start and sensorless run of the PPVS method. Referring to the open loop start, despite being a critical stage on the control process, it was successfully implemented and the results show the expected behavior. In relation to the sensorless run, being this the keystone of this dissertation, the results obtained were very promising. The main achievements can be folded as:

- the rotor rotational speed accompanies the user request variations, even under load conditions. This demonstrates the direct speed control implemented on the software, where the user has a direct control over the stator PWM duty cycle, which in turn determines the rotational speed of the rotor;
- the rotor magnetic field weakening, which is a feature enabled by wound-rotor EMs that allows an extent of the maximum speed of the rotor, was also implemented and successfully verified;
- power consumption and torque results under heavy load conditions were also taken, which were only possible with proper rotor position determination, achieved by the PPVS method. The curves obtained are consistent with typical EM power and torque curves. Furthermore, a total of 2kW peak was extracted from the supply batteries.

These results amply verify the control of an EM, which was only possible with perfect functioning of both the power electronics and control method.

Concerning applicability on an airplane, it is possible to conclude that synchronous wound-rotor EMs provide a reliable and respectable performance as a motor, while achieving the regeneration results exhibited in [19]. Moreover, a sensorless control technique, with all the advantages it brings in terms of reliability, which is important in an operating environment such as the MLG, proves to be a good alternative to sensored control methods. In fact, bearing in mind the load variations during airplane taxiing, the developed sensorless technique is capable of replacing more expensive sensored methods, as it attains promising results. The only problem subsists on the open loop start procedures, which need further addressing to allow full sensored control replacement.

As a final remark, it should be stated that actual state of development of the PPVS technique appears as a viable solution to electric airplane taxiing. Although not attaining the same degree of controllability of sensored systems, what could represent a barrier to a full scale implementation on electric taxiing, a PPVS technique can quiet well function as a redundant system or alongside a sensored control method.

## 7.1 FUTURE WORK

To further improve the performance of the PPVS control method, it should be considered the implementation of:

- digital compensation of the phase delay existent between the Pseudo-Hall signals and real Hall sensor signals;
- techniques such as phase advance [36], which allow the extension of the speed range of the EM;
- introduction of a single Hall effect sensor in the shaft to determine the rotational speed of the rotor, which can prove to be a viable solution to address the EM slip that occurs during the open loop start, causing the high current consumption;
- closed-loop controller to perform speed and torque control with correspondent feedback.

Moreover, the testing structure, power electronics and EM should be subjected to testing under real conditions, outside the laboratory, to thoroughly evaluate the performance of the system and more accurately infer applicability on an airplane. Ultimately, a 1:1 scale size of the system should be constructed and implemented on a testing airplane.

# Appendix A

## MAIN CODE PARAMETERS

---

### A.1 FILES LISTING

Filename	File purpose	Functions contained
<b>defines.h</b>	#define major parameters used throughout the code	
<b>globals.h</b>	External declaration of global variables used throughout the code	
<b>source.h</b>	Linkage of all the separate files - contains all the functions headings – and #include of libraries used	
<b>adc.c</b>	Configuration of ADC module	open_adc
<b>change_notification.c</b>	Configuration of CN module	open_CN
<b>config_rotor_PWM.c</b>	Configuration of rotor PWM (OC4)	config_rotor_PWM
<b>configIO.c</b>	Configuration of dsPIC® IO pins	configIO
<b>globals.c</b>	Linkage for the external global variables	
<b>input_capture.c</b>	Configuration of IC module	open_IC1; open_IC7; open_IC8
<b>MCPWM.c</b>	Configuration of MCPWM module	InitMCPWM
<b>serial_port.c</b>	Configuration of UART module	SerialOpen; SerialWrite; print_int; print_long; print_string; Serial_print; SerialInstruction_transmited; SerialInstruction_received; U2TXInterrupt; U2RXInterrupt
<b>thesis_sensorless_PPVS.c</b>	Initialization, control algorithm, interrupts and background code (main file)	Main; START_Motor; STOP_Motor; INT_STATUS; ADCInterrupt; CNInterrupt; T2Interrupt; T1Interrupt; Open2Lock_transition; System_routines; IC1Interrupt; IC7Interrupt; IC8Interrupt;

		Send_SerialData; braking
timer.c	Configuration of TIMER module	open_timer1; open_timer2_for_rotorPWM; open_timer3

Table A.1 - Source code files, purpose and specific functions contained

## A.2 PARAMETERS LISTING

	Purpose
<b>Machine Parameters</b>	
<b>TOOTH_NUMBER</b>	Tooth number of the EM external disk. Associated to the utilization of a Hall effect sensor for rotor rotational speed calculation
<b>POLE_PAIRS</b>	Number of EM pole pairs, essential to the conversion of electrical cycles in mechanical revolutions
<b>Frequency Parameters</b>	
<b>FCY</b>	Instruction clock rate [44], corresponds to the actual speed of code execution in the dsPIC® and must be in accordance with user-defined PLL and FOSC [44]. Essential to all TIMERS and functions associated with them.
<b>FPWM</b>	Frequency of Motor Control PWM (MCPWM) module. Actual frequency will depend in MCPWM configurations [43]
<b>FPWM_ROTOR</b>	Frequency of rotor PWM. This parameter is, in fact, timer 2 period, which is the timer associated to Output Compare 4
<b>TIMER1_PERIOD</b>	Timer 1 period, which is the timer used for the open loop routine
<b>TIMER3_PERIOD</b>	Timer 3 period, which is the timer used for the Input Capture module
<b>REALTIME_UPDT</b>	Frequency of the Real-time update routines
<b>ADC Parameters</b>	
<b>IBAT_FACTOR</b>	Translation of the ADC value corresponding to DC bus current to Ampere. Calibration needed, since it depends on ADC configuration [43] and hardware used for sensing (section 4.2.5.4)
<b>IBAT_OFFSET</b>	
<b>VBAT_FACTOR</b>	Translation of the ADC value corresponding to DC bus voltage to Volt. Calibration needed, since it depends on ADC configuration [43] and hardware used for sensing (section 4.2.5.4)
<b>VBAT_OFFSET</b>	
<b>POT_THRESHOLD</b>	ADC value above which potentiometer readings are considered positive. Depends on ADC configuration [43]. Filters minor reading fluctuations on the pin associated to the potentiometer to avoid false starts.
<b>CURRENT_THRESHOLD</b>	Maximum DC bus current allowed in the system, commutation stops above this value. In Ampere , with 2 decimals
<b>DUTYC_MIN</b>	Minimum duty cycle value allowed to avoid PWM distortion due to dead time utilization

<b>Purpose</b>	
<b>DUTYC_MAX</b>	Maximum duty cycle value allowed to avoid PWM distortion due to dead time utilization
<b>UART Parameters</b>	
<b>BAUD_RATE</b>	Baud rate value used for UART [43] configuration
<b>SEND_DATA_T2MS</b>	Period of serial port data sending, in milliseconds
<b>Open Loop Parameters</b>	
<b>STABILITY_DELAY</b>	Time to stabilize the rotor in a given position during the alignment stage
<b>RAMP_START</b>	Initial period of the electrical cycle at the beginning of open loop ramp (Maximum period)
<b>RAMP_END</b>	Final period of the electrical cycle at the end of open loop ramp (Minimum period)
<b>RAMP_SLOPE</b>	Rate of electrical cycle period decrease - fixed value subtracted to timer 1 period. Used in the first stage of the open loop ramp.
<b>RAMP_SLOPE2</b>	Rate of electrical cycle period decrease, in percentage. Used in the second stage of the open loop ramp.
<b>RAMP_THRESHOLD</b>	Open loop electrical cycle period after which the second stage begins. Divides the open loop ramp in two stages: first with linear period decrease and no BEMF validation; second with percentage period decrease and BEMF validation check
<b>OLoop2Lock_THRESHOLD</b>	Number of Pseudo-Hall successful readings to enable sensorless run/lock mode
<b>Pseudo-Halls Parameters</b>	
<b>PHALLS_ERROR</b>	Maximum variation allowed between two consecutive period measurements, retrieved from input capture readings
<b>PHALLS_THRESHOLD</b>	Minimum calculated period allowed, for validation of input capture readings. Necessary to digitally filter signal jitter, present in Pseudo-Halls signal.
<b>PHALLS_MEASURE_STABILITY</b>	Number of consecutive period calculation below/above the maximum variation allowed for the Pseudo-Hall signal to be considered stable/unstable
<b>Rotor_Lock_TIMEOUT</b>	Time, in milliseconds, between two commutations after which locked rotor is considered
<b>Rotor/Braking Parameters</b>	
<b>BRAKE_MIN_ACCEL</b>	Register/pin associated with the button for minimum duty cycle applied to the rotor
<b>BRAKE_MED_ACCEL</b>	Register/pin associated with the button for medium duty cycle applied to the rotor
<b>BRAKE_MAX_ACCEL</b>	Register/pin associated with the button for maximum duty cycle applied to the rotor
<b>BRAKE_MIN_VAL</b>	Value of the minimum duty cycle applied to the rotor
<b>BRAKE_MED_VAL</b>	Value of the medium duty cycle applied to the rotor
<b>BRAKE_MAX_VAL</b>	Value of the maximum duty cycle applied to the rotor

Table A.2 - Major Parameters listing and respective software Implications

### A.3 FLAGS LISTING

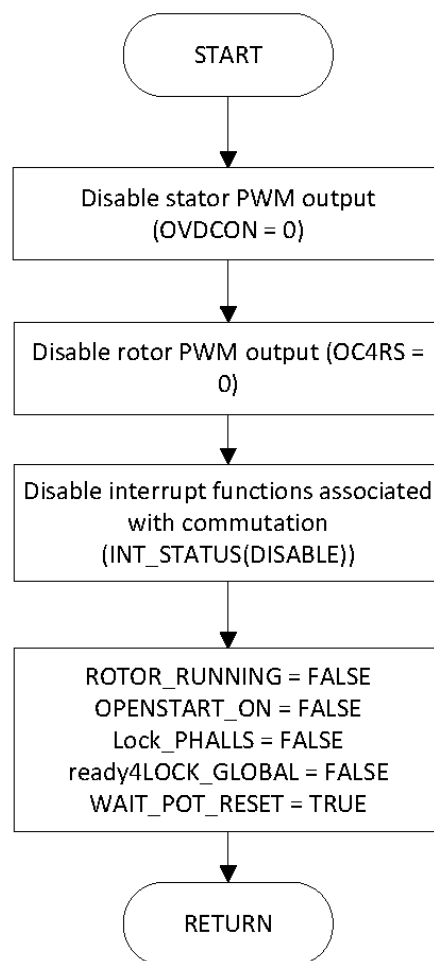
Flags	Purpose	Modified in	Used in
<b>ROTOR_RUNNING</b>	Indicates commutation status	START_Motor and STOP_Motor	main
<b>OPENSTART_ON</b>	Indicates Open Loop ramp status	START_Motor, STOP_Motor and Open2Lock_transition	CNInterrupt and T1Interrupt
<b>Lock_PHALLS</b>	Indicates sensorless run/lock mode status	STOP_Motor and CNInterrupt	T2interrupt and main
<b>ready4LOCK_IC7</b>	Indicates validation status of period calculations based in readings of the Pseudo-Hall associated with IC7.	System_routines	System_routines
<b>ready4LOCK_IC8</b>	Indicates validation status of period calculations based in readings of the Pseudo-Hall associated with IC7.	System_routines	System_routines
<b>ready4LOCK_GLOBAL</b>	Indicates validation status of both IC7 and IC8 period calculations	System_routines and STOP_Motor	CNInterrupt (optional)
<b>WAIT_POT_RESET</b>	Indicates potentiometer need for reset status after commutation stops	main and STOP_Motor	main

Table A.3 - Flags listing and respective software implications

# Appendix B

## FIRMWARE FLOW CHARTS

---



**Figure B.1 - STOP\_Motor function flow chart**

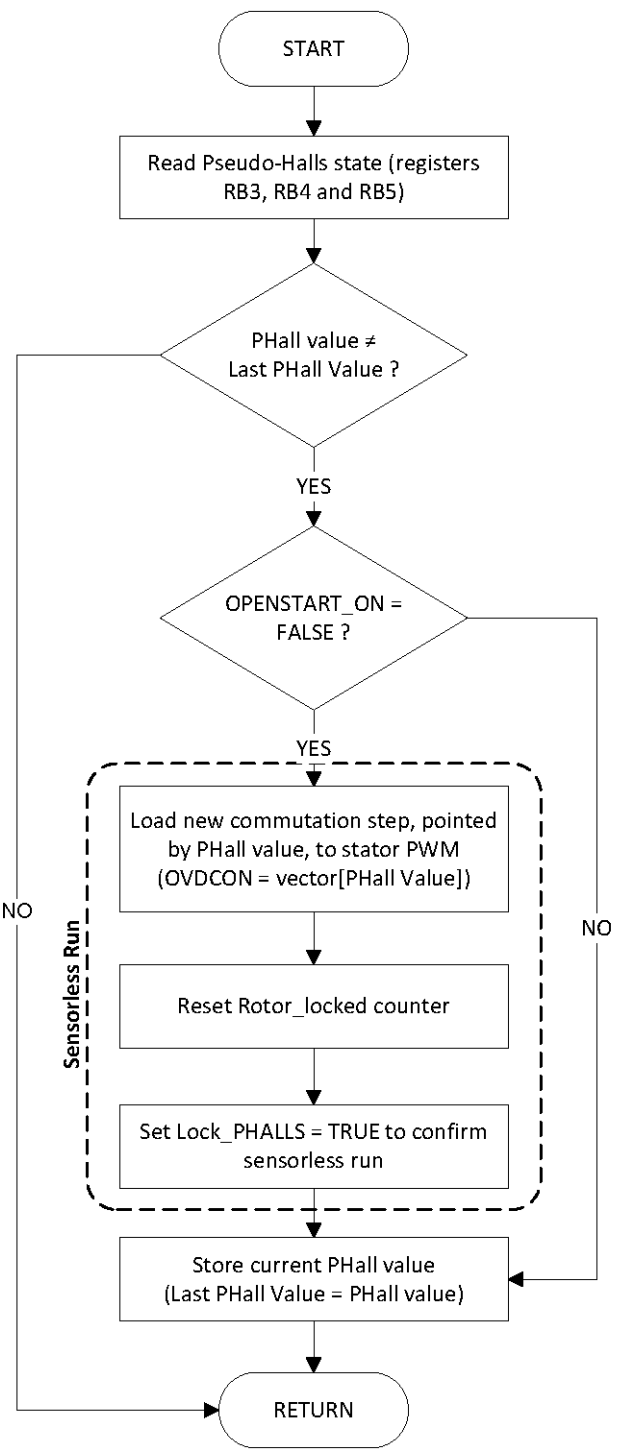
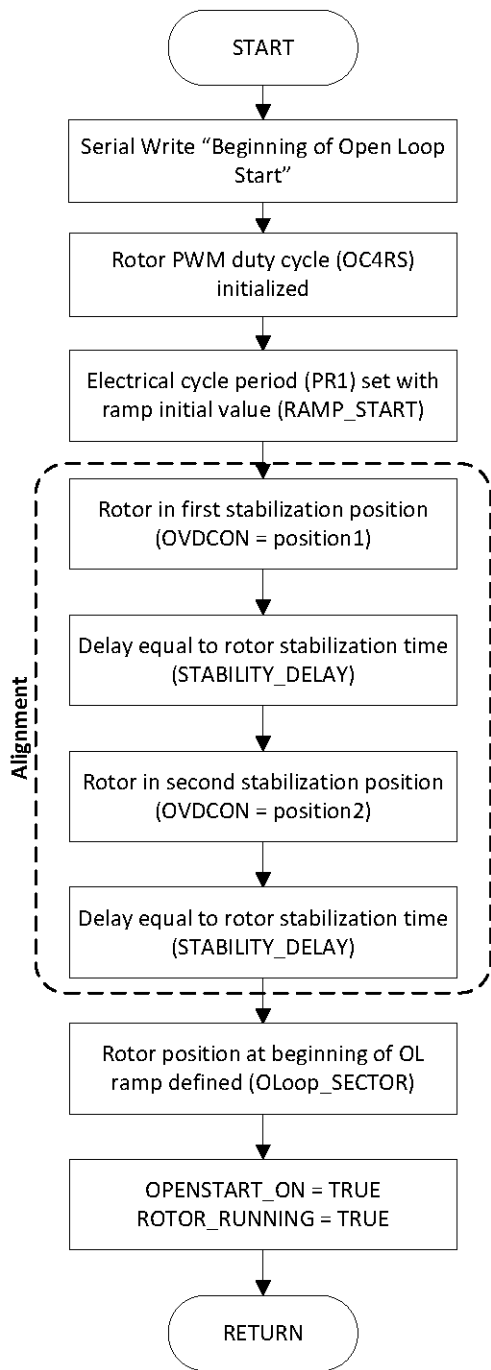


**Figure B.2 - START\_Motor function flow chart**

chart

**Figure B.3 - CNIInterrupt function flow chart**

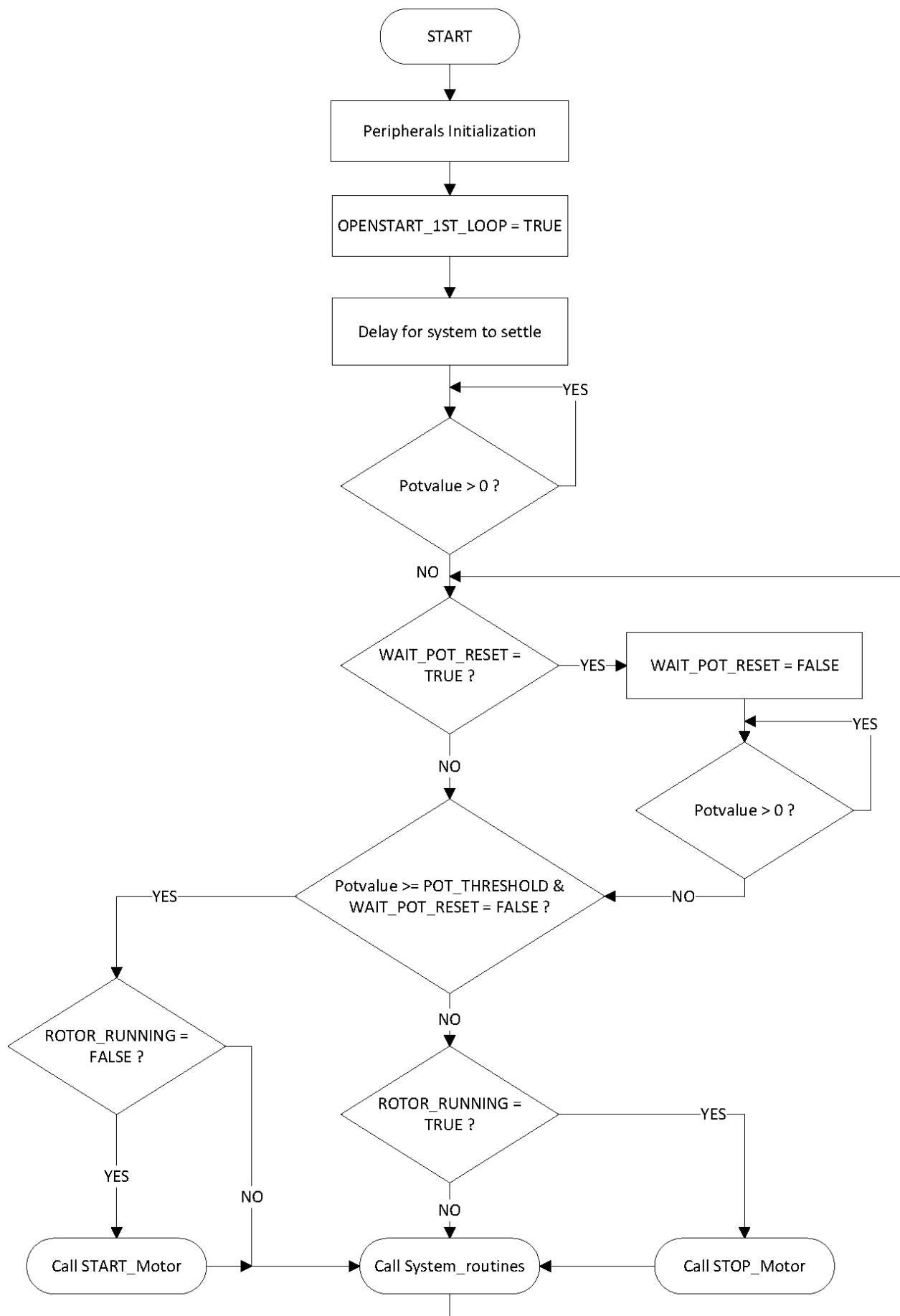


**Figure B.4 - Main function flow chart**

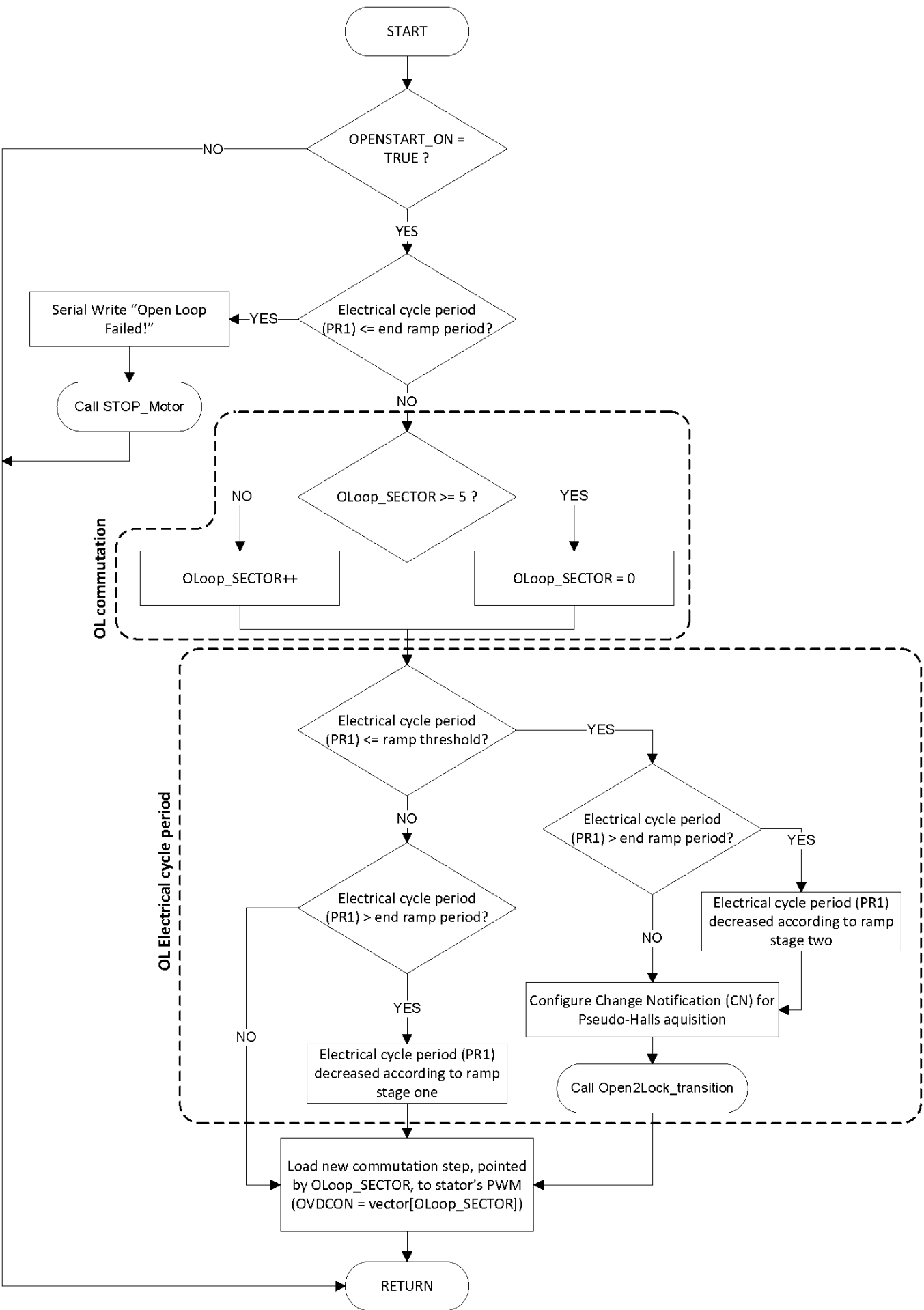


**Figure B.5 - T1Interrupt function flow chart**

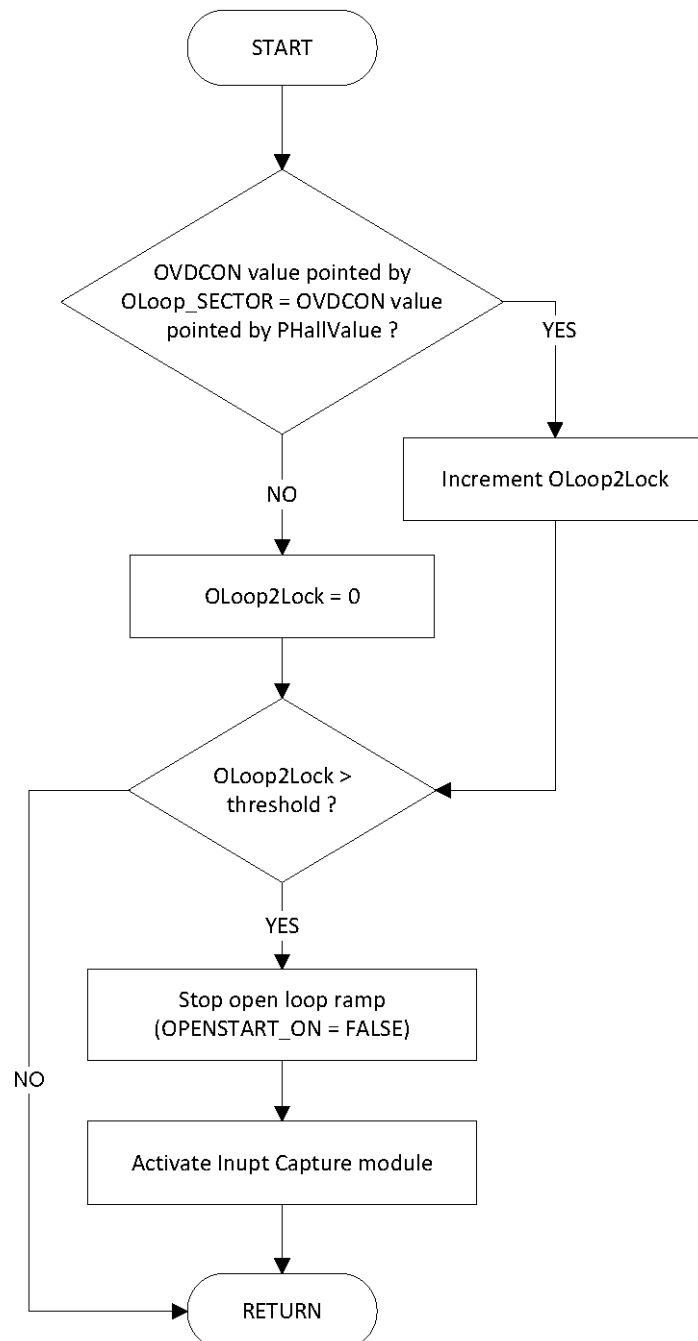


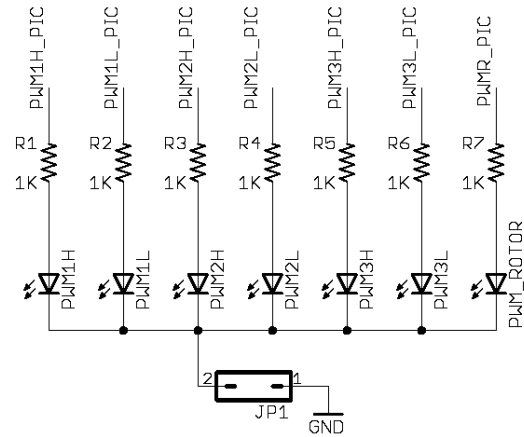
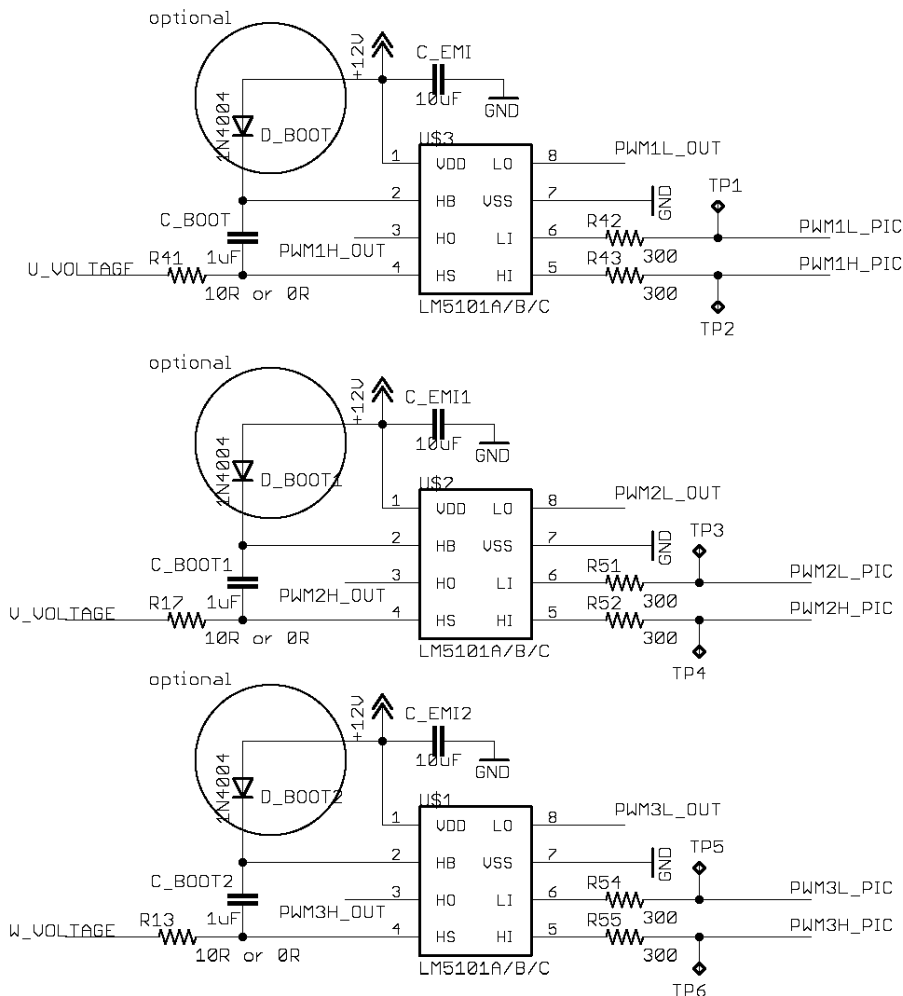
**Figure B.6 - Open2lock\_transition function flow chart**

# Appendix C

## SCHEMATICS

---

**Figure C.1 - MOSFET gate drivers circuitry schematics**



### MOSFET GATE DRIVERS

TITLE: teste\_board1\_181010

Document Number:

REV:

Date: not saved!

Sheet: 1/5

**Figure C.2 - Phase and bus currents feedback circuitry schematics**

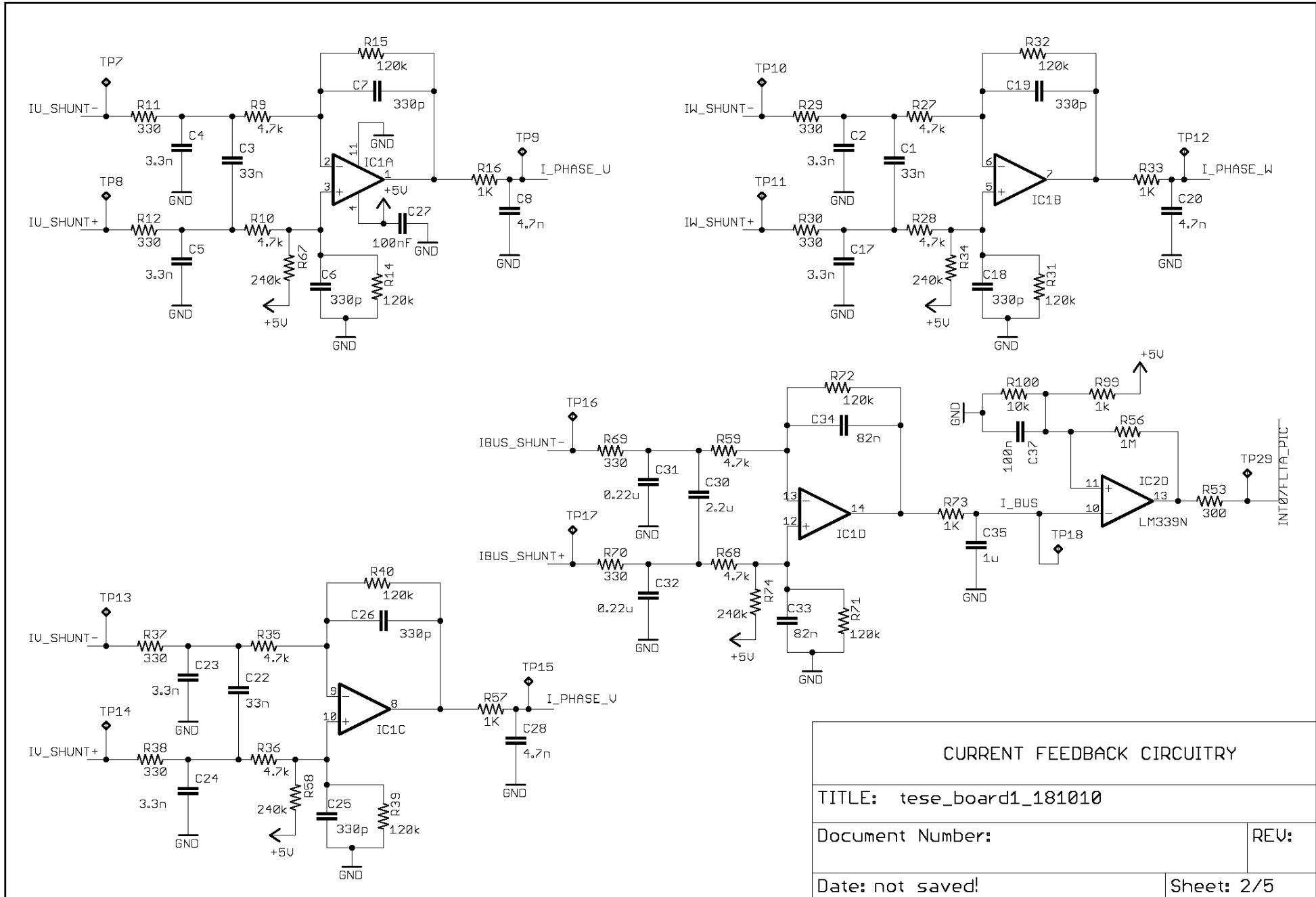


**Figure C.3 -Schematics of DIN 96, DIL 10 and DB 25 connectors, buttons and geartooth**

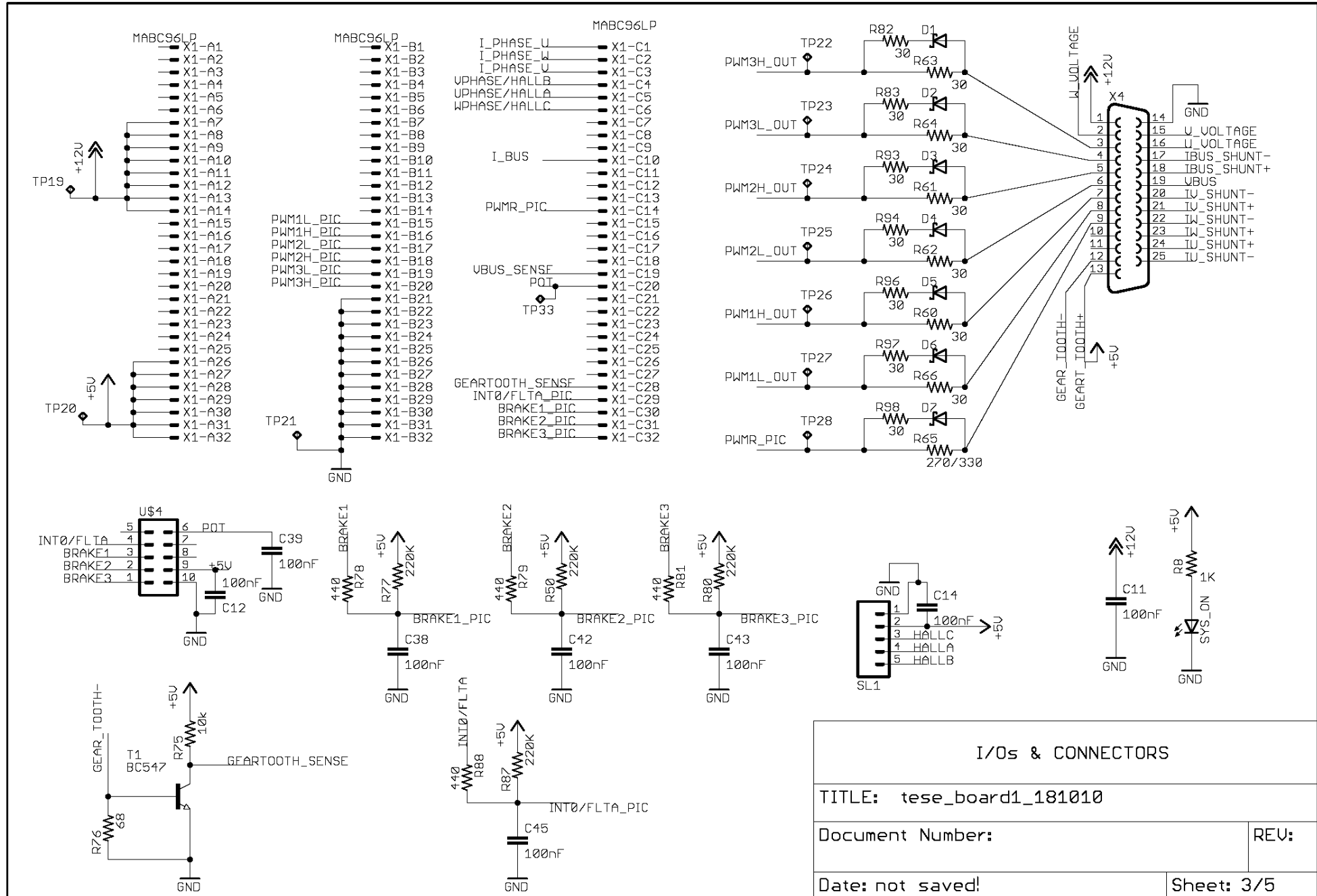
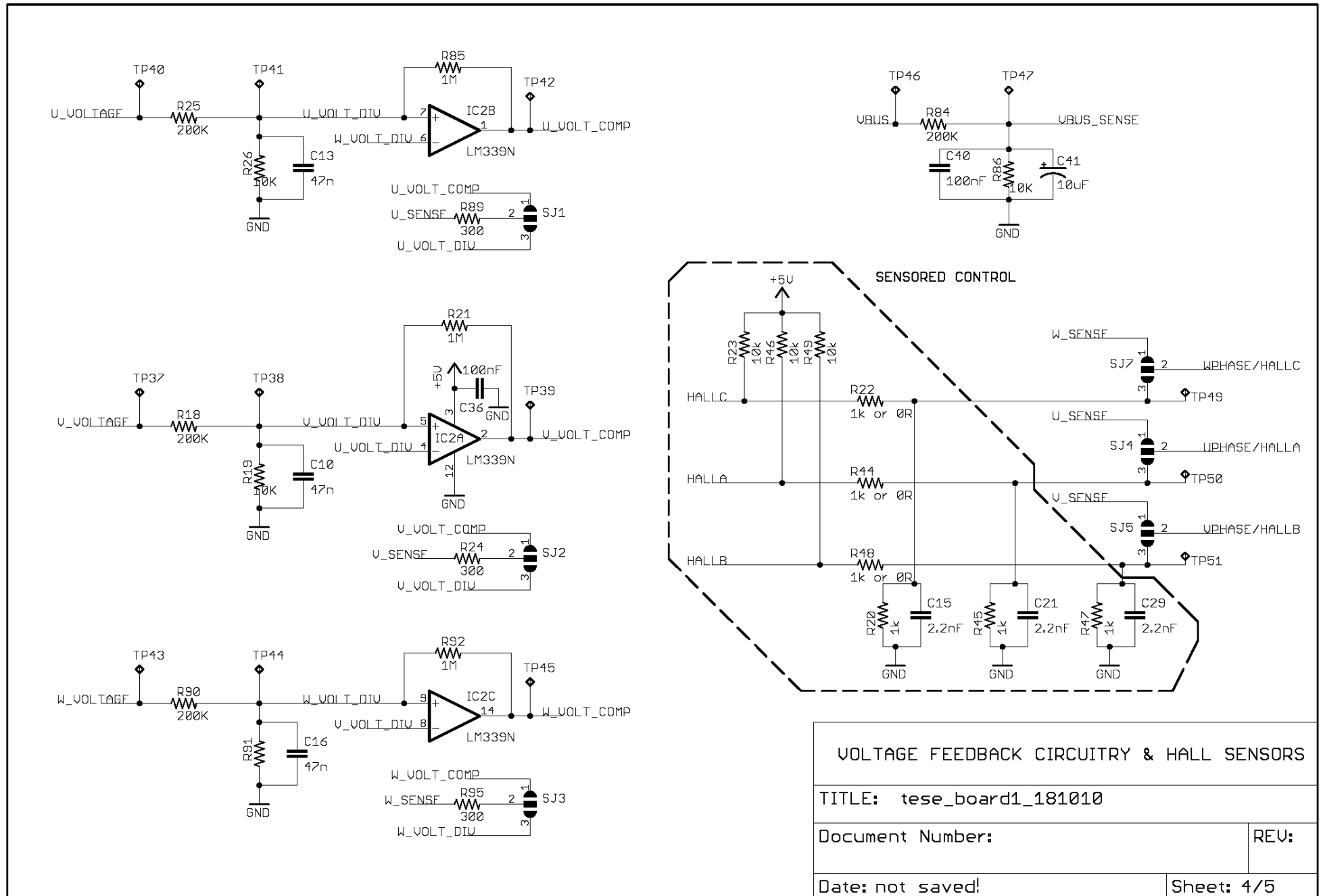
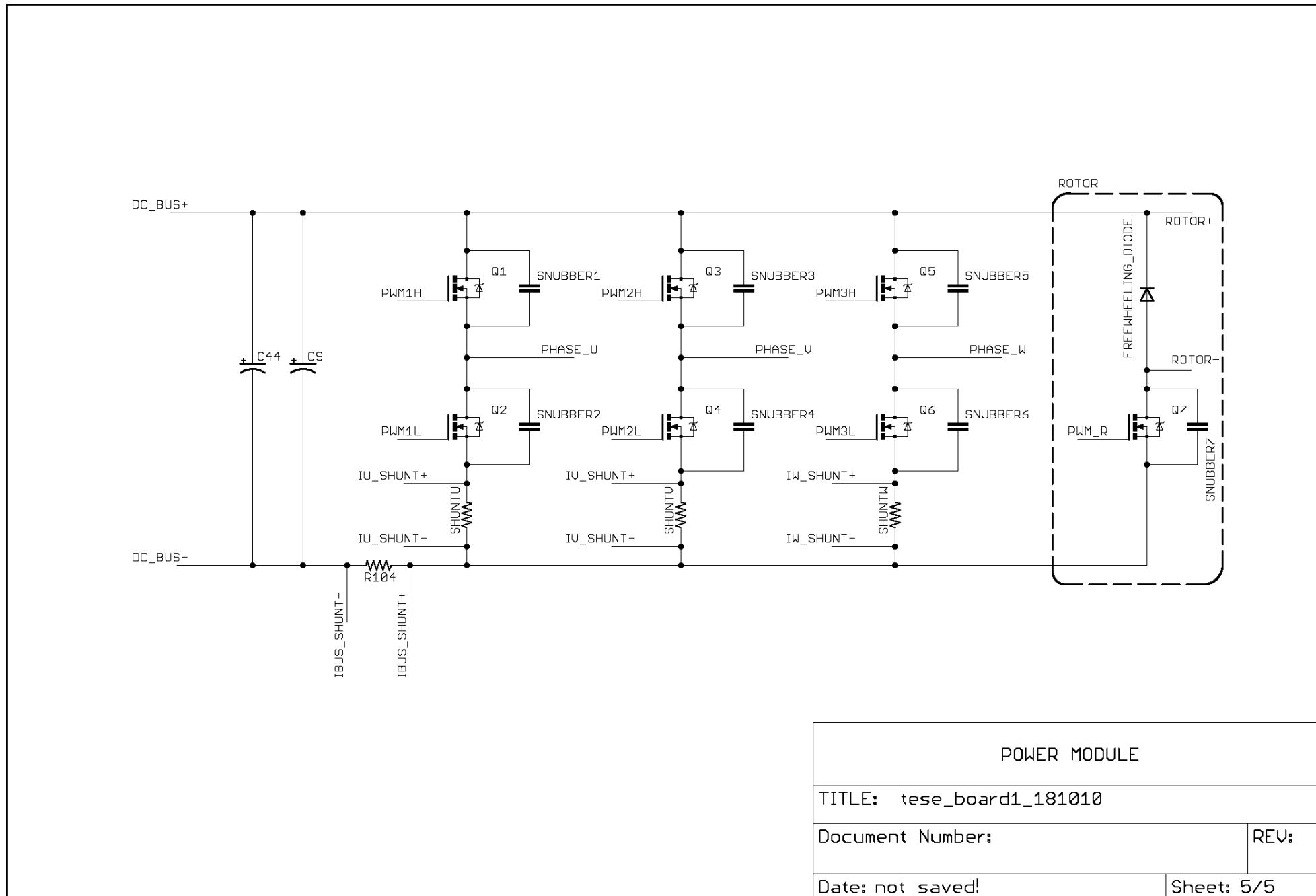


Figure C.4 -Voltage Feedback circuitry and Hall sensors interface schematics



**Figure C.5 - Power module schematics**



# Appendix D

## HARDWARE VALIDATION RESULTS

---

The following graphs were obtained using the laboratory oscilloscope, providing an experimental look over the behavior of the hardware built.

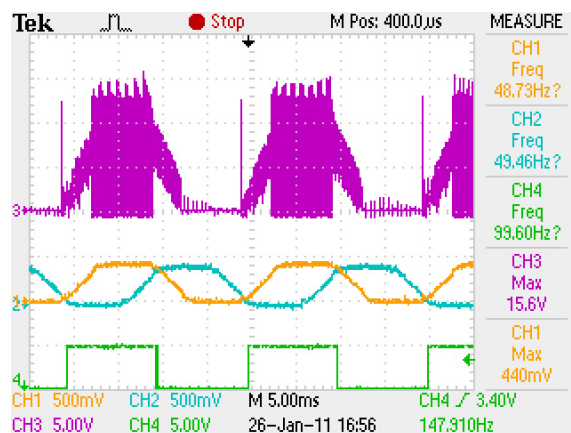


**Figure D.1 - BEMF of phase U (CH3) and BEMF filtering of phases U (Ch1) and W (CH2) during sensorless run mode; correspondent pseudo-Hall signal *U\_VOLT\_COMP* (CH4)**

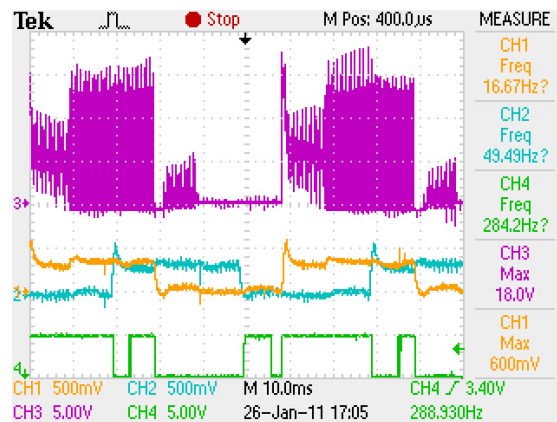
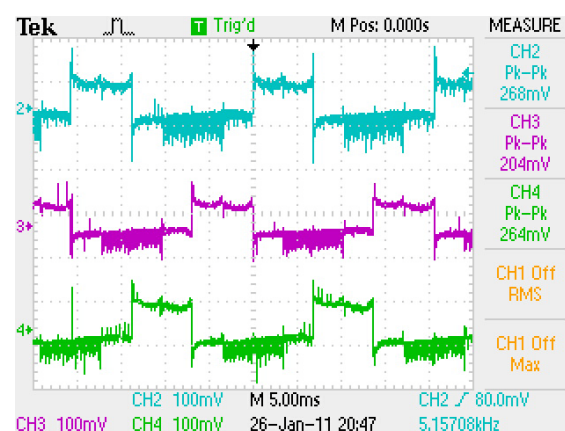
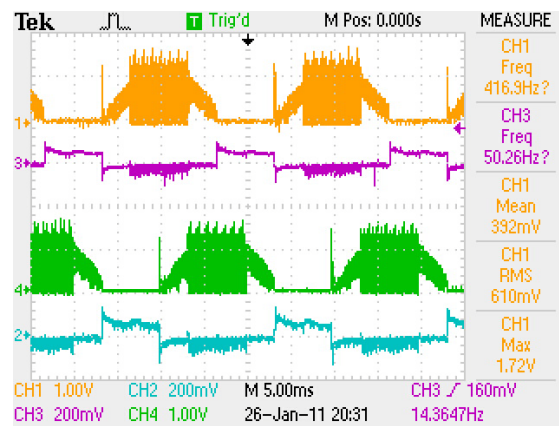


**Figure D.2 - BEMF of phase U (CH3) and BEMF filtering of phases U (Ch1) and W (CH2) during open loop start; correspondent pseudo-Hall signal *U\_VOLT\_COMP* (CH4)**



# BIBLIOGRAPHY

---

- [1]. **Luongo, Cesar A., et al.** *Next Generation More-Electric Aircraft: A Potential Application for HTS Superconductors*. s.l. : IEEE Transactions on Applied Superconductivity, 2009.
- [2]. **Faleiro, Lester.** Beyond the More Electric Aircraft. *AEROSPACE AMERICA*. 2005.
- [3]. **Honeywell.** The More Electric Architecture Revolution. *Honeywell International Inc . [Online]* 2010.  
[http://www.honeywell.com/sites/portal?smap=aero&page=aerotechmagazinearchive3\\_two&theme=T4&catID=CAJGEVG59TXDA5S08CM5CU9WUV3N2ZISW&id=HAQU1907ZGJW9PMPHOYVSCSHM9H4X6KV5&sel=2](http://www.honeywell.com/sites/portal?smap=aero&page=aerotechmagazinearchive3_two&theme=T4&catID=CAJGEVG59TXDA5S08CM5CU9WUV3N2ZISW&id=HAQU1907ZGJW9PMPHOYVSCSHM9H4X6KV5&sel=2).
- [4]. **Clean Sky.** [Online] <http://www.cleansky.eu/>.
- [5]. **Devatine-Lacaze, Isabelle.** Dispatch Towing - The Green Revolution from Airbus. s.l. : © Airbus France S.A.S., 2010.
- [6]. **IAI.** TAXIBOT SYSTEM. *Israel Aerospace Industries*. [Online] [http://www.iai.co.il/35095-39730-en/Groups\\_Military\\_Aircraft\\_Lahav\\_Products\\_TaxiBot.aspx](http://www.iai.co.il/35095-39730-en/Groups_Military_Aircraft_Lahav_Products_TaxiBot.aspx).
- [7]. Honeywell And Safran To Create Joint Venture To Launch New Green Aircraft Taxiing System . *Honeywell*. [Online] 2011. <http://honeywell.com/News/Pages/Honeywell-And-Safran-To-Create-Joint-Venture-To-Launch-New-Green-Aircraft-Taxiing-System.aspx>.
- [8]. Messier-Bugatti's "Green Taxiing" solutions for Smarter Ground Operations. *Safran group*. [Online] 2010. <http://www.safran-group.com/site-safran-en/press-media/press-releases/2010-698/article/messier-bugatti-s-green-taxiing?10498>.
- [9]. **WheelTug.** [Online] <http://www.wheeltug.gi/>.
- [10]. Aerospace manufacturers look to electricity for developing aircraft ground taxiing green technology. *Green Air Online*. [Online] 2011.  
<http://www.greenaironline.com/news.php?viewStory=1293>.
- [11]. **Raes, Dwayne.** *Efficient autonomous pushback and taxiing - a step forward to reducing costs and pollution*. s.l. : Hamburg University of Applied Sciences , 2008.
- [12]. **Motors, Chorus.** *WheelTug*. [Online]  
<http://www.chorusmotors.com/wheeltug/index.shtml>.

- [13]. **Cheng, Victor H. L., Sharma, Vivek and Foley, David C.** A Study of Aircraft Taxi Performance for Enhancing Airport Surface Traffic Control. *IEEE TRANSACTIONS ON INTELLIGENT TRANSPORTATION SYSTEMS*. 2001, Vol. 2.
- [14]. Taxi Procedures. *Operational Liaison Meeting FBW aircraft*.
- [15]. **Rypdal, Kristin.** Aircraft Emissions. *Good Practice Guidance and Uncertainty Management in National Greenhouse Gas Inventories*.
- [16]. Jet Fuel Price Monitor . IATA. [Online] 2011. [http://www.iata.org/whatwedo/economics/fuel\\_monitor/Pages/index.aspx](http://www.iata.org/whatwedo/economics/fuel_monitor/Pages/index.aspx).
- [17]. **CleanSky.** *Call for Proposals: CLEAN SKY RESEARCH and TECHNOLOGY DEVELOPMENT PROJECTS*. s.l. : Clean Sky Joint Undertaking , Call SP1-JTI-CS-2010-05.
- [18]. —. *Call for Proposals: CLEAN SKY RESEARCH and TECHNOLOGY DEVELOPMENT PROJECTS*. s.l. : Clean Sky Joint Undertaking , Call SP1-JTI-CS-2011-01.
- [19]. **Silva, Dário G. R.** *ELECTROMAGNETIC BRAKING SYSTEM FOR AIRCRAFT APPLICATION - PROTOTYPE DESIGN*. s.l. : Instituto Superior Técnico, 2010.
- [20]. **Henneberger, Gerhard.** *Electrical Machines I*. s.l. : Aachen University , 2002.
- [21]. **Hughes, Austin.** *Electric motors and drives: fundamentals, types and applications*. Third Edition. s.l. : Newnes, 2006.
- [22]. **Münch, Vera.** Electric Drive Unit 1eDT330. s.l. : Getrag, 2010.
- [23]. **Martin, Andrew.** *More Electric Aircraft Forum - A Review of Active Rectification in aircraft AC systems*. s.l. : MOET Project Consortium, 2009.
- [24]. **Jomier, T.** *MOET Technical Report (deliverable D0.02.3)*. s.l. : MOET Consortium, 2009.
- [25]. **FOURIE, Frédéric and ANDRIAMISAINA, Mathias.** *More Electric Aircraft Forum - Large aircraft integration rig and tests results* . s.l. : MOET Project Consortium, 2009.
- [26]. **Wheeler, Pat.** The More Electric Aircraft - Why Aerospace needs Power Electronics . s.l. : University of Nottingham.
- [27]. **Brown, Ward.** *AN857 - Brushless DC Motor Control Made Easy*. s.l. : Microchip Technology Inc., 2002.
- [28]. **Tawadros, Markos, Rizk, Jamal and Nagrial, Mahmood.** *Sensorless Control of Brushless Drives Using Back emf Mapping*. School of Engineering - University of Western Sydney . s.l. : Second International Conference on Computer and Electrical Engineering, 2009.

[29]. **Stopa, Pawet.** *High Speed Field Oriented Control*. Institut e of Energy Technology - Aalborg University. June 2009.

[30]. *A Study of New Techniques of Controlled PWM Inverters*. **Farid, Berrezzek and Amar, Omeiri**. s.l. : ISSN - European Journal of Scientific Research, 2009, Vol. 32.

[31]. **Johnson, James P., Ehsani, M. and Guzelgiinler, Yilcan.** *Review of Sensorless Methods for Brushless DC*. Power Electronics Laboratory, Texas A&M University.

[32]. **Grasblum, Pavel.** *DRM086 - Sensorless BLDC Motor Control Using MC9S08AW60*. s.l. : Freescale Semiconductor, Inc., 2007.

[33]. **Akin, Bilal.** *State estimation techniques for speed sensorless Field Oriented Control of induction motors*. The Graduate School of Natural and Applied sciences of The Middle East Technical University. August 2003.

[34]. **Prasad, V Himamshu.** *Analysis and comparison of Space Vector Modulation Schemes for three-leg and four-leg voltage source*. Virginia Polytechnic Institute and State University. 1997.

[35]. **D'Souza, Stan.** *AN992 - Sensorless BLDC Motor Control Using dsPIC30F2010*. s.l. : Microchip Technology Inc., 2005.

[36]. **Elliott, Charlie and Bowling, Steve.** *AN901 - Using the dsPIC30f for Sensorless BLDC Control*. s.l. : Microchip Technology Inc., 2004.

[37]. *A New Cost Effective Sensorless Commutation Method for Brushless DC Motors Without Phase Shift Circuit and Neutral Voltage*. **Chen, Cheng-Hu and Cheng, Ming-Yang.** s.l. : IEEE Transactions on Power Electronics, March 2007, Vol. 22.

[38]. **Yedamale, Padmaraja.** *AN970 - Using the PIC18F2431 for Sensorless BLDC Motor Control*. s.l. : Microchip Technology Inc., 2005.

[39]. *Sensorless Control of the BLDC Motors From Near-Zero to High Speeds*. **Kim, Tae-Hyung and Ehsani, Mehrdad.** s.l. : IEEE Transactions on Power Electronics, November 2004, Vol. 19.

[40]. **Yedamale, Padmaraja.** *AN885 - Brushless DC (BLDC) Motor Fundamentals*. s.l. : Microchip Technology Inc., 2003.

[41]. **Cheles, Mihai and Sammoud, Hafedh.** *AN1206 - Sensorless Field Oriented Control (FOC) of an AC Induction Motor (ACIM) Using Field Weakening*. s.l. : Microchip Technology Inc., 2008.

[42]. **D'Souza, Stan.** *AN957 - Sensored BLDC Motor Control Using dsPIC30f2010*. s.l. : Microchip Technology Inc., 2004.

[43]. **Microchip.** *dsPIC30F Family Reference Manual - High-Performance Digital Signal Controllers*. s.l. : Microchip Technology Inc., 2006.

- [44]. —. dsPIC30F4011/4012 Data Sheet. s.l. : Microchip Technology Inc., 2010.
- [45]. **Yedamalem, Padmaraja.** *AN889 - Brushless DC Motor Control Using PIC18FXX31 MCUs*. s.l. : Microchip Technology Inc., 2004.
- [46]. **Microchip.** dsPICDEM™ MCLV DEVELOPMENT BOARD USER'S GUIDE. s.l. : Microchip Technology Inc., 2008.
- [47]. —. dsPICDEM™ MC1L 3-Phase Low Voltage Power Module User's Guide. s.l. : Microchip Technology Inc., 2003.
- [48]. —. dsPICDEM™ MCHV Development System User's Guide. s.l. : Microchip Technology Inc., 2009.
- [49]. **freescale.** 3-Phase BLDC/PMSM Low-Voltage Motor Control Drive User Manual. s.l. : freescale™ semiconductor, 2009.
- [50]. **IR.** IRMD2336DJ - 3 PHASE GATE DRIVER IC REFERENCE DESIGN KIT. s.l. : International Rectifier, 2008.
- [51]. **Balogh, Laszlo.** *Design And Application Guide For High Speed MOSFET Gate Drive Circuits*.
- [52]. **D. Pathak, Abhijit.** *AN0002 - MOSFET/IGBT DRIVERS THEORY AND APPLICATIONS*. s.l. : IXYS, 2011.
- [53]. **IR.** *AN978 - HV Floating MOS-Gate Driver ICs*. s.l. : International Rectifier.
- [54]. **National.** LM5101B - 2A High Voltage High-Side and Low-Side Gate Driver. s.l. : National Semiconductor Corporation, 2010.
- [55]. **Merello, Andrea.** *AN1123 - Bootstrap Network Analysis: Focusing on the Integrated Bootstrap Functionality*. s.l. : International Rectifier.
- [56]. **Merello, A., Rugginenti, A. and Grasso, M.** *DT04-4 - Using monolithic high voltage gate drivers*. s.l. : International Rectifier.
- [57]. **Chey, Chris and Parry, John.** *DT97-3 - Managing Transients in Control IC Driven Power Stages*. s.l. : International Rectifier.
- [58]. **Lepkowski, Jim.** *AN894 - Motor Control Sensor Feedback Circuits*. s.l. : Microchip Technology Inc., 2003.
- [59]. **Microchip.** MCP6024 - Rail-to-Rail Input/Output, 10 MHz Op Amp. s.l. : Microchip Technology Inc., 2006.
- [60]. **Allegro.** ATS642LSH - Two-Wire True Zero Speed Miniature Differential Peak-Detecting Gear Tooth Sensor with Continuous Calibration. s.l. : Allegro MicroSystems, Inc., 2009.

- [61]. **Blake, Carl and Bull, Chris.** IGBT or MOSFET: Choose Wisely. s.l. : International Rectifier.
- [62]. **IR.** IRFP4310ZPbF HEXFET® Power MOSFET. s.l. : International Rectifier.
- [63]. **Shao, Jianwen.** *Direct Back EMF Detection Method for Sensorless Brushless DC (BLDC) Motor Drives*. Virginia Polytechnic Institute and the State University . September 2003.
- [64]. **IR.** AN936 - *The Do's and Don'ts of Using MOS-Gated Transistors*. s.l. : International Rectifier.
- [65]. **Gomez, F. and Scholz, D.** *IMPROVEMENTS TO GROUND HANDLING OPERATIONS AND THEIR BENEFITS TO DIRECT OPERATING COSTS*. s.l. : Hamburg University of Applied Sciences , 2009.